Atmospheric Artifacts Correction for InSAR Using Empirical Model and Numerical Weather Prediction Models

Author

Zhongbo Hu

Thesis Supervisor

Jordi J. Mallorquí

A thesis submitted to the Universitat Politècnica de Catalunya (UPC)
in partial fulfillment of the requirements for the degree of
DOCTOR OF PHILOSOPHY

Ph.D program on Signal Theory and Communications
CommSensLab - Unidad de Excelencia María de Maeztu
Universitat Politècnica de Catalunya (UPC)
Barcelona, November 2019

Atmospheric Artifacts Correction for InSAR Using Empirical Model and Numerical Weather Prediction Models
Thesis written by Zhongbo Hu

Ph.D. program on Signal Theory and Communications
This work has been supported by CSC-UPC Fellowship Program, the Spanish Ministry of Economy, Industry and Competitiveness (MINECO), the Agencia Estatal de Investigación (AEI), the European Funds for Regional Development (EFRD) under project TEC2017-85244-C2-2-P and the National Natural Science Foundation of China (Grant 51574221, 41874044). CommSensLab is Unidad de Excelencia María de Maeztu MDM-2016-0600 financed by the AEI, Spain.

Preface

I would like to dedicate this PhD thesis to the people who made this research possible.

First and foremost, I would like to express my sincere gratitude to my supervisor, Prof. Jordi J. Mallorquí, not only for his constructive and patient guidance in academic matters, but also for his influence in my life. Prof. Jordi J. Mallorquí is deeply knowledgeable about InSAR. I still cannot fathom how he mastered both theoretical InSAR and practical data processing. He is uniquely keen on and good at programming. I will never forget what he always said to me: "Pass me your code. I prefer to read some codes after lunch". The SUBSIDENCE software his group developed is a treasure; it helped me to learn technical InSAR. His attitude towards life outside of academics also deeply impressed me. His sense of humor makes his students feel welcome and at home. In my heart, he is my friend more than a professor. I will never forget the BBQs he hosted with his family. Their hospitality helped me fall in love with the fantastic city of Barcelona.

I would also like to thank my former supervisor, Prof. Yunjia Wang from China University of Mining and Technology, for his endless and selfless support, which allowed me to study abroad. I never thought that I would have the opportunity to pursue my PhD in a foreign country. He helped my dream come true.

I would like to thank my colleagues in the remote sensing research group for their support and for the many enjoyable hours we spent together. I am very grateful to Giuseppe Centolanza for our valuable discussions during my first year. I am also grateful to Joaquín Escayo Menéndez from Instituto de Geociencias CSIC-UCM, who is an expert in Linux, for helping me solve many Linux problems and for our lengthy and inspiring email discussions. Paolo Testolina from Università deli Studi di Padova only stayed with our group for several months, but gave me a very good impression of Italy. I am grateful to Aynie Khoe and Beni Vazquez for helping me with bureaucratic matters. My thanks also go to Hongdong Fan, Feng Zhao and Sen Du for the delightful experience we had together in Barcelona. We are from the same university in China and had the same supervisor in Spain. It is the fate that brought us together.

Furthermore, I would like to express my special gratitude to my family. It is not common for parents to support their children's education endlessly in my hometown. My parents are an exception. They supported my study unconditionally even when the future was uncertain. I am also greatly indebted to my beloved wife Yanping Tan, who left her family and has been with me in Barcelona since 2016. She is such a model wife that words cannot express my gratitude for everything that she does, but I must say that I am a most fortunate man because of her. I am also deeply grateful to my parents-in-law

for their selfless love. We are the only children in our two families. They chose to let us go and to endure loneliness because they know what is best for their children.

Zhongbo Hu
Barcelona, November 13, 2019

Acknowledgments

The author would like to acknowledge the following institutions:

- **CSC** (China Scholarship Council) for providing three years doctoral fellowship (Grant 201506420043).
- **MINECO** (Spanish Ministry of Economy, Industry and Competitiveness) and **EFRD** (European Funds for Regional Development) for providing financial support under project TEC2017-85244-C2-2-P.
- **AEI** (Agencia Estatal de Investigación) for its financial support to the "María de Maeztu" Unit of Excellence, MDM-2016-0600.
- **NSFC** (National Natural Science Foundation of China) for providing financial support, under Grant 51574221 and Grant 41874044.
- **ESA** (European Space Agency) for providing Sentinel-1 Synthetic Aperture Radar (SAR) data.
- **ECMWF** (European Centre for Medium-Range Weather Forecasts) for providing ERA-Interim and ERA5 datasets.
- **NASA** (National Aeronautics and Space Administration) for providing MERRA2 weather forecast data.
- **NCAR** (National Center for Atmospheric Research) for providing the WRF model.

Contents

Abstract xi

Acronyms xiii

1 Introduction 1

1.1 Atmospheric artifacts . . . 1
1.2 Compensation based on temporal-spatial filters . . . 2
1.3 Compensation based on empirical models . . . 3
1.4 Compensation based on ancillary observation data . . . 3
1.5 Motivation . . . 4
1.6 Objectives of the thesis . . . 5
1.7 Structure of the thesis . . . 5

2 InSAR and tropospheric delay on InSAR 7

2.1 SAR . . . 7
2.2 InSAR and DInSAR . . . 11
2.3 InSAR derived techniques and their applications . . . 12
2.4 Coherence and error sources . . . 14
2.4.1 Coherence . . . 14
2.4.2 Decorrelation factors . . . 15
2.4.3 Other sources of error . . . 16
2.5 PSI techniques and the Coherent Pixels Technique . . . 18
2.5.1 Interferograms preparation and pixels selection . . . 22
2.5.2 CPT linear module . . . 23
2.5.3 CPT non-linear module . . . 24
2.5.4 CPT products module . . . 24

3 Empirical model for tropospheric delay compensation **27**
3.1 Covariance weighted linear model . . . 28
3.1.1 Weighted linear model to estimate stratified APS . . . 28
3.1.2 Spatial covariance matrix . . . 29
3.2 Simulated study . . . 30
3.2.1 Simulation of the different phase components . . . 30
3.2.2 Stratified atmospheric artifacts estimation . . . 33
3.2.3 Evaluation of results and sensitivity analysis . . . 34
3.3 Validation with real SAR data . . . 38
3.3.1 Test site and data set . . . 38
3.3.2 Processing chain . . . 39
3.3.3 Stratified atmospheric artifacts compensation . . . 41
3.3.4 Validation with global meteorological reanalysis data . . . 43
3.3.5 Statistical analyses on all interferograms . . . 44
3.4 Summary . . . 47

4 Tropospheric delay mitigation using global weather forecast models **49**
4.1 Methodology . . . 50
4.1.1 Traditional methods based on global atmospheric models . . . 50
4.1.2 Drawbacks of the zenith total delay approach . . . 51
4.1.3 Precise LOS phase delay calculation . . . 52
4.2 Test sites, ERA5 dataset and SAR data processing . . . 54
4.2.1 Tenerife island, Spain . . . 54
4.2.2 Crete, Greece . . . 56
4.2.3 Almería, Spain . . . 56
4.2.4 ERA5 . . . 56
4.2.5 SAR datasets and data processing . . . 56
4.3 Algorithm validation in Tenerife island . . . 57
4.3.1 Implementation of the improved method . . . 57
4.3.2 Tenerife island case study analysis . . . 59
4.3.3 Statistics analyses . . . 62
4.4 Application for Crete, Greece . . . 63
4.5 Application for Almería, Spain . . . 66
4.6 Comparison of different global atmospheric models . . . 69
4.6.1 ERA-Interim . . . 69

4.6.2 MERRA . . . 69
4.6.3 Tenerife, Spain . . . 70
4.6.4 Almería, Spain . . . 75
4.6.5 Crete, Greece . . . 78
4.7 Summary . . . 81

5 Tropospheric delay mitigation using local numerical weather prediction models 83
5.1 Introduction . . . 84
5.2 Local numerical weather prediction models . . . 85
5.2.1 WRF . . . 86
5.2.1.1 WRF model scheme . . . 88
5.2.1.2 WRF model setup . . . 90
5.3 APS correction based on the WRF model . . . 93
5.3.1 Evaluation in Tenerife, Spain . . . 93
5.3.2 Evaluation in Almería, Spain . . . 96
5.4 Summary . . . 99

6 Application for Gansu of APS correction methods 101
6.1 Introduction . . . 102
6.2 Implementation and results discussion . . . 104
6.2.1 Simulated atmospheric artifacts . . . 104
6.2.2 V-LMRTA residual . . . 104
6.2.3 D-LOS MERRA2 residual . . . 107
6.2.4 D-LOS ERA5 residual . . . 108
6.2.5 D-LOS WRF residual . . . 109
6.3 Summary . . . 110

7 Conclusions and future lines 111
7.1 Conclusions . . . 111
7.1.1 Correcting APS using a covariance-weighted linear model . . . 111
7.1.2 Comparison between Z-LOS and D-LOS correction methods . . . 112
7.1.3 APS mitigation using global numerical weather models . . . 113
7.1.4 APS mitigation based on the local WRF model . . . 114
7.2 Future research lines . . . 115

List of Figures 117

List of Tables **121**

Bibliography **123**

List of Publications **133**

Abstract

Geological hazards, such as earthquakes, volcanoes, landslides, cause significant threats to human life and property all over the world. In general, most of the geological hazards are associated with ground movement. Synthetic Aperture Radar Interferometry (InSAR) has been proved its unprecedented ability and merits of monitoring ground deformation on large scale with centimeter to millimeter scale accuracy. However, several factors affect the reliability and accuracy of its applications. Among them, atmospheric artifacts due to spatial and temporal variations of atmosphere state often pose noise to interferograms. Therefore, atmospheric artifacts mitigation remains one of the biggest challenges to be addressed in the InSAR community.

State-of-the-art research works have revealed atmospheric artifacts can be partially compensated with empirical models, temporal-spatial filtering approach in InSAR time series, pointwise GPS zenith path delay and numerical weather prediction models. In this thesis, firstly, we further develop a covariance weighted linear empirical model correction method. Secondly, a realistic Line of Sight (LOS) direction integration approach based on global reanalysis data is employed and comprehensively compared with the conventional method that integrates along zenith direction. Finally, the realistic integration method is applied to local Weather Research and Forecasting Model (WRF) numerical forecast model data. Moreover, detailed comparisons between different global reanalysis data and local WRF model are assessed.

In terms of empirical models correcting methods, many publications have studied correcting stratified tropospheric phase delay by assuming a linear model between them and topography. However, most of these studies have not considered the effect of turbulent atmospheric artefacts when adjusting the linear model to data. In this thesis, an improved technique that minimizes the influence of turbulent atmosphere in the model adjustment has been presented. In the proposed algorithm, the model is adjusted to the phase differences of pixels instead of using the unwrapped phase of each pixel. In addition, the different phase differences are weighted as a function of its Atmospheric Phase Screen (APS) covariance estimated from an empirical variogram to reduce in the model adjustment the impact of pixel pairs with significant turbulent atmosphere. The good performance of the proposed method has been validated with both simulated and real Sentinel-1 SAR data in the mountainous area of Tenerife island, Spain.

Considering methods using meteorological observations to mitigate APS, an accurate realistic computing strategy utilizing global atmospheric reanalysis data to estimate atmospheric artifacts has been implemented. With the approach, the realistic LOS path

along satellite and the monitored points is considered, rather than converting from zenith path delay. Compared with zenith delay based method, the biggest advantage is that it can avoid errors caused by anisotropic atmospheric behaviour. The accurate integration method is validated with Sentinel-1 data in three test sites: Tenerife island, Spain, Almería, Spain and Crete island, Greece. Compared to conventional zenith method, the realistic integration method shows great improvement in our cases.

A variety of global reanalysis data are available from different weather forecasting organizations, such as ERA-Interim, ERA5, MERRA2. In this study, the realistic integration mitigation method is assessed on these different reanalysis data. The results show that these data are feasible to mitigate APS to some extent in most cases. The assessment also demonstrates that the ERA5 performs the best statistically, compared to other global reanalysis data. Moreover, as local numerical weather forecast models have the ability to predict high spatial resolution atmospheric parameters, by using which, it has the potential to achieve APS mitigation. In this thesis, the realistic integration method is also employed on the local WRF model data in Tenerife and Almería test sites. It is known that the local WRF model depends on the initial atmospheric conditions as well as the parameters setup. In our cases, the latest global meteorological ERA5 data as initial and different setups are used to evaluate the performance of the WRF model. However, it turns out that the WRF model performs worse than the original global reanalysis data.

Acronyms

ALOS Advanced Land Observation Satellite

APS Atmospheric Phase Screen

ARW Advanced Research WRF

CGM Conjugate Gradient Method

CPT Coherent Pixels Technique

CSA Canadian Space Agency

DEM Digital Elevation Model

DInSAR Differential SAR Interferometry

D-LMRTA Distance Weighted LMRTA

DSs Distributed Scatterers

ECMWF European Center for Medium-Range Weather Forecasts

EGM96 Earth Gravitational Model 1996

ERS-1 European Remote Sensing Satellite

ESA European Space Agency

ESD Enhanced spectral diversity

EW Extra Wide Swath

GAM Global Atmospheric Models

GEM Global Environmental Multiscale Model

GEOS-5 Goddard Earth Observing System Data Assimilation System Version 5

GeoSAR Geostationary Synthetic Aperture Radar

GFS Global Forecast System

IFS Integrated Forecast System

InSAR Synthetic Aperture Radar Interferometry

IRF Impulse Response Function

IW Interferometric Wide Swath

JERS Japanese Earth-Resources satellite

KML Keyhole Markup Language

LMRTA Linear Model Resisting Turbulent Atmosphere Delay

LOS Line of Sight

MAF Model Adjustement Function

MERIS Medium Resolution Imaging Spectrometer

MERRA Modern Era-Retrospective Analysis for Research and Applications

MM5 NCAR-Penn State Mesoscale Model Version 5

MODIS Moderate Resolution Imaging Spectroradiometer

MSC Meteorological Service of Canada

MTI Multi-Temporal InSAR

NASA National Aeronautics and Space Administration

NCAR National Center for Atmospheric Research

NCEP National Centers for Environmental Prediction

NMM Nonhydrostatic Mesoscale Model

NOAA National Oceanic and Atmospheric Administration

NWP Numerical Weather Prediction Models

Pol-InSAR Polarimetric SAR Interferometry

PRF Pulse Repetition Frequence

PSI Persistent Scatters Interferometry

PSs Persistent Scatters

PyAPS Python-based Atmospheric Phase Screen

ROI Region of Interest

SAR Synthetic Aperture Radar

SBAS Small Baseline Subsets

SD Standard Deviation

SLC Single Look Complex

SNR Signal-to-Noise Ratio

SRTM Shuttle Radar Topography Mission

TOPS Terrain Observation by Progressive Scans

UPC Universitat Politècnica de Catalunya

UTC Coordinated Universal Time

V-LMRTA Variogram Weighted LMRTA

WGS84 World Geodetic System 1984

WPS WRF Preprocessing System

WRF Weather Research and Forecasting Model

ZTD Zenith Total Delay

1

Chapter 1
Introduction

Differential synthetic aperture radar interferometry (DInSAR), also known as Persistent Scatters Interferometry (PSI), has already proven to be an extraordinary geodetic approach for ground deformations measurement at large scale and high accuracy (centimeter to millimeter) related to earthquakes [1–3], tectonic movement [4,5], volcanic actions [6–8], and landslides [9, 10]. With the unprecedented development of SAR missions (such as Sentinel-1, TerraSAR-X, ALOS-2, COSMO-SkyMed, RADARSAT-2, PAZ, Gaofen-3 and the planned NISAR), large amounts of SAR data are or will be available with short repeat cycles and wide swath modes. It is therefore believed that InSAR technique can provide an efficient and near-real-time way for monitoring dynamic processes on the Earth's surface on a global scale [11–13]. Their high accuracy is achieved in correspondence to the high phase quality of interferograms, assuming they are not influenced by other phase components. However, atmospheric perturbation, hereafter called the APS, caused by the differences in humidity, temperature and pressure between two acquisitions, may induce additional fringes on differential interferograms. The extra fringes can result in a biased estimation of the geophysical signal from InSAR stacks. In the InSAR community, it is well known that the APS remains one of the major limitations for InSAR techniques, which cannot be ignored in order to retrieve useful geophysical information more reliably.

1.1 Atmospheric artifacts

Initial studies [10, 14–16] related to atmospheric artifacts in InSAR demonstrated that atmospheric perturbations are caused by temporal and spatial changes of the atmosphere state, such as temperature, pressure and humidity. Consequently, the refractivity of the

atmosphere is not constant. When microwaves get through the different atmospheric layers, the speed of propagation changes as the refractivity index does and the two-way trip delay is affected as well. Meanwhile, the state of the atmosphere is temporally dependent and it will be usually different at the times the two images of the interferogram had been acquired. As a result, additional fringes would appear in the interferogram not related with neither topography nor deformation. Atmospheric delays cannot be thus ignored because they can often be comparable, or even much larger, in magnitude to the geophysical signals of interest. For example, the work in [15] showed that spatial and temporal changes of just 20% in relative humidity can result in 10 *cm* errors in deformation products. The work in [16] reported that the atmospheric delay can be of the order of several centimeters. The same previous study by Hanssen [16] further showed that the atmospheric propagation delay in an interferogram can be categorized into vertical stratification and turbulence components mixing. In the former, APS correlates with topographic variations, while in the latter, APS presents a spatial correlation length that can typically be described by the slope of its power spectral density based on Kolmogorov's theory.

1.2 Compensation based on temporal-spatial filters

To remove the two categories of APS from interferograms, to date, numerous methods have been explored to mitigate APS, all of which generally can be summarised in three categories. The classical approaches in time series analysis take advantage of the properties of APS and deformation in the interferometric phase. Turbulent atmospheric phase artifacts are highly correlated in space, but they can be assumed to be uncorrelated in time. At the same time, the phase terms associated to deformation present a higher temporal correlation and, usually assumed, a lower spatial correlation. Thus, the phase terms coming from atmospheric artifacts can be estimated and partially removed from the interferometric phase by applying different spatial and temporal filters [17–20]. However, with no prior information about the atmospheric artifacts and/or the deformation signal characteristics, it is difficult to determine the proper shape/extension of the spatial filter and the optimal length of the temporal one. In order to optimize the filtering approaches, some researchers have tried to obtain the statistical properties of the atmospheric artifacts from auxiliary data (such as numerical weather prediction (NWP) products) as a priori information [21, 22]. It has been proved that this is an alternative method to improve atmospheric artifacts mitigation. Besides, the work in [23] studied the spatial autocorrelation of APS and its impact when retrieving geophysical signals. Although this approach is efficient with large datasets of SAR images under the assumption that atmospheric artifacts present a Gaussian distribution, it is still challenging in terms of filtering parameters optimization according with the atmospheric characteristics. There is always the risk of filtering in excess the deformation or contaminating the time-series with atmospheric noise.

1.3 Compensation based on empirical models

Another class of techniques considers that APS is correlated with topography [24], which can happen in mountainous areas. Stratified APS contribution in interferograms can be modelled by analysing the phase-elevation relationship with a linear model [25–28]. To estimate the stratified APS more accurately, recent improvements have been made by analysing phase-elevation relationship with a multiple-regression model [29]. In addition, a power law model has also been applied to remove tropospheric APS, which accounts for the spatial variation of the tropospheric properties [30]. The main limitation of these model related methods is that other phase terms (e.g., turbulent atmospheric artifacts, deformation related phase, decorrelation noise) can influence the estimate of the coefficient that relates phase with elevation. In practice, Persistent Scatters (PSs) are usually selected to calculate the coefficient in order to reduce the impact of decorrelation noise. Although such attempt can be more effective to some extent [31], the influence of turbulent atmospheric artifacts can not be neglected. If the real situation fails to meet the basic assumption that the observed phase is stratified APS only, or in other words if the stratified and turbulent APS are mixed, current phase-elevation based methods may obtain an incorrect coefficient estimation.

1.4 Compensation based on ancillary observation data

The third category of mitigation methods utilize various auxiliary information sources, which include Zenith Total Delay (ZTD) from GPS measurement [32–36], multi-spectral observations [37,38] and either local meteorological models [39–42] or Global Atmospheric Models (GAM) [27, 43]. The main drawbacks reported from the above mentioned references are the low spatial and/or temporal resolution and precision of the external datasets. Although [44] proposed a framework to correct APS routinely using a GPS-based method, GPS stations are still sparsely distributed or even absent in many regions. Additionally, some GPS datasets are still not freely available to the public. Fortunately, with the development of the numerical weather prediction, GAM are able to provide accurate and higher resolution parameters for characterizing the atmosphere state, such as ERA5 data generated using Copernicus Climate Change Service Information [45]. Moreover, the GAM datasets (e.g. ERA-Interim, ERA5, MERRA2) are freely available to the public on a global scale. Consequently, GAM based methods are considered as a promising and practical technique for APS mitigation. Previous studies have validated the potential ability of using GAM [27, 43, 46], in which the zenith path delay is estimated firstly, and then the phase delay along LOS direction is obtained geometrically by considering the incidence angle. However, in real situations, the calculation based on converting zenith to LOS direction (hereafter called Z-LOS approach) can produce biases if the atmospheric delay is spatially anisotropic, especially in cases where the incidence angle is big. Some other studies [47, 48] have introduced a direct integration method along LOS direction (hereafter called D-LOS approach) based on GAM. However, the magnitude of the difference between Z-LOS and D-LOS method has not been carefully compared and analysed in previous studies. Consequently, the Z-LOS method, which is an approximate calculation strategy compared to D-LOS method, is still widely used in recent studies [43, 49, 50].

1.5 Motivation

From the aforementioned research background, each type of method has the ability to remove atmospheric artifacts to some extent. Filtering approaches always aim at turbulent APS estimation, while modelling methods can estimate and mitigate the topography-related APS to some extent. Ancillary data, like weather forecast models, can partially provide both turbulent and stratified signals. However, There still exist some aspects remaining to be improved or further analysed in APS mitigation, with a few topics studied in this thesis.

1. In stratified and turbulent mixed situations, stratified APS can influence the performance of the filtering-based methods. On the contrary, estimating stratified components using conventional linear models is not accurate in situations where the turbulent component exists. Facing the dilemma, is it possible to mitigate one type of atmospheric artifacts more accurately by considering the characteristics of the other type of atmospheric artifacts?

In order to address this issue, we proposed a new stratified APS correction technique that can be applied to mountainous areas in which the topography-related and turbulent APS are mixed together. As the turbulent component is correlated in space while the stratified one is correlated with topography, the proposed method is based on utilizing the phase differences among nearby pixels, which are within the correlation distance of turbulent APS, to estimate the coefficient value of a linear model. The biggest improvement of this technique is that the influence of turbulent components are minimized when modelling the stratified APS.

2. In term of weather forecast model based mitigation methods, most attempts made by other researchers calculate the APS with an approximate assumption, i.e., integrating atmospheric parameters along zenith direction. Only a few attempts consider integration along the realistic LOS path. Is the difference between zenith and LOS method small enough to be ignored?

In this thesis, in order to avoid errors caused by the anisotropic behaviour of atmosphere, the D-LOS methodology based on GAM data is implemented by considering the realistic path between satellites and ground points. The D-LOS method is explicitly validated with Sentinel-1 data in Tenerife island (Spain) and applied also to Almería (Spain) and Crete island (Greece) test sites, emphasizing the comparison to zenith approach. The performance of the advanced method in all sites demonstrates its robustness and capability of mitigating APS.

3. A various of global weather forecast models are available to the public. Which one is better for atmospheric artifacts mitigating in InSAR applications?

The well-known global weather forecast models are the Integrated Forecast System (IFS) from the European Center for Medium-Range Weather Forecasts (ECMWF) and the Goddard Earth Observing System Data Assimilation System Version 5 (GEOS-5) from the National Aeronautics and Space Administration (NASA), providing ERA-Interim, ERA5 and MERRA2 global reanalysis data. In this thesis, the realistic integration method is applied to the three global reanalysis in three test sites (Tenerife, Almería, Crete), in order to figure out the best performance of current global forecast data.

4. Compared to global weather forecast data, local numerical weather prediction models, such as WRF, are able to provide atmospheric parameters with much higher spatial and temporal resolution. Can the higher resolution local data perform better than global forecast data in APS compensation?

Using global weather forecast data as initial and boundary conditions, the local numerical weather prediction models have the ability to simulate atmospheric conditions more locally. Many researchers may believe the local ones can achieve a better APS mitigation compared to the global ones. In this study, the advanced WRF model is taken as an example for APS correction, compared to the global reanalysis data. Furthermore, based on the latest global ERA5 data as initial conditions, different model settings are also tested in our cases.

1.6 Objectives of the thesis

The aim of this thesis is to mitigate atmospheric artifacts as much as possible for InSAR techniques. To achieve this research target, the detailed objectives are defined as follows.

- Develop a covariance-weighted linear empirical model to mitigate tropospheric delay for InSAR techniques.
- Develop a realistic integration method based on numerical weather forecast data to correct APS for interferograms, emphasizing the comparison with conventional zenith-based method.
- Assess the performance of different global atmospheric reanalysis data using the realistic integration method for APS compensation.
- Evaluate the performance of the realistic integration method based on the local WRF model by adjusting model setups, using the latest global ERA5 data as the initial meteorological conditions.

1.7 Structure of the thesis

- Chapter 1 introduces the motivation of APS mitigation in the InSAR community, the state-of-the-art of APS compensation techniques, as well as the outline of the thesis.
- Chapter 2 introduces the basic concepts related to SAR, InSAR, Differential SAR Interferometry (DInSAR), multi-temporal InSAR techniques and the SUBSIDENCE-GUI software used in this thesis. Besides, several factors limiting the InSAR applications, especially the tropospheric phase delay, are also explained in this Chapter.
- In Chapter 3, a covariance-weighted empirical linear model method based on InSAR data has been developed to correct APS for interferograms. The proposed method is explicitly evaluated in Tenerife island, Spain. The assessment is carried out by analysing phase dispersion of residual phase after APS correction. The traditional linear model method and ERA5 correction result are referred as comparison.

- Chapter 4 explains a realistic integration method along LOS path to simulate tropospheric delay based on the global meteorological reanalysis ERA5 data. The accurate method is implemented step by step in Tenerife, Spain and is applied to Almería, Spain as well as Crete, Greece in this Chapter. A detailed comparison and great improvement can be found in the three test sites, compared to conventional zenith direction based method. Moreover, the advanced method is also applied to other global reanalysis data, such as ERA-Interim, MERRA2. Readers may take our experience as a reference to choose the proper global data for APS compensation.

- In Chapter 5, the realistic LOS integration method is applied on the local weather forecast WRF model to mitigate APS. Compared to global weather forecast models, the WRF model is able to predict atmospheric parameters in a relative high spatial resolution (up to 1 km). Therefore, it is expected that the local WRF model may demonstrate a better performance than the original global reanalysis data. In this Chapter, although the WRF model setups are carefully adjusted, the performance of the WRF model is just on the contrary to the expectations.

- In Chapter 6, all the developed methods in this thesis are applied to Gansu, China test site, where deformation signal and strong atmospheric artifacts exist in a single interferogram simultaneously. The feasibility and performance of these APS correction methods has been further proven to separate the two mixed signals in a real situation.

- The conclusions and future research lines are summarised in Chapter 7.

2

Chapter 2

InSAR and tropospheric delay on InSAR

This Chapter is intended to introduce the fundamentals involved in this thesis such as SAR, InSAR, DInSAR as well as the sources of errors. Among the limitation factors, tropospheric phase delay is the main error source that will be mitigated in the thesis.

2.1 SAR

A space-borne SAR system is an active imaging radar mounted on an aircraft or satellite. Compared with the passive optical sensors, it can obtain complex reflectivity images of the Earth surface in all-weather day-and-night conditions. In addition, radar remote sensing has advantages on its sensitivity to dielectric properties, surface roughness, man made objects, target structure and accurate distance measurements.

The first space-borne SAR experiments were performed by Carl Wiley on a validation system known as DOUSER in 1950s at Goodyear, Arizona [51]. After the initial test, a big step moving forward came with the experiences of the L-band airborne SAR system onboard Seasat in the 1960s and 1970s. The next milestone of SAR system is related to the success of SIR-A and SIR-B Space Shuttle missions in L-band by NASA in the early 1980s. Based on the success of the mentioned SAR missions, European Space Agency (ESA) launched its first C-band SAR satellite in 1991: European Remote Sensing Satellite (ERS-1) and later in 1995, the twin of ERS-1: ERS-2 was launched. The spectacular SAR images from the twins preserved an excellent phase quality and thus the twins

satellites indeed shaped the radar interferometry community. Afterwards, Japan launched L-band Japanese Earth-Resources satellite (JERS) in 1992. Unfortunately, the bad orbit control and maintenance limited its practical usage for interferometry. Canadian Space Agency (CSA) jointed to the study of SAR and launched its C-band satellite Radarsat in 1995. Similar to the Japanese JERS, the orbit was not as precise as designed, which limited its interferometry applications. The attempts and experience with SAR system missions culminated in the Shuttle Radar Topography Mission (SRTM) mission, conducted between 11 and 23 February 2000 by NASA. The Space Shuttle mission mainly carried two radar antennas in C and X band with a fixed 60 m boom to obtain a pair of SAR images simultaneously. The zero temporal baseline can avoid temporal decorrelation and atmospheric artifacts. The C-band system was designed to topographic mapping for about 80% of the land surface of the Earth. The X-band data can produce topographic maps at a higher resolution than the C-band data, but cannot have the near-global coverage. All the mentioned SAR missions helped to shape and promote the development of SAR system designs, SAR interferometry and variety of SAR-based applications. Afterwards, more and more advanced, stable SAR satellites successors have been launched to the space to provide new data and information of the Earth. Among them, the most significant ones are Envisat, Advanced Land Observation Satellite (ALOS)-1, Radarsat-2, TerraSAR-X, COSMO-SkyMed, TanDEM-X, ALOS-2, etc. These satellites have been providing large amounts of SAR data with high quality for the scientific research and commercial applications. It is important to remark that the new generation SAR satellite of ESA, Sentinel-1, has an unparalleled mapping capacity in a reliable, continuous and continent-wide way since its launch in 2014 for Sentinel-1A and 2016 for Sentinel-1B. Recently, China also joined in it and launched its first C-band Gaofen-3 SAR satellite in August 2016. Besides, Paz, a Spanish Earth observation and reconnaissance satellite, was launched on 22 February 2018, which is operated in a constellation with the German SAR fleet TerraSAR-X and TanDEM-X on the same orbit. A sensational news in the SAR community is the start-up company ICEYE, who will launch the largest satellite constellation of 18 microsatellites equipped with SAR sensors in the world by the end of 2019 [52]. By now, ICEYE-X1, the first satellite under 100 kilograms, was launched in January 2018 successfully and ICEYE-X2 satellite was also delivered into orbit by SpaceX Falcon9 rocket on December 2018. Nowadays, SAR has been in a golden age. More than 15 space-borne SAR satellites are being in service and many new SAR systems will be launched in the near future [53]. With all the SAR satellites and data distribution policy, SAR data issues become a thing of the past. Fig. 2.1 provides an overview of historical and current SAR satellites and their status.

The space-borne SAR sensors have a side-looking imaging geometry and are always mounted on a moving platform, traveling in the along-track or azimuth direction. The perpendicular to the flight path is called across-track or slant range direction. For the sake of simplicity, illustration of a typical stripmap SAR is shown in Fig. 2.2, showing the acquisition system and SAR imaging geometry. The illuminated area is called footprint. Under the imaging geometry, the SAR coordinate system is defined in two-dimensions by the azimuth and slant range directions. Thus, complex reflectivity images of the Earth obtained from a SAR system are in two-dimensions. The active radar system transmits electromagnetic pulses with high power and at the same time receives the echoes of the backscattered signal. From the received amplitude and phase of the backscattered signal, the radar is able to extract certain information of the reflecting objects such as geometry,

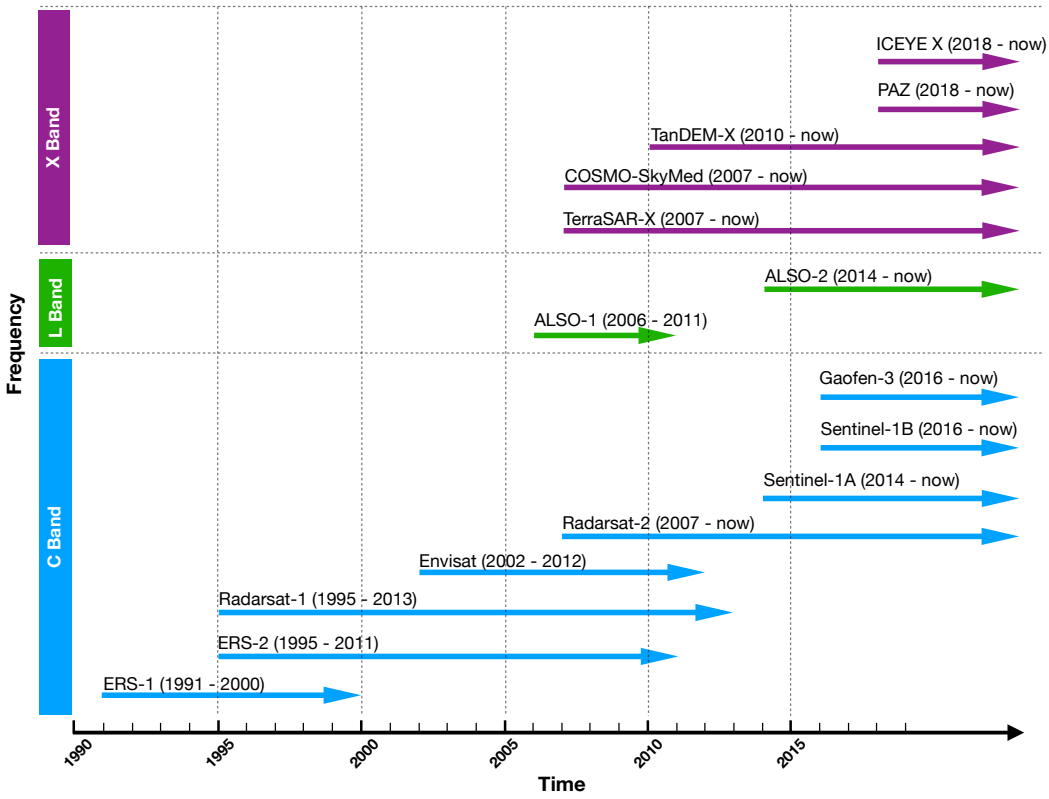

Fig. 2.1. Historical and current SAR satellites.

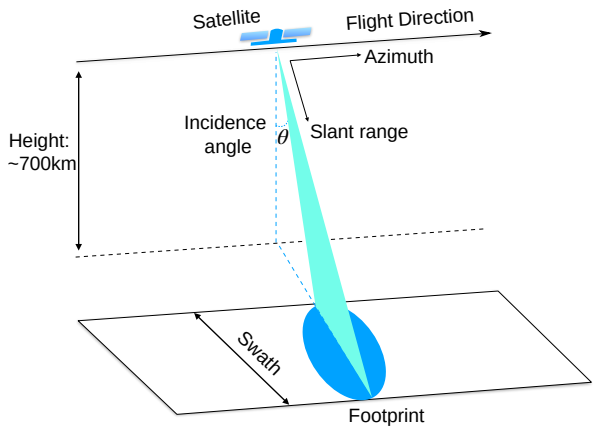

Fig. 2.2. An example of SAR geometrical configuration.

roughness and electrical properties. However, visualizing raw SAR data does not give any visible information of the scene. The raw data acquired by the sensor has to be

focused in range and azimuth directions to obtain, after some processing, the Single Look Complex (SLC), in which phase as well as amplitude are preserved for InSAR processing afterwards. The amplitude in the complex SLC images is associated to the backscattering coefficient of the ground target and the phase records the travelled distance information. The phase of a SAR image can be expressed as [54]

$$\varphi = -\frac{4\pi}{\lambda} \cdot r + \varphi_{scattering} \tag{2.1}$$

Where λ is the wavelength, r is the range associated to travel path from the sensor and ground and $\varphi_{scattering}$ is the phase due to the target backscattering property.

Based on the complex images, both amplitude and phase can be utilized for many applications. On the one hand, amplitude and phase information can be used for change detection, moving target indication and etc. Fig. 2.3 shows one example of amplitude of SAR image (Barcelona area) acquired by PAZ (Fig. 2.3(a)) and Gaofen-3 satellite (Fig. 2.3(b)). On the other hand, the SAR community mainly takes advantage of the phase information by making interferometry processing based on multiple images. The derived techniques include InSAR for topography construction, DInSAR for displacements measuring such as volcano and earthquake monitoring and Polarimetric SAR Interferometry (Pol-InSAR) for forestry such as forest height estimation.

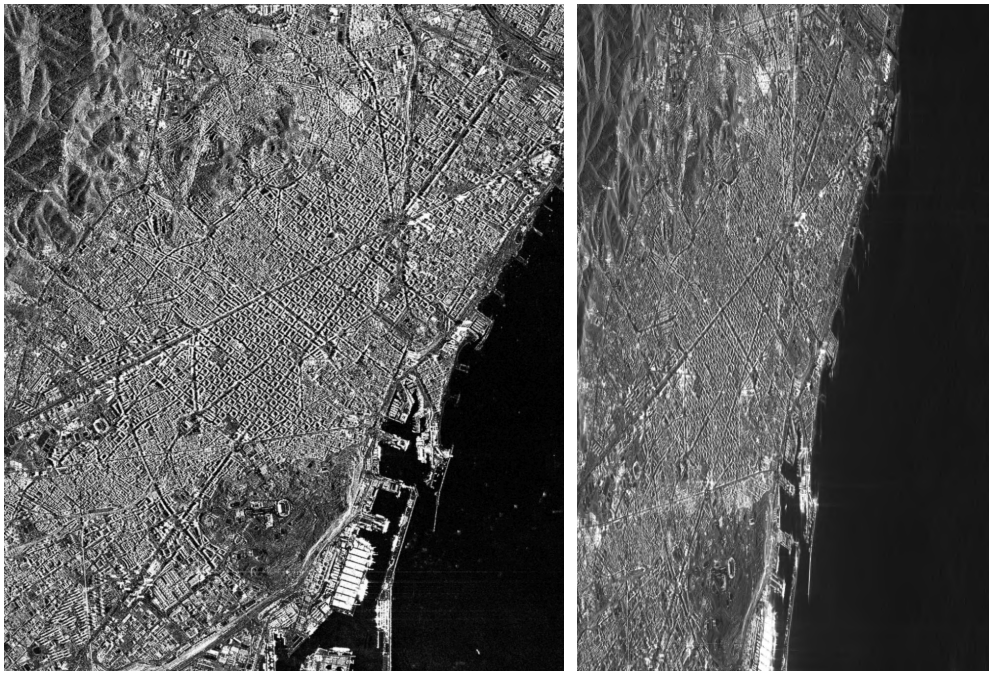

(a) **(b)**

Fig. 2.3. Amplitude of PAZ and Gaofen-3 SAR images over Barcelona. (a) Amplitude of stripmap SAR image acquired by PAZ on 26 April, 2018. (b) Amplitude of spotlight mode SAR image acquired by Gaofen-3 on 19 November, 2018.

2.2 InSAR and DInSAR

InSAR is a well-established remote sensing technique that has the ability to measure geophysical parameters such as topography, ground subsidence as well as structure stability with high accuracy. The key idea of InSAR is to combine phase component of two SAR images acquired from slightly different orbital positions and/or at different times. The so called interferogram is the new product of interferometry processing, which is conducted by the following equation based on two SLC images [55].

$$I = S_1 S_2^* \tag{2.2}$$

Where I is the interferometric phase, S_1, S_2 are the two SLC images. According to Eq. (2.1), interferometric phase ϕ of a single pixel in an interferogram can be expressed as:

$$\phi = -\frac{4\pi}{\lambda} \cdot (r_1 - r_2) + (\varphi_{scattering1} - \varphi_{scattering2}) \tag{2.3}$$

In Eq. (2.3), as the backscattering characteristics of targets have not changed between the two acquisitions, the backscattering components $\varphi_{scattering1}$ and $\varphi_{scattering2}$ are very similar. Then the interferometric phase in Eq. (2.3) only depends on distance factors r. It is also important to point out that the measured distances are influenced, in practice, by some factors for example atmospheric artifacts and other sources of noise. The relation between phase and geophysical information is not clear until the Eq. (2.3) is derived to more specific parameters. By means of geometry calculation, the interferometric phase can be derived to geophysical components related to topography, deformation and others as [16]:

$$\Delta\phi = \frac{4\pi}{\lambda r_0} \cdot \frac{B_n \cdot \Delta r}{tan\theta} + \frac{4\pi}{\lambda r_0} \cdot \frac{B_n \cdot \Delta h}{sin\theta} + \frac{4\pi}{\lambda} \cdot \Delta\rho + \Delta\phi_{APS} + \Delta\phi_{noise} \tag{2.4}$$

The variables in Eq. (2.4) are:

- $\Delta\phi$: the phase difference between two pixels in an interferogram.
- λ: the wavelength of the carrier frequency.
- r_0: the distance between the sensor and the terrain, usually known as range.
- θ: the local incidence angle.
- B_n: the perpendicular baseline.
- Δr: the difference of range between two pixels.
- Δh: the topographic difference between two pixels.
- $\Delta\rho$: the deformation difference in range direction between two pixels.
- $\Delta\phi_{APS}$: the atmospheric artifacts.
- $\Delta\phi_{noise}$: other noise terms.

The interferometric phase $\Delta\phi$ in Eq. (2.4) consists of several phase components as follows:

- $\frac{4\pi}{\lambda r_0} \cdot \frac{B_n \cdot \Delta r}{tan\theta}$: The phase component is so called flat Earth contribution ϕ_{flat}, which is a phase ramp from the near-range to the far-range.
- $\frac{4\pi}{\lambda r_0} \cdot \frac{B_n \cdot \Delta h}{sin\theta}$: This phase refers to topographic information. The terminology for it is ϕ_{topo} in the InSAR community. The phase value depends on spatial baseline as well as height difference between two pixels.
- $\frac{4\pi}{\lambda} \cdot \Delta\rho$: This term is the main phase component ϕ_{def} for deformation measurement.
- $\Delta\phi_{APS}$: The atmospheric phase term ϕ_{APS} is caused by different atmospheric status between two SAR images acquisitions. It is the main error source to be solved in the thesis.

Focusing on the different phase components in Eq. (2.4), InSAR techniques exploit the phase information in a variety of applications, which are described in Section 2.3.

DInSAR is the main branch of InSAR based techniques. If deformation information is the main purpose, then DInSAR is the tailored technique to measure the displacements. By using an external DEM, the topographic phase and flat phase components can be extracted from the interferogram, leading to a differential SAR interferogram in which the main residual phase item refers to displacement between two acquisitions. Theoretically, DInSAR can achieve an accuracy in the order of the wavelength along the LOS direction. However several aspects limit the performance of this technique. Section 2.4 will explain details of the error factors.

Fig. 2.4 illuminates an example of an interferogram (Fig. 2.4(a)) and the differential interferogram (Fig. 2.4(b)) after removing topographic information over Mojave, California obtained with two PAZ images acquired with 11 days time span. The deformation phase component should be the only term that remains in the differential interferogram.

2.3 InSAR derived techniques and their applications

In the beginning, SAR images were mainly interesting from the science and engineering point of view. Nowadays, more and more public departments are aware of its usefulness and importance in different application fields due to its all-weather day-and-night imaging capability.

As described in Eq. (2.4), their phase components are related with different geophysical parameters. If we pay attention to the topographic phase item ϕ_{topo}, it opens the door to topography estimation applications. This can be achieved by eliminating the flat Earth phase component, and reducing other noise phase contributions (deformation, atmospheric artifacts, etc.) as much as possible. In order to reduce the impact of deformation, two SAR acquisitions with a short time interval are usually chosen. Regarding atmospheric variability, interferograms with apparent APS are abandoned. After removing the flat Earth component, a phase unwrapping process has to be applied to the residual phase. And then, the unwrapped phase can be converted into height and the reference

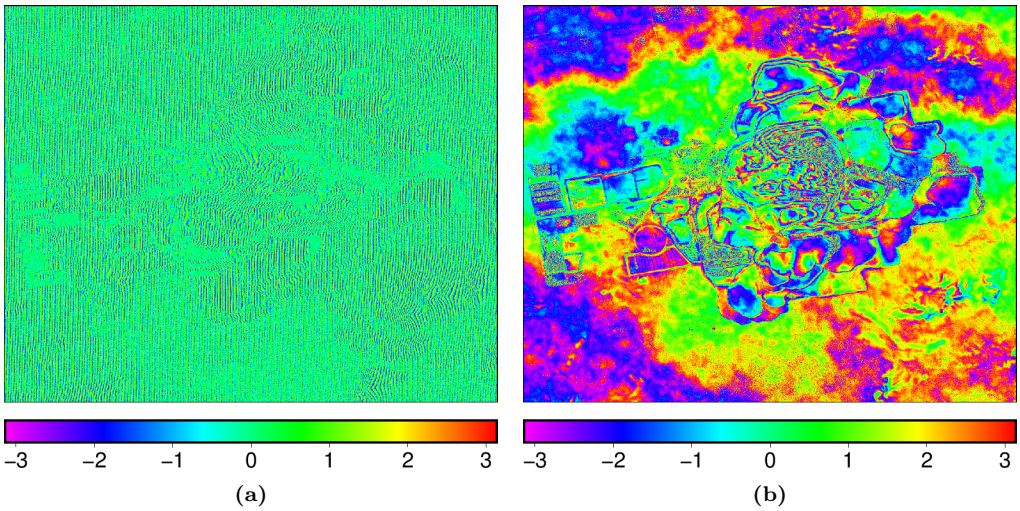

Fig. 2.4. An example of one interferogram (a) and differential interferogram (b) from two SLC images acquired by PAZ over Mojave, California on May 20th and May 31st 2018.

altitude can be calibrated through known points. The early experiment can trace back to the reference [56], in which a topographic map of a portion of the San Fracisco Bay Area was derived. A mature and eminent application was the SRTM mission, using single-pass interferometry. As the data were acquired at the same time, atmospheric influence and deformation signal were reduced to minimum. This mission obtained the most complete high-resolution digital topographic database of the Earth on a near-global scale during only 11 days in February 2000. TanDEM-X is another milestone of topography measurement by using SAR. TanDEM-X allows the generation of the WorldDEM with an unprecedented accuracy, coverage and quality. Available since 2014, WorldDEM is to feature a vertical accuracy of 2 m (relative) and 4 m (absolute) [57].

In Eq. (2.4), DInSAR and its derived PSI techniques are focused on phase component related to terrain deformation. These techniques have already proven to be extraordinary geodetic approaches for large scale and high accuracy ground deformations measurement to monitor and characterize earthquakes [1–3], tectonic movements [4, 5], volcanic actions [6–8], landslides [9, 10] and subsidence phenomena [58, 59]. With the unprecedented development of SAR missions (such as Sentinel-1, TerraSAR-X and TanDEM-X, ALOS-2, COSMO-SkyMed, RADARSAT-2, PAZ, Gaofen-3 and the planned NISAR), large amounts of SAR data are or will be available with short repeat cycles and wide swath modes. It is therefore believed that DInSAR techniques can provide an efficient and near-real-time way for monitoring dynamic processes on the Earth's surface on a global scale [11–13].

In the last decade, SAR based techniques have extended to Pol-InSAR [60] for obtaining information of volume scatterers [61]. Scattering polarimetry is sensitive to the shape, orientation, and dielectric properties of scatterers. This allows the identification and separation of different scattering mechanisms of natural and artificial volume scatterers [60, 62]. There are three main application fields of Pol-InSAR techniques. Firstly, it

has the ability to investigate the three-dimensional structure of vegetation cover. In [63], a first-order estimator for tree height was introduced based on the phase difference between interferograms acquired at different polarisations. In [60], an inversion algorithm based on a coherent scattering model was introduced for the estimation of forest height, average forest extinction, and underlying topography. Secondly, Pol-InSAR is also developed for the quantitative estimation of agricultural vegetation [64, 65]. In literature [66], researchers demonstrated the retrieval of vegetation height from agricultural crops by means of Pol-InSAR technique. The most challenging applications of Pol-InSAR are with respect to understanding ice layering and snow depth [53, 67, 68]. However, the development by now is in the early stage, on account of limited experimental and validation data, as well as the limited understanding of the coherent interaction with ice volumes.

2.4 Coherence and error sources

The performance of any InSAR technique relies on the phase quality of the interferograms. Several aspects usually contaminate the interferometric phase, influencing its accuracy or even making this technique unreliable. These errors sources can have a small correlation length, also defined as decorrelation, and a large correlation length, such as APS and orbital errors.

2.4.1 Coherence

The main parameter to evaluate the interferometric phase quality is coherence, which is defined as [16]:

$$\gamma = \frac{E\left\{S_1 S_2^*\right\}}{\sqrt{E\left\{\left|S_1\right|^2\right\} E\left\{\left|S_2\right|^2\right\}}}, \quad 0 \leq \gamma \leq 1 \tag{2.5}$$

where S_1 and S_2 is a pixel from the master and slave image, $E\{\cdot\}$ means the expectation operator and $|\cdot|$ stands for the modulus operator. Based on this definition, in theory, the expectation values in Eq. (2.5) are obtained by using an ensemble average from multiple observations for each pixel. In other words, large amounts of interferograms are acquired simultaneously under the same circumstances. Then an ensemble average is applied to obtain the expectation values. Unfortunately, in the real case, every pixel is observed only once during each SAR acquisition. So, in practice, it is assumed that the accuracy of phase observations is stationary. Under the assumption of ergodicity, the expectation operator is replaced by averaging in space. This assumption is used to obtain the maximum likelihood estimator as [16]:

$$|\hat{\gamma}| = \frac{\left|\sum_{n=1}^{N} S_1^{(n)} S_2^{*(n)}\right|}{\sqrt{\sum_{n=1}^{N}\left|S_1^{(n)}\right|^2 \sum_{n=1}^{N}\left|S_2^{(n)}\right|^2}} \tag{2.6}$$

where N is the estimation window.

The coherence magnitude $|\gamma|$ can be expressed as a function of the Signal-to-Noise Ratio (SNR) of the interferogram as follows:

$$|\gamma| = \frac{SNR}{SNR + 1} \tag{2.7}$$

The absolute value of the coherence, ranging from 0 to 1, can be used as a measure for the quality of the interferogram. A zero coherence stands for a totally uncorrelated scene, while a coherence close to one accounts for a perfect interferogram. Fig. 2.5 presents an example of coherence image obtained from a pair of stripmap SAR images acquired by PAZ over Mojave, California. A short temporal baseline (11 days) allows obtaining a terrific quality interferogram, presenting high values in the coherence map.

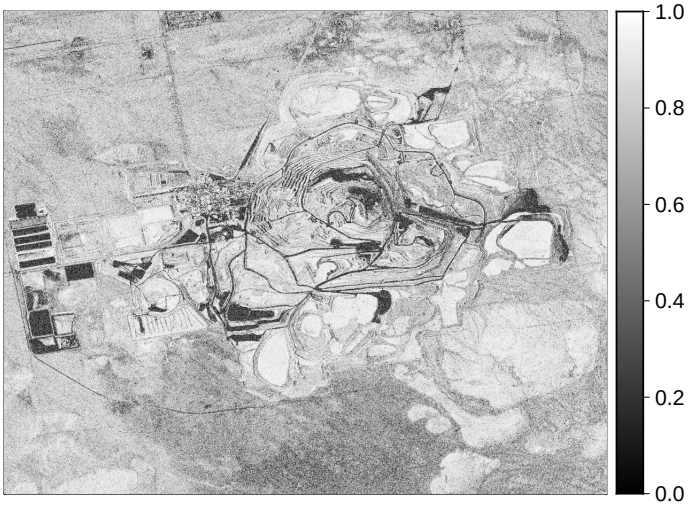

Fig. 2.5. The coherence map calculated from two SAR images acquired by PAZ over Mojave, California on May 20th and May 31st 2018. The estimation window is 5x5.

2.4.2 Decorrelation factors

The phase quality of an interferogram can be affected by several aspects. The decorrelation is defined as the noise caused by error sources that have a correlation length smaller than a regular coherence window. This category of error source does affect the coherence. Several sources of decorrelation are listed as follows [16]:

- **Temporal decorrelation.** An interferogram is usually formed by repeat-pass of SAR acquisitions. During the two acquisitions, the surface of the observed terrain cannot remain unchanged. Surface changes will definitely influence the phase quality of an interferograms, which is called temporal decorrelation. The temporal decorrelation could be caused by several physical mechanisms, ranging from weather events, human-driven land-cover change to vegetation phenology (such as the presence of a snow layer in winter seasons) [69]. It is difficult to assess the amount of

temporal decorrelation, as it depends on stochastic factors, such as the structure of the scatterers, environmental processes occurring between the SAR acquisitions. Meanwhile, proper temporal baselines are in favor of terrain deformation retrieve. As a rule of thumb the decorrelation rate for temporal baselines is on the order of 30-45 days at C and L band radar frequency provided by the data of the ESA and JERS missions [70].

- **Geometric decorrelation.** In the case of repeat-pass interferometry, two SAR images, forming an interferogram, are acquired from different looking directions. The slightly different observation angle can introduce a spectral shift in the range direction between two images. Note that when generating an interferogram, only the common part of spectra is useful, while the non-common band contributes noise in the interferogram. Therefore, in order to reduce the geometrical decorrelation, a common-band filtering is preferred to be applied.

- **Volume scattering.** This decorrelation source is caused by penetration of the radar waves in the scattering medium. When observing targets within the resolution cell with different heights, backscattering from different heights leads to a spectral shift in the height direction. The volume decorrelation depends on the radar wavelengths, height distribution of the targets and the scattering medium.

- **Doppler Centroid.** This decorrelation source is similar with the geometric decorrelation factor, but it is corresponding to spectral shift in azimuth direction. This is caused by the Doppler centroid differences between SAR acquisitions. Similar to the geometric one, azimuth filtering can improve the interferogram quality.

- **Misregistration.** Prior to generating an interferogram, a precise coregistration process is essential. Misregistration introduces loss of the coherence, i.e., degrading the quality of interferometric phase. It is reported in the reference [71] that an accuracy of 0.1 pixels is usually sufficient to obtain high-quality interferograms for conventional stripmap acquisition mode. For Terrain Observation by Progressive Scans (TOPS) mode, the registration requirement is much more demanding [72].

- **Thermal decorrelation.** The influence of thermal noise depends on the SNR of a specific SAR system.

2.4.3 Other sources of error

There are other sources of errors that have a correlation length larger than a regular coherence estimation window. Although they do not have any impact on the coherence, they do affect the interferometric phase in interferograms [16].

- **Orbital errors.** For the purpose of topographic mapping or terrain deformation retrieve, the flat Earth phase and topographic phase contributions in Eq. (2.4) need to be subtracted firstly. In order to do this, the orbit information of the two SAR acquisitions are crucial. If significant orbital errors exist, in general a phase ramp or orbital fringes will appear in the residual phase. The more accurate of the orbit vector is, the less errors would be propagated to the deformation maps or

topographic height. In order to mitigate the effects of the orbital errors, tie points distributed over the whole processing area can be used to constrain the reference phase. Note that the tie points should be carefully selected from stable area, without contamination by other phase components, such as atmospheric delays or ground deformation. Nowadays, the modern SAR satellites, Sentinel-1 for example are flying in a small orbit tube with radius of 50 m (rms), which provides small InSAR baselines with small orbital errors.

- **Digital Elevation Model (DEM) error.** As mentioned in Eq. (2.4), topographic phase is one of the important components in an interferogram. It requires to be removed when the purpose is estimating the ground deformation or refining the topography. In practice, it is accomplished by using an approximate DEM. Therefore an approximate DEM will introduce errors to the remaining phases. Fortunately, the DEM error is proportional to the perpendicular baselines of interferograms. Thus, an uniform distribution of spatial baselines is able to benefit the estimation of DEM error.

- **Atmospheric artifacts.** In addition to the above mentioned error sources, another important source of errors is atmospheric artifacts which usually cannot be neglected in topographic mapping or generating deformation maps. As it is known an interferogram is formed from two images with a temporal gap. Among the two acquisitions, spatio-temporal variations in the propagation medium can lead to a variable refractive index, which is mainly due to the water vapor content in the troposphere. As a result, the electromagnetic waves propagate at different velocities compared to the vacuum speed of the light. Thus the measured distance between the satellite and the ground points is affected by the variable refractive index. As any InSAR technique relies on the measured distance wrapped in the observation phase, the phase delays caused by the atmospheric artifacts can produce significant phase changes. The order of magnitude can be 2-4 meters [53]. In other reference, the phase delay can lead to 10-14 cm errors in deformation products if there is a 20% difference in the relative humidity [15].

  Based on their spatio-temporal characteristics, the atmospheric artifacts can be classified into two categories [16]. The first is height dependent phase delays, also known as stratified atmospheric artifacts. The second category is called turbulent mixing of water vapor component. Fig. 2.6 presents two examples of the atmospheric artifacts, dominating the phase component in each differential interferogram. The temporal baseline for the two interferograms is relatively short, therefore it is assumed that the deformation phase component is insignificant. In addition, the phase variation is clearly correlated with topography. Therefore it is reasonable to believe that it is the atmospheric artifacts that dominates the phase components in the two interferograms. Note that in the first case Fig. 2.6(a), the atmospheric phase delay can reach values up to 40 rad. While in the second case Fig. 2.6(b), the value is also up to 20 rad. Both are too significant to be ignored. The two examples will be further used as case studies in Chapter 4 and Chapter 6 to demonstrate the performance of APS correction based on weather forecast data.

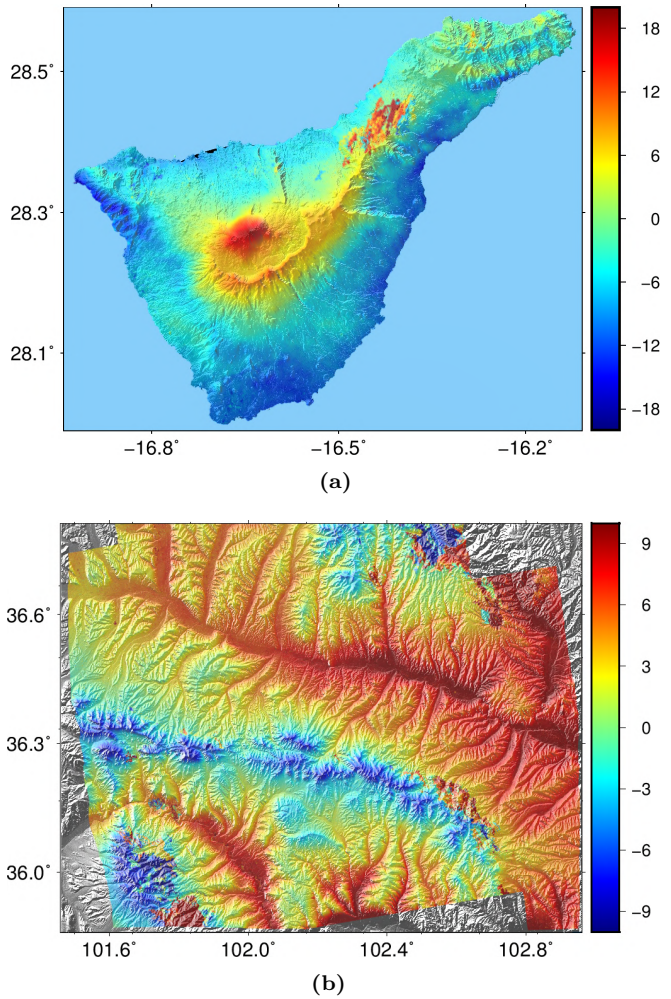

Fig. 2.6. Two examples of atmospheric artifacts. (a) shows the atmospheric artifacts existing in the interferogram 20160721-20160814 in Tenerife, Spain. (b) presents the APS affecting the interferogram 20160418-20160512 in Gansu, China.

2.5 PSI techniques and the Coherent Pixels Technique

As described in Section 2.4, several factors limit the practical use of DInSAR technique using just a single interferogram. Over the decades, PSI techniques, involving the processing of multiple-temporal interferograms, have enhanced the ability of deformation mapping with InSAR. The proposed PSI approaches can be broadly classified into two categories, namely, Permanent Scatters [17, 73, 74] and Small Baseline Subsets (SBAS) [18, 19, 75, 76]. The Coherent Pixels Technique (CPT) technique, containing the two mainstream approaches, has been developed and maintained by the CommSensLab in Universitat Politècnica de Catalunya (UPC) since the late 1990s. This tech-

nique is used in the PhD thesis and also the framework that the developed APS module is adapt to. This Section is to give an overview of PSI techniques and CPT.

Despite the many successful applications of DInSAR techniques, temporal and geometrical decorrelation often prevent standard techniques from being a fully operational tool for slow surface deformation monitoring in a long time period. In addition, atmospheric disturbances can strongly compromise the accuracy of the results. More importantly, the conventional DInSAR techniques based on two or three SAR images processing can only be applied to analyse a single deformation episode. With the increasing number of SAR images at disposal, from the end of the 1990s, the scientific community began to look for ways of addressing the limitations of conventional DInSAR techniques by processing multi-temporal sets of SAR images. Simultaneously, the interest of InSAR research community was moved from a single episode deformation towards the study of the time series analysis of the deformation. In this context, several approaches have been already developed and widely used [17, 18, 74–82]. Among these procedures, the one referred to as Persistent Scatterers SAR Interferometry (PSInSAR) [17, 74, 80] involves utilizing PSs, whose scattering characteristics remain stable over the whole observation period and when observed from slightly different looking angles. PSs can be identified depending on the characteristics of the targets. For instance, deterministic targets, which correspond to point-wise scatterers, can be identified through its amplitude stability or its spectral behavior along the dataset and they are only slightly affected by spatial and temporal decorrelation. These targets are also known as Permanent Scatterers. On the other side, Distributed Scatterers (DSs), corresponding to independent small scatterers within a resolution cell sharing similar reflectivity values, can be identified through its coherence along the generated interferograms. The former works at full image resolution and it is more suited for urban areas, while the latter with multi-look (averaged) interferograms is more adequate for rural areas.

The key issue of the PSI techniques is that the different phase terms (related with terrain motion, atmosphere and topography) can be estimated and separated due to their different dependencies with the temporal and spatial baselines and behaviors in time and space. Basically a model is adjusted to the interferometric data to obtain the linear terms and then a filter is used to separate the atmospheric artifacts and non-linear deformation. Finally the deformation time-series are obtained by combining the linear and non-linear deformations. Submeter DEM accuracy and millimetric terrain motion detection can be achieved after processing large datasets of images [17, 83, 84]. Sharing the same principles there are different implementations. The ones using the Permanent Scatterers approach [17] work at full resolution and with, at least theoretically, no restrictions regarding temporal and spatial baselines. Others, known as SBAS, involve making use of many multi-looked differential interferograms formed with small geometric and temporal baselines to limit the decorrelation phenomena [18, 19, 75, 85, 86]. Advantageously, the SBAS technique increases the temporal sampling rate by combining the different small base (SB) acquisition subsets.

Among these techniques mentioned above, the CPT technique is able to work with both approaches to estimate the linear and non-linear components of displacement. This technique is implemented in the SUBSIDENCE-GUI software. It is the achievement of many research work at CommSensLab, initially started at the mid 1990s [76, 87–89], later developed by several researches [20, 90–92]. With long-term development and a wealth of

experience, the SUBSIDENCE-GUI software is stable to process almost all SAR data from large variety of sensors, such as Radarsat-1/2, ALOS-1/2, Sentinel-1A/B, TerraSAR-X, COSMO-SkyMed, as well as GB-SAR data from RiskSAT sensor developed by the Comm-SensLab. Moreover, this software supports the entire processing chain from interferogram generation to final geophysical products such as geocoded deformation maps, DEM as well as time-series subsidence. These features are achieved by four main blocks: interferograms preparation and pixels selection, linear components estimation, non-linear term estimation and final product generation. The first block is designed to prepare the data for the following blocks. The linear block is focused on the estimation of linear parameters, namely the linear velocity of ground deformation and the topographic error term. After the linear block processing, the residual phases still contain non-linear contributions which are mainly composed of atmospheric artifacts and non-linear deformation. The following non-linear block is devoted to separate these components in order to obtain the time-series of the deformations. Finally, the product generation block is aimed at geocoding and projection of the results. An overview layout of the SUBSIDENCE-GUI software is shown in Fig. 2.7. The detailed explanation of each block will be presented in the following sections.

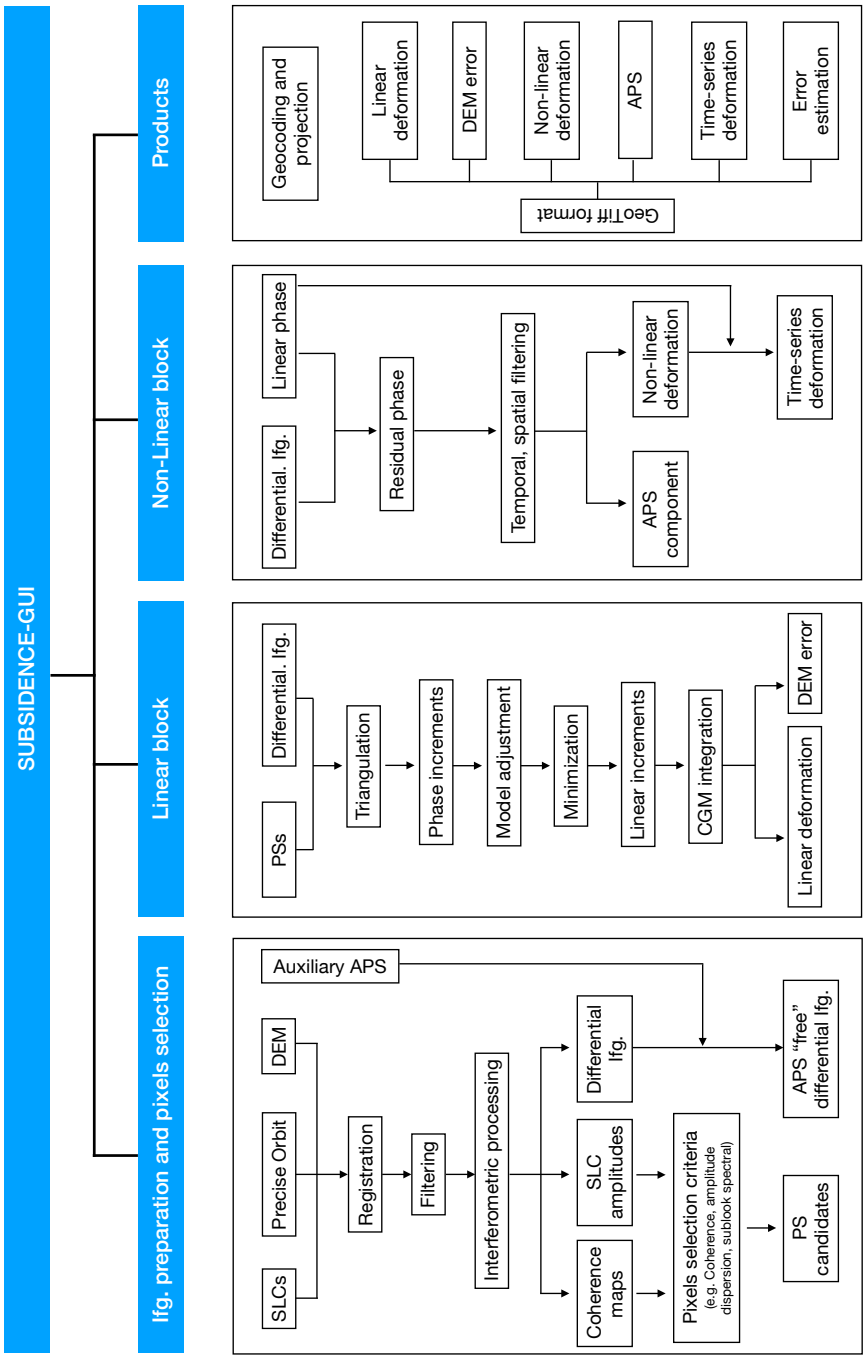

Fig. 2.7. Overview of CPT blocks and details in its sub-blocks.

2.5.1 Interferograms preparation and pixels selection

As mentioned in Section 2.5, the high accuracy of PSI approaches is only achieved in correspondence of interferograms and pixels with high phase quality. The higher the phase quality, the more reliable the final DInSAR products will be. In addition, the spatial and temporal distribution of interferograms also plays an important role in the linear parameters estimation. Therefore, prior to applying any DInSAR technique, it is mandatory to select interferograms with an appropriate distribution of baselines and pixels with high phase quality.

- **Interferograms selection.** The main purpose of this step is to generate a subset of interferograms for the later linear block. Several aspects have been studied related to interferograms selection for retrieving linear components better in the literature [20, 90]. In this Section, main features will be summarized.

  First of all, in the step of linear parameters estimation, a linear model containing linear deformation and DEM error is usually used to adjust to the interferograms. The linear model is as follow:

  $$\Delta\phi_{model} = \frac{4\pi}{\lambda} \cdot T \cdot \Delta v + \frac{4\pi}{\lambda} \cdot \frac{B}{r_0 \cdot \sin\theta} \cdot \Delta\varepsilon \tag{2.8}$$

  where T and B is the temporal and spatial baseline, r_0 is the distance between the satellite and the terrain, θ is the incidence angle, Δv and $\Delta\varepsilon$ are the linear deformation velocity and DEM error to be estimated.

  Actually, the basic idea of PSI techniques is that each individual interferogram can sample an episode of deformation and topography error. Thus in order to recover the signal precisely, the signal should be well sampled. The impact of distribution on the minimization function has been detailed analysed in the reference [93]. To summarize, as the linear deformation is related to the temporal baseline, a wide uniform distribution of temporal baselines is preferred to estimate the linear deformation. Similarly, the DEM error depends on the spatial baseline, a wide uniform distribution of spatial baselines is necessary to estimate this parameter accurately. In CPT, firstly, a 3D Delaunay triangulation, in the spatial, temporal baseline and Doppler frequency space, is applied to generate an initial subset of interferograms. At this stage, the initial subset still contains redundant information. In order to refine the selection, a Minimum Spanning Tree strategy is employed to the subset [93]. Furthermore, in practice, interferograms selection also depends on the main information to be retrieved from InSAR stack. For example, if the main goal is to obtain the linear deformation, an homogeneous distribution of temporal baselines and interferograms with short spatial baselines are preferable. The estimation of linear deformation will be better by degrading the reliability of DEM error estimation. The same principle can be applied to DEM error estimation.

- **Pixels selection.** In PSI techniques, only pixels preserving high quality phase are used to retrieve geophysical parameters. There are two mainstream categories of scatterers, i.e., PSs and DSs. PSs have stable phase history as the echo of the backscattered signal is dominated by a point-wise scatterer. DSs pixels, such as debris area, desert, are partially coherent throughout the time series of observation.

In order to select coherent pixels, two main criteria are available for the estimation of the pixels' quality. Firstly, the coherence value has been used as a criterion to evaluate pixels' phase quality. The pixels whose coherences are higher than a given threshold are selected as candidates for processing. This pixel selection criterion has been widely used in SBAS approaches [19, 82]. Secondly, the well-known amplitude dispersion value is used as a criterion to estimate the phase quality for PSs candidates when working at full resolution [17]. CPT can select stable pixels according to the nature of the scatterers and the number of available images by using both the coherence stability criterion and the amplitude criterion [20].

More recently, a new approach based on sub-look coherence was proposed to select stable scatterers [94] and implemented to CPT. It utilizes scatterers' spectral properties along time rather than their amplitude stability. Since this selection method uses a different stability characteristic of the scatterers compared to the conventional one, the combination of both approaches yields to a significant increase of pixels's density. Moreover, this method can be used to select reliable point-like scatterers with a reduced number of images.

2.5.2 CPT linear module

Time series deformation product generated by PSI techniques is composed of linear deformation and non-linear deformation. Linear deformation retrieve is one of the most important procedures in InSAR stack processing. In order to retrieve the linear deformation component, in general a linear model (refer to Eq. (2.8)) is adjusted to the well-selected interferograms. In addition to the linear deformation, DEM error component is also recovered by the linear model.

Once a proper set of interferograms and high quality pixels have been selected in the previous steps, the observed phase in interferograms should be organized appropriately, tailored for the linear model adjustment. The initial idea in CPT is to use arcs among selected pixels as new observation phase rather than absolute value of each pixel. It is well-known in the classic PSI [17] and SBAS [18] InSAR techniques, the phase unwrapping is compulsory. But by using arcs strategy, it can work with wrapped interferograms. In practice, a Delaunay triangulation is applied to the selected pixels to generate the arcs connecting neighboring pixels. Meanwhile, atmospheric artifacts are considered as a low spatial frequency signal [16], so using arcs also benefits the linear components estimation by reducing the influence of atmospheric artifacts.

The linear deformation and DEM error can be estimated by minimizing the following Model Adjustement Function (MAF) [76]:

$$\Gamma = \frac{1}{N}\sum_{i=1}^{N}\left|e^{-j\Delta\phi^{i}_{obs}} - e^{-j\Delta\phi^{i}_{model}}\right|^{2} \tag{2.9}$$

Where N is the number of interferograms, $\Delta\phi_{obs}$ is the phase for each arc in a differential interferogram and $\Delta\phi_{model}$ is the linear model described in Eq. (2.8). Note that this function is working in the complex space. So once again it can avoid potential error caused by phase unwrapping. The minimization function is applied to each arc. Once it is accomplished, the increment of linear deformation velocity and DEM error for each

relationship will be obtained. The next step is to convert the increment for each arc to the absolute value for each pixel. In order to achieve this goal, the Conjugate Gradient Method (CGM) algorithm has been used in CPT.

To summarize, Fig. 2.7 shows a detailed layout of the CPT linear module, consisting of triangulation, phase increments organization, model adjustment, linear increments estimation as well as CGM integration. As a result of the linear module, a deformation map and DEM error map will be generated.

2.5.3 CPT non-linear module

To obtain a complete ground deformation for a certain period, besides the above discussed linear deformation, non-linear deformation is also an important component to be retrieved. The non-linear deformation term is usually coupled with other phase components, mainly the atmospheric artifacts in the residual phase. The residual phase can be calculated as follow:

$$\Delta\phi_{res} = \Delta\phi_{intf} - \Delta\phi_{linear} \tag{2.10}$$

in which $\Delta\phi_{intf}$ is the phase in a differential interferogram. $\Delta\phi_{linear}$ is the estimated linear phase component, containing the linear deformation and DEM error.

In general, it is very difficult to retrieve the non-linear deformation accurately unless an accurate model in terms of its characteristics is available. There are two strategies to deal with the non-linear term in CPT. On the one hand, if a prior model or information about deformation is available, CPT is capable of integrating these models to differential interferograms to extract non-linear deformation phase component. For example, in coal mining areas, large-scale deformation usually occurs in a short temporal gap. It is the non-linear deformation that dominates the time-series deformation phenomena. For these areas, some models, such as the probability integration model, are usually able to predict the subsidence. Once the non-linear deformation is removed partially from the interferograms, it is believed the estimation for the linear term will be more reliable.

On the other hand, in most cases where prior information of non-linear deformation term is unavailable, a spatio-temporal filter is usually applied to the residual phase in order to decouple non-linear deformation and atmospheric artifacts. The filtering approaches take advantage of different spatio-temporal characteristics of atmospheric artifacts and non-linear deformation. Namely, atmospheric artifacts are correlated in space rather than in time, while on the contrary the deformation term is correlated in time, not in space. The filtering methods are effective, but it is impossible to separate them completely. In addition, as atmospheric artifacts can be obtained by auxiliary data, such as weather forecast data, it provides an alternative to retrieve the non-linear deformation by subtracting the estimated atmospheric artifacts.

2.5.4 CPT products module

Once the linear and non-linear modules have been completed, the SUBSIDENCE-GUI software ends up with the final products generation block, including geocoding, projection and geographical results formatting.

It is well well-known that SAR images are acquired under slant-range geometry, while for geoscience applications, maps with geographical coordinates are preferable. In order to generate user-friendly InSAR products, geocoding them to match the geometry of geographical information is one key step. In SUBSIDENCE-GUI, the general idea of geocoding is to establish the relationship between a general pixel at slant-range coordinate system and its coordinates at geographic geometry. In general, the relationship can be established based on precise orbit, geometry of SAR images acquisition, velocity of satellites and an external DEM. A detailed geocoding procedure in CPT has been explained in the literature [91].

In addition to geocoding, it is also worth pointing out that in practice projection should be taken into consideration in terms of the deformation term. SAR images are acquired under the slant-range coordinates and as a result, the retrieved displacement by InSAR techniques is only sensitive along the LOS direction. In fact, it is a projection of the real displacement. Hence, prior to applying the deformation products retrieved by InSAR techniques, a re-projection procedure should be realized. The projection algorithm implemented in CPT has been discussed explicitly in [90, 91].

After implementing the geocoding and projection, the software is able to generate all the geographical products, including deformation maps, time-series deformation, DEM error (or refined DEM) and atmospheric artifacts, in multiple formats, such as Keyhole Markup Language (KML), GeoTIFF.

3

Chapter 3

Empirical model for tropospheric delay compensation

Stratified atmospheric artifacts can be estimated with an empirical linear model as studied in some references [24–28, 31]. These studies have demonstrated the feasibility of mitigating stratified component in some cases. However, the estimation of coefficient for stratified APS is not always reliable if the turbulent component exists as well. On account of that the stratified APS and turbulent one present different characteristics, it is possible to refine the coefficient estimation for stratified component by taking the advantage of the spatial characteristics of turbulent atmospheric artifacts. In this Chapter, a covariance-weighted linear model based on the interferograms themselves has been proposed for correcting stratified APS more reliably. This Chapter starts with an introduction of conventional linear models, followed with a spatial covariance matrix estimation for characterising turbulent APS in Section 3.1. Section 3.2 demonstrates the feasibility of the proposed method with simulated data. After that in Section 3.3, the developed method is evaluated in Tenerife island, Spain, including phase dispersion analyses as well as comparison with the global weather forecast data ERA5 correction method.

3.1 Covariance weighted linear model

3.1.1 Weighted linear model to estimate stratified APS

In mountainous areas stratified APS linearly correlates with topography, which can be modelled as follows [24–28, 31]:

$$\phi_{model} = Kh + \phi_0 \tag{3.1}$$

Where K is the key coefficient to be estimated; h is the elevation, which can be derived from an auxiliary DEM; and ϕ_0 is a phase offset.

As the phase quality of any interferogram is not homogeneous due to the different decorrelation sources, K has to be estimated from a set of high quality pixels, this is PSs. As resolution is not a constrain, the quality of the interferograms can be improved with multi-looking and the PSs selected imposing a simple coherence threshold. Since the coefficient K is assumed to be constant in a specific interferogram, it is possible to obtain a good estimation of K by adjusting the linear model, ϕ_{model} Eq. (3.1), to the observation phase, ϕ_{obs}. The coefficient K can be estimated by minimizing a MAF [76] defined as follows:

$$\Gamma = \frac{1}{N}\sum_{i=1}^{N}\left|e^{-j\phi^i_{obs}} - e^{-j\phi^i_{model}}\right|^2 \tag{3.2}$$

Where N is the number of selected PSs. The main advantage of working in the complex space is that it can be done with wrapped interferograms, so no phase-unwrapping is necessary and a potential source of errors is avoided.

Other papers dealing with the estimation of coefficient K have been published in the last years [26, 28]. In [26], a preliminary deformation is estimated and removed prior the calculation of K to avoid the "noise" contribution of deformation. Alternatively, in [28], improvements have been made by analysing the observed phase with a multiple spatial scales approach. Using these methodologies, topography related APS can be estimated correctly with the assumption that there is no turbulent APS in the phase ϕ_{obs}. Unfortunately, if the interferogram contains turbulent artifacts the estimation of K will be jeopardized.

In order to make more robust the model adjustment in presence of turbulent APS, in this Chapter it is proposed to use phase differences among the selected PSs instead of the absolute values. This improved method has been called Linear Model Resisting Turbulent Atmosphere Delay (LMRTA). Under LMRTA approach, it is possible to reduce the impact of turbulent APS significantly.

The implementation of the LMRTA is presented below. Considering the situation with turbulent APS, the observation phase ϕ_{obs} consists of ϕ_{atm_stra} and ϕ_{atm_turb} components.

$$\phi_{obs} = \phi_{atm\_stra} + \phi_{atm\_turb} \tag{3.3}$$

As ϕ_{atm_stra} component correlates with topography, but ϕ_{atm_turb} component not, adjusting directly the model ϕ_{model} with the observation phase ϕ_{obs} may lead to an incorrect

coefficient K. Taking advantage of the spatial correlation of ϕ_{atm_turb}, the differential phases among neighbouring pixels can be used instead. A new observation phase between two pixels i and j, $\Delta\phi^{i,j}_{obs}$, can be defined to reduce the impact of turbulent APS in the model adjustment. The new phase is defined as,

$$\begin{aligned}\Delta\phi^{i,j}_{obs} &= \Delta\phi^{i,j}_{atm\_stra} + \Delta\phi^{i,j}_{atm\_turb} \\ &= \phi^{i}_{atm\_stra} - \phi^{j}_{atm\_stra} + \phi^{i}_{atm\_turb} - \phi^{j}_{atm\_turb}\end{aligned} \tag{3.4}$$

Correspondingly, LMRTA model can be defined now as

$$\begin{aligned}\Delta\phi^{i,j}_{model} &= Kh^i - Kh^j + \phi^i_0 - \phi^j_0 \\ &= K(h^i - h^j)\end{aligned} \tag{3.5}$$

ϕ_0 is a constant value for all pixels of the interferogram. Under the practical point of view, the selected pixels can be related thanks to a Delaunay triangulation, where the pixel locations constitute the nodes and the relations among them the arcs. These arcs define the phase differences to be used during the model adjustment step. Different limitations can be set to improve the performance of K estimation, for instance the maximum arc length or the minimum number of arcs reaching any pixel of the triangulation.

Many studies indicate that the turbulent atmospheric artifacts correlate spatially [16]. The level of correlation decreases as the pixels' distance increases. Therefore, when estimating the coefficient of stratified APS, the influence of $\Delta\phi^{i,j}_{atm\_turb}$ component can be partially weakened by weighting in the MAF the different pixel pairs. The farther the pixels the lower its weight in MAF. To be more specific, for two close pixels i and j located at short distance the turbulent term for each one is very similar, so $\Delta\phi^{i,j}_{atm\_turb}$ should be close to zero. On the contrary, for other pixels with a large separation, the turbulent APS may be totally uncorrelated and the impact of $\Delta\phi^{i,j}_{atm\_turb}$ in MAF is considerable. Based on this concept, an appropriate covariance matrix involving the correlation length would be beneficial for weighting the different pixels' pairs.

3.1.2 Spatial covariance matrix

Previous studies show that a stochastic model can be used to properly characterise turbulent atmosphere phase delay [23]. Turbulent atmosphere artifacts are characterised by its high spatial correlation. In spatial statistics the theoretical variogram is a function that describes the degree of spatial dependence of a spatial random field. So it is actually the variogram of atmospheric artifacts that can characterise the correlation of turbulent APS.

In geostatistics the empirical variogram is an estimate of the theoretical variogram and measures the spatial variability of an isotropic and stationary area. The empirical variogram $\hat{\gamma}(h)$ is defined as [95]:

$$\hat{\gamma}(l) = \frac{1}{2|N_l|}\sum_{(i,j)\in N_l}|z_i - z_j|^2 \tag{3.6}$$

Where N_l is the set of pairs of pixel i, j within distance l, $|N_l|$ is the total number of pairs within distance l and z would be in this case the turbulent atmospheric phase value.

In practice, the turbulent phase is mixed with other components that are expected to be less correlated in space. Hence, the variogram of the turbulent atmospheric artifacts can be empirically estimated from the interferograms.

The turbulent atmospheric covariance matrix Σ of one interferogram can be derived from the empirical variogram.

$$\Sigma = \begin{pmatrix} \sigma^2_{11,11} & \sigma^2_{11,12} & \cdots & \sigma^2_{11,1m} & \sigma^2_{11,21} & \sigma^2_{11,22} & \cdots & \sigma^2_{11,nm} \\ \sigma^2_{21,11} & \sigma^2_{21,12} & \cdots & \sigma^2_{21,1m} & \sigma^2_{21,21} & \sigma^2_{21,22} & \cdots & \sigma^2_{21,nm} \\ \vdots & \vdots & \ddots & \vdots & \vdots & \vdots & \ddots & \vdots \\ \sigma^2_{n1,11} & \sigma^2_{n1,12} & \cdots & \sigma^2_{n1,1m} & \sigma^2_{n1,21} & \sigma^2_{n1,22} & \cdots & \sigma^2_{n1,nm} \\ \sigma^2_{12,11} & \sigma^2_{12,12} & \cdots & \sigma^2_{12,1m} & \sigma^2_{12,21} & \sigma^2_{12,22} & \cdots & \sigma^2_{12,nm} \\ \sigma^2_{22,11} & \sigma^2_{22,12} & \cdots & \sigma^2_{22,1m} & \sigma^2_{22,21} & \sigma^2_{22,22} & \cdots & \sigma^2_{22,nm} \\ \vdots & \vdots & \ddots & \vdots & \vdots & \vdots & \ddots & \vdots \\ \sigma^2_{nm,11} & \sigma^2_{nm,12} & \cdots & \sigma^2_{nm,1m} & \sigma^2_{nm,21} & \sigma^2_{nm,22} & \cdots & \sigma^2_{nm,nm} \end{pmatrix} \tag{3.7}$$

where n, m are the maximum pixel indices in azimuth and range directions respectively. Each element $\sigma^2_{hi,jk}$ in the covariance matrix can be derived as follows:

$$\sigma^2_{hi,jk} = \sigma^2(0) - \hat{\gamma}_{hi,jk}(l) \tag{3.8}$$

Where $\sigma^2(0)$ is the covariance at distance $l = 0$. In practice, $\sigma^2(0)$ is the limit of the variogram tending to infinity lag distances, and $h, j \in \{1, 2, \ldots, n\}, i, k \in \{1, 2, \ldots, m\}$. $\hat{\gamma}_{hi,jk}(l)$ is calculated from Eq. (3.6).

Once the covariance matrix of turbulent APS has been estimated, it can be used to weight the different arcs of the triangulation when adjusting the LMRTA model.

In real situations, three aspects limit the variogram-based estimation accuracy of the turbulent APS covariance matrix: the density and quality of PSs, the real shape of the variogram, and the last but not the least, the different phase components present in the interferograms that can disguise the turbulent APS [90].

3.2 Simulated study

The LMRTA method proposed in this Chapter is being validated firstly with simulated data in order to perform tests under perfectly controlled conditions. In comparison with real data cases, the true values of the different parameters involved are known, which can be compared with the estimated ones. In the simulated test, firstly, both topography related APS and turbulent APS are simulated. Secondly, the method aforementioned has been implemented to separate stratified APS from turbulent APS. Finally, an accuracy study has been done to evaluate the results of the new method compared with those of the conventional one.

3.2.1 Simulation of the different phase components

The following synthetic scenario is simulated based on the parameters presented in Table 3.1. Details on how to simulate the different atmospheric components are discussed.

Table 3.1: Parameters over a synthetic scenario

Parameters	Value
Size of Images (pixels)	256 x 256
Number of Images	51
Number of Interferograms	135
Minimum temporal baseline (days)	11
Size of pixels (m)	30
Number of pixels	726
Number of links	2132
Maximum coefficient	0.2
Minimum coefficient	0.16
Standard deviation of coefficient	0.01
Maximum topography (m)	2000
Minimum topography (m)	1600

On the one hand, in terms of the turbulent atmospheric artifacts from Section 3.1.2, it is clear that the spatial variance is the key point. A large number of methods have been exploited to simulate Gaussian random fields [96, 97]. In these approaches, the spatial correlation matrix has to be firstly defined, and then the Cholesky decomposition can be applied to a random process [23] or the circular embedding method [96] can be used to Gaussian stochastic simulations. As mentioned in Section 1.1, Kolmogorov's theory can generally describe the turbulent atmospheric artifacts and the spatial correlation follows approximatively an exponential law. In addition, a wide range of correlation models can describe the Kolmogorov's turbulence, which include Matérn-family models, Bessel family models, Gaussian, exponential and spherical models. Different models are compared in [21]. In the following, the covariance of turbulent atmospheric artifacts has been simulated through a spherical model.

$$\gamma(l) = \begin{cases} \sigma^2(0)[\frac{3l}{2a} - \frac{1}{2}(\frac{l}{a})^3], & l \leq a \\ \sigma^2(0), & l > a \end{cases} \tag{3.9}$$

Where $\sigma^2(0)$ means the variogram value for distances far away from the correlation distance, l is the distance and a indicates the correlation window. Examples of simulated turbulent atmospheric artifacts are shown in Fig. 3.1(a) and Fig. 3.1(c).

On the other hand, the topography related atmospheric artifacts are modelled using a simple linear model. For simplicity, a topography based on a paraboloid and a semi-empirical coefficient K are chosen in the simulated scene. Examples of simulated topography related atmospheric artifacts are shown in Fig. 3.1(b) and Fig. 3.1(d). We refer them as pair I1 and I2.

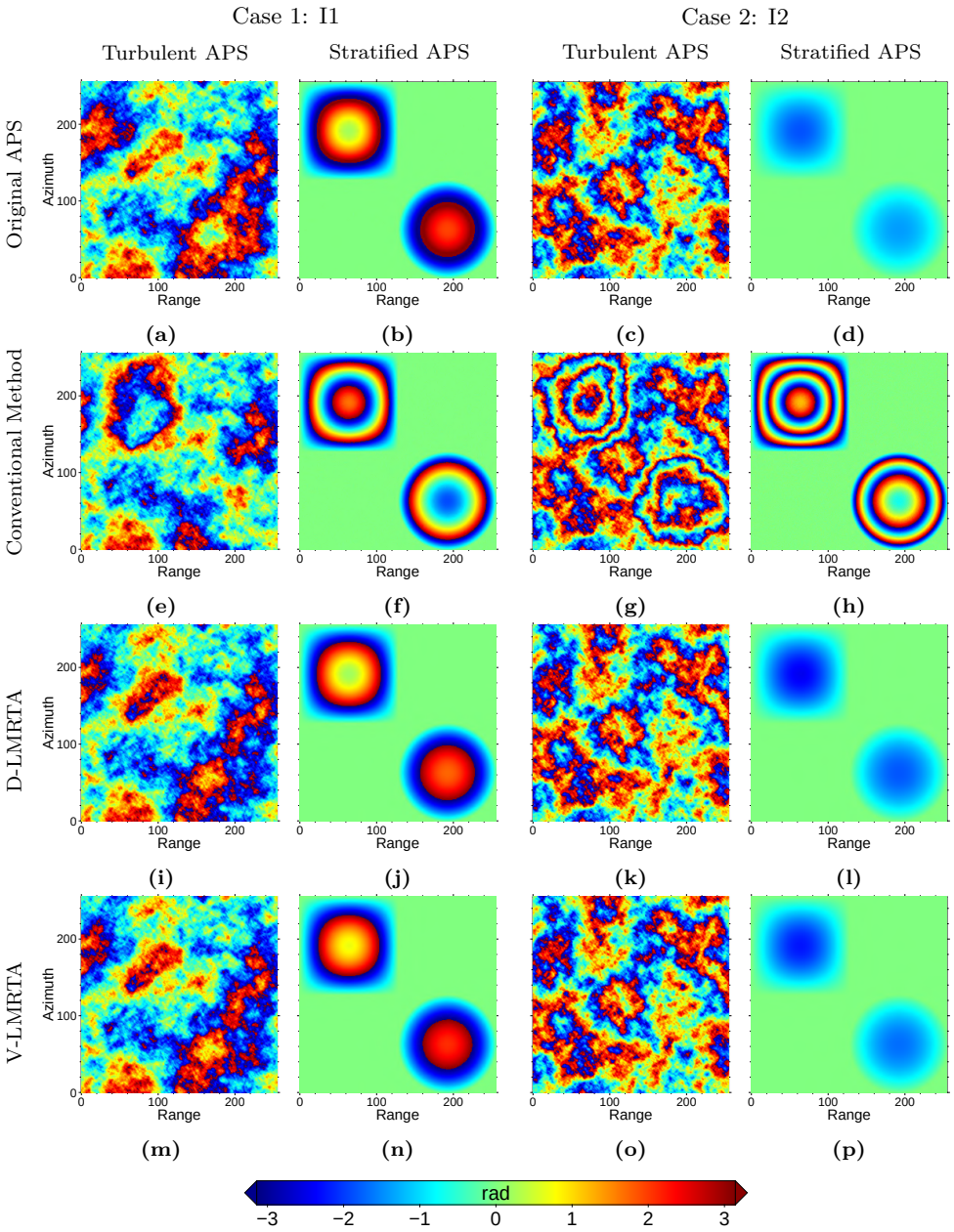

Fig. 3.1. Two examples of true and estimated turbulent APS (first and third column) and topography related APS (second and fourth column). The first two columns are for I1 and last two columns are for I2. The first row subfigures are for original APS, second row for conventional method, third row for distance weighted D-LMRTA and last row for variogram weighted V-LMRTA.

3.2.2 Stratified atmospheric artifacts estimation

The first step of the algorithm is to select pixels with good phase quality, this is the PSs. The classical PSs coherence-based selection over the multi-looked interferograms can be used. The number of PSs selected will depend on the coherence threshold and the particularities of the interferogram. Once selected, they are connected using a Delaunay triangulation, as explained in Section 3.1.1. In the simulation, 726 pixels have been randomly selected. The selected pixels and triangulation are shown in Fig. 3.2.

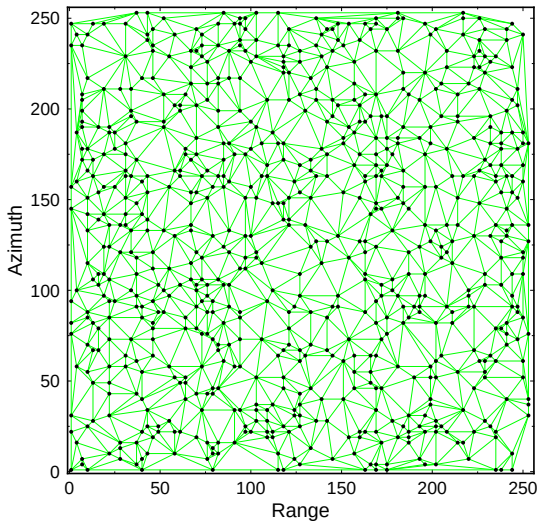

Fig. 3.2. Delaunay triangulation for selected PSs in the simulator.

As mentioned previously, experimental variograms of APS are important to provide the parameters that characterise the spatial properties of turbulent atmospheric artifacts. In the simulated case, Eq. (3.6) has been used to do the variogram analysis. In the network of selected pixels, the minimal and maximal distances are 30 m and 10380 m respectively. Distance bins have been set to 30 m wide, the same resolution of the interferogram, in the variogram computation. The variograms calculated from the simulated turbulent APS I1 and I2 are shown in Fig. 3.3. Variogram values for arcs larger than 8 km are not represented as the number of pixels was too few for providing a reliable estimation. As it can be seen, the variogram values for distances over 3 km show an oscillation behavior around a specific value, $\sigma^2(0)$. In other words, both plots in Fig. 3.3 show that the correlation distance of the atmospheric artifacts is about 3 km. The values of $\sigma^2(0)$ for I1 and I2 are 3.4 mm^2 and 5.8 mm^2 respectively, which is the average of variogram values for distance over 3 km for each case. Finally, the covariance matrix Σ for each interferogram can be filled using Eq. (3.8).

In the following, both conventional and LMRTA methods are applied to the synthetic data to separate the stratified and the turbulent APSs. The optimal coefficient K_{opt} can be estimated by a brute-force method testing all reasonable values of K_{opt} in $[-1, 1]$ with

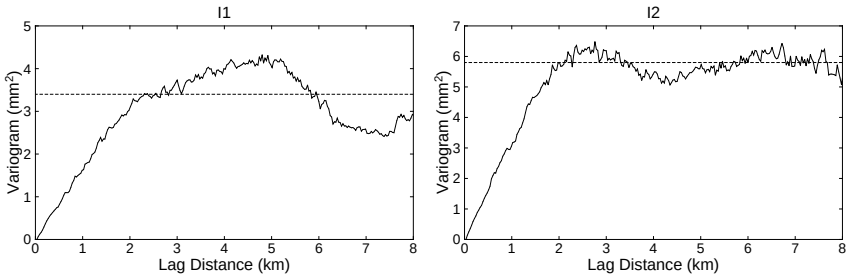

(a) **(b)**

Fig. 3.3. Experimental variograms (dots) for turbulent APS I1 and I2. Dashed lines indicate $\sigma^2(0)$ for both cases.

a step of 0.0001 in function $\Gamma(K)$.

$$K_{opt} = arg \min_{K\in[-1,1]} \Gamma(K) \tag{3.10}$$

The LMRTA algorithm uses the phase differences among connected pixels as a new observation phase to mitigate the impact of turbulent APS. In order to further reduce its impact, each arc can be weighted in such a way that the contribution of short distance pairs (less affected by turbulent APS) is increased in front of longer ones (more affected by turbulent APS). Based on this idea, the LMRTA algorithm can be improved by considering a weight matrix. Consequently, the MAF can be rewritten as follows.

$$\Gamma(K) = \frac{1}{\sum_{l=1}^{L} w_{i,j}} \sum_{i=1}^{L} \left| w_{i,j}(e^{-j\Delta\phi_{obs}^{i,j}} - e^{-j\Delta\phi_{model}^{i,j}}) \right|^2 \}) \tag{3.11}$$

Where L is the number of total arcs established among pixels and $w_{i,j}$ is its weight. $\Delta\phi_{obs}^{i,j}$ and $\Delta\phi_{model}^{i,j}$ are detailed in Eq. (3.4) and Eq. (3.5) respectively. The best weighting strategy would be to use the covariance matrix Σ derived from the empirical variogram, as presented Section 3.1.2. However, with real data covariance matrix can be costly to build in large scenes and prone to errors depending on the interferograms' quality. Alternatively, links' distances can be used as a practical alternative for determining the weight for each link. Namely, pairs with short distances are assigned higher weights than pairs with longer distances.

3.2.3 Evaluation of results and sensitivity analysis

Fig. 3.1(a)–(d) show the original APS for two different cases with both turbulent and stratified atmosphere. Fig. 3.1(e)–(h) show the estimated turbulent APS and topography related APS obtained using the conventional method. Visually comparing with the true APS, the errors in the estimation of the stratified APS, which are translated to the estimation of the turbulent APS, are clearly visible. The benefits of the two versions of LMRTA, the Distance Weighted LMRTA (D-LMRTA) and the Variogram Weighted

LMRTA (V-LMRTA), are evident from a visual comparison of the results with the original APS. Fig. 3.1(i)–(l) show the results for D-LMRTA while Fig. 3.1(m)–(p) for V-LMRTA.

Table 3.2 shows a comparison of the true and estimated values of K for the different methods. As it can be seen, the estimated coefficients for D-LMRTA and V-LMRTA are closer to the true values than the conventional method demonstrating the robustness of the proposed strategy when turbulent APS is presented. The performance of D-LMRTA and V-LMRTA is very similar, thus the distance-based weighting is an efficient alternative to avoid the calculation of the covariance matrix of turbulent APS from the empirical variogram.

Table 3.2: True and estimated coefficients. K is the true value, while K_1, K_2, K_3 are the estimated results using conventional method, D-LMRTA and V-LMRTA.

Interferograms	True K	Conventional K_1	D-LMRTA K_2	V-LMRTA K_3
I1	0.0100	0.0273	0.0151	0.0140
I2	0.0046	0.0442	0.0061	0.0056

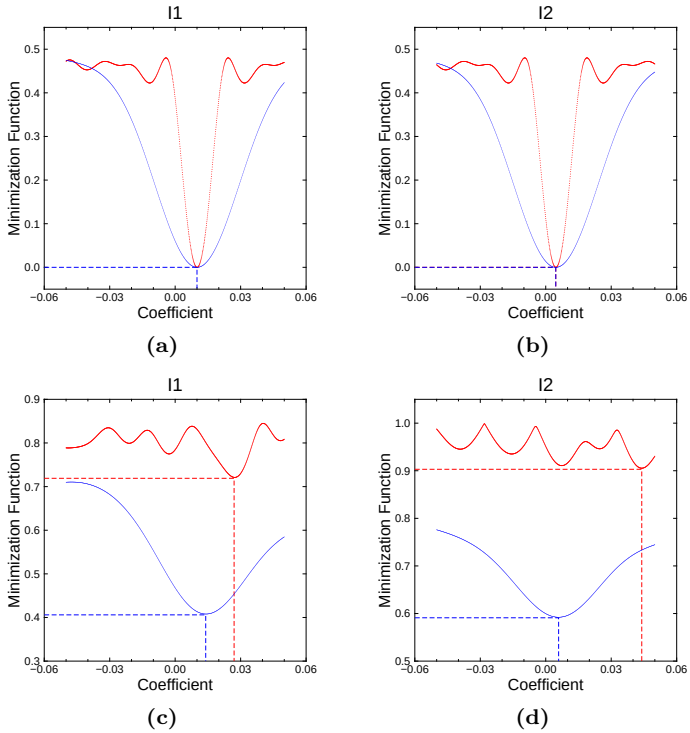

Fig. 3.4. Minimization Function. Red lines refer to conventional method and blue lines refer to D-LMRTA.

It is also interesting to study the sensitivity of the minimization step to demonstrate the robustness of LMRTA approach. Fig. 3.4(a) and Fig. 3.4(b) show the behaviour

of MAF, $\Gamma(K)$, for the conventional and D-LMRTA methods when interferograms have stratified atmosphere only. The absence of the turbulent component allows both methods to find the exact value but the conventional method is more sensitive. The quadratic behaviour of the function near the minimum is narrower than with D-LMRTA. The differences arise when turbulent APS and a linear deformation pattern are added to the interferograms. Fig. 3.5 shows the deformation pattern added to the interferograms, which covers the center of the scene. The results shown in Fig. 3.4(c) and Fig. 3.4(d) validate the robustness of D-LMRTA. D-LMRTA is able to retrieve a good approximation of the correct K while the conventional method fails. Looking at the plots, also the conventional method presents many local minima. This will make the minimization results very sensitive to any additional source of noise presenting in the interferometric phase. The linear deformation phase contribution definitely contaminates the estimation of K with the conventional method. However, the same advantages of D-LMRTA (or V-LMRTA) in front of turbulent APS, thanks to its phase difference approach, also apply to the low-pass behaviour of the linear deformation.

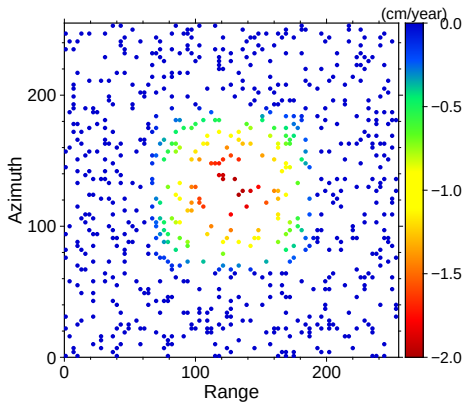

Fig. 3.5. Linear deformation pattern in simulated interferograms.

Besides explicit discussion on the above two interferograms I1 and I2, statistical analyses are carried out to evaluate the performance of LMRTA on other simulated pairs. Three methods are compared, conventional, unweighted LMRTA and covariance weighted V-LMRTA. Phase Standard Deviation (SD) is used as a metric to assess their performance. Detailed SD analyses are shown in Table 3.3 for four different pairs. Interferograms' phase components contain linear deformation, turbulent and stratified APS. *Reference phase* components include all of them except the stratified one. *Corrected phase* means residue after removing the estimated stratified component. The magnitude of the simulated turbulent APS is determined with the parameter $\sigma(0)$. The larger $\sigma(0)$ the stronger the turbulent component. As it can be seen in Table 3.3, for a mild turbulent component (Ifg1, $\sigma(0) = 0.710$), all three methods provide a good estimation of stratified APS. More specifically, SD vaules of the corrected phases are close to the reference one, SD (0.514), and the relative errors are very small. Even though the differences are not significant, the smaller error is for V-LMRTA. When the turbulent component increases the performance of the conventional method starts to degrade. Ifg2, Ifg3 and Ifg4 show different cases with raising turbulent component. As expected, the relative errors for the

conventional method raise as well. At the same time both LMRTA methods keep the relative errors small. The worst value for unweighted LMRTA is 2.73% and for V-LMRTA is 1.04%, but they do not occur with the interferogram with strongest turbulent APS. Once again, the best performance is provided by V-LMRTA.

Table 3.3: Performance of different correction methods for four selected interferograms. Values in parentheses are relative error ($|Corrected - Reference|/Reference$).

Ifg.	$\sigma(0)$	Ifg phase SD	Reference phase SD	Corrected phase SD		
		All phase components	No stratified component	Conventional method	Unweighted LMRTA	V-LMRTA
Ifg1	0.710	2.071	0.514	0.508 (1.17%)	0.509 (0.97%)	0.510 (0.78%)
Ifg2	1.574	1.834	1.546	1.761 (13.91%)	1.525 (1.36%)	1.530 (1.04%)
Ifg3	2.586	2.574	2.416	3.426 (41.81%)	2.482 (2.73%)	2.419 (0.12%)
Ifg4	3.310	3.235	2.547	3.491 (37.06%)	2.534 (0.51%)	2.535 (0.47%)

Finally, a statistical comparison is applied to a set of 135 simulated interferograms with $\sigma(0)$ ranging from 0.71 to 3.53. The results are shown in Table 3.4. For the correction with conventional method only 39% pairs have a relative error below 1.5% while this rate increases dramatically to around 70% for both LMRTA. The number of pairs with relative error above 5.0% decreases from the 44.4% obtained with the conventional method to only 3.7% for both LMRTA. Meanwhile, the two LMRTA methods show a similar statistical performance. Moreover, a scatter plot for the 135 simulated interferograms relating $\sigma(0)$ and absolute SD error is shown in Fig. 3.6. It is clear that all the three methods present similar performances in interferograms with mild turbulent components. The better performance of LMRTA is evident in pairs with strong turbulent contamination.

Table 3.4: Statistical comparison of different correction methods for all simulated interferograms in terms of relative error.

Correction performance	Numbers (Percentage)		
Relative error	Conventional method	Unweighted LMRTA	V-LMRTA
0-1.5%	53 (39.3%)	95 (70.4%)	94 (69.6%)
1.5%-3.5%	10 (7.4%)	24 (17.8%)	26 (19.3%)
3.5%-5.0%	12 (8.9%)	11 (8.1%)	10 (7.4%)
Above 5.0%	60 (44.4%)	5 (3.7%)	5 (3.7%)

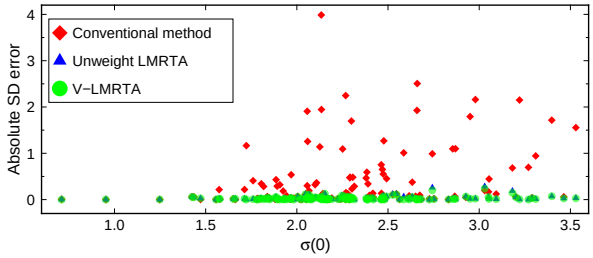

Fig. 3.6. The scatter plot between $\sigma(0)$ and absolute SD error for 135 interferograms with conventional, unweighted LMRTA and V-LMRTA methods.

3.3 Validation with real SAR data

3.3.1 Test site and data set

To demonstrate the performance of LMRTA on real data, Tenerife island (Spain, see Fig. 3.7) has been selected as test site. Tenerife is a volcanic island, whose eruptive system is dominated by the Las Canadas Caldera and the extinct Teide volcano. In 2004, a seismic crisis occurred in Tenerife, which produced surface gravity changes and displacements [98–100]. It is worth to point out that in this test site, the topography ranges from sea-level up to 3700 m. In such mountainous regions, the atmospheric artifacts can be deeply correlated with the topography. In addition, over coastal areas, atmospheric turbulences are usually strong [27], which can interfere the estimation of stratified APS with conventional methods. Consequently, this region is a perfect scenario to evaluate the correction capabilities of LMRTA. The dataset is composed by 55 Sentinel-1A satellite images acquired in the period covering from 2014 to 2016. From the available images 99 differential interferograms, with perpendicular and temporal baselines shorter than 400m and 70 days respectively, have been produced. All processing has been carried out with SUBSIDENCE-GUI, the software implementation of CPT [20] developed at UPC.

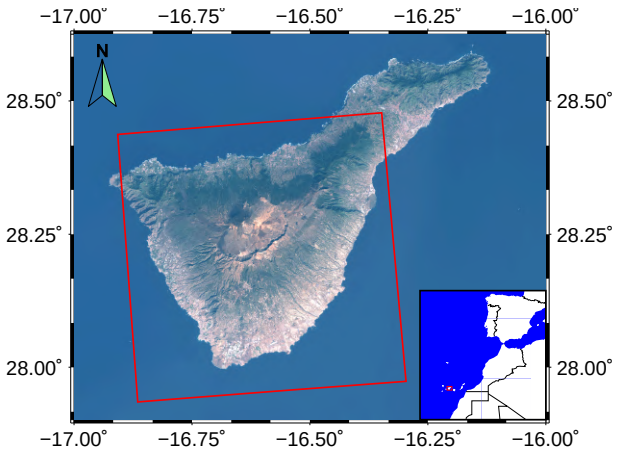

Fig. 3.7. Location of Canary Archipelago just off the southern coast of Morocco and map of Tenerife Island. The red rectangle indicates the area of interest, centred on Teide.

By analysing the relationship between unwrapped phase and topography, it has been found that 14 out of the 99 interferograms present strong phase artifacts linearly correlated with topography. Fig. 3.8 shows 6 interferograms with different temporal and spatial baselines. The labels indicate the acquisition dates of the master and slave images with the format year-month-day (yyyymmdd). In order to exclude that the fringes were produced by inaccuracies of the DEM used to remove topography, Fig. 3.9(a) shows a differential interferogram with a moderate baseline with almost no fringes on the slopes of Teide. Moreover, Fig. 3.9(b) shows a scatter plot of the spatial baseline and the number of fringes of the interferograms. Clearly, the number of fringes is not correlated with the spatial baseline. The performance of the proposed algorithm is assessed based on the aforementioned 14 pairs.

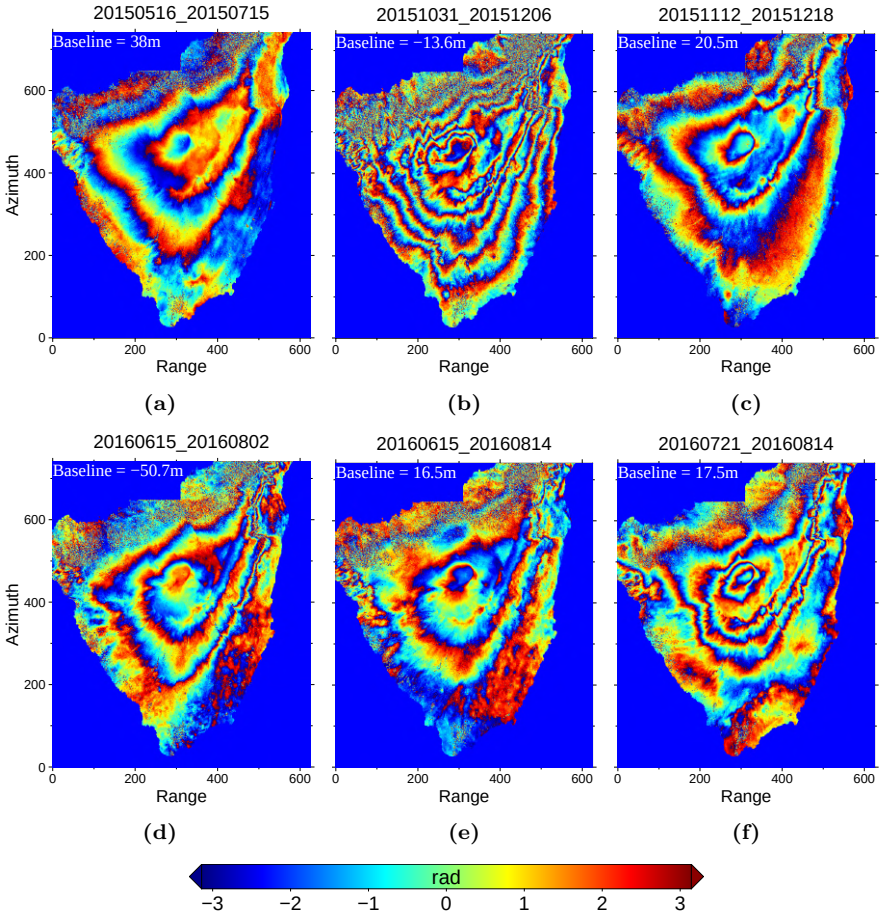

Fig. 3.8. Wrapped differential interferograms with strong topography-related APS.

3.3.2 Processing chain

The block diagram that summarizes LMRTA algorithm processing chain is shown in Fig. 3.10. As it can be observed, there are three main steps. Firstly, a preliminary linear model, which includes linear deformation and DEM error, is adjusted to the stack of multi-looked differential interferograms to cancel, as much as possible, the influence of these two phase components. Secondly, a weighted LMRTA model is adjusted to the residue phase to model stratified APS. Weighting can be obtained either from the covariance matrix or the pixels' distances. For the former, phase unwrapping is necessary in order to estimate the covariance matrix from the experimental variogram. In this thesis interferograms have been unwrapped using SNAPHU [101]. For the latter, unwrapping can be skipped. Once the topography correlated APS have been estimated with LMRTA, it can be removed from the interferograms. CPT is then applied to the compensated interferograms, which can be now at full-resolution, to determine the remaining velocity of deformation and DEM error. In practice, the first low-resolution linear model adjustment is affected by

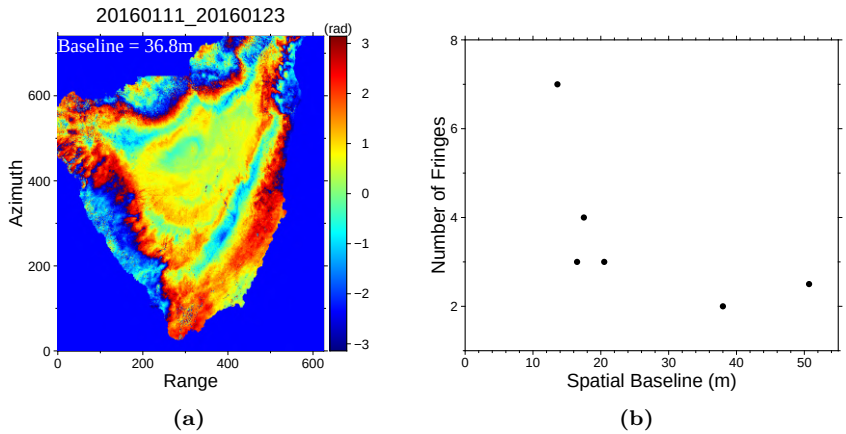

Fig. 3.9. (a) is the 20160111-20160123 differential interferogram. (b) is the relationship between the number of fringes and spatial baseline.

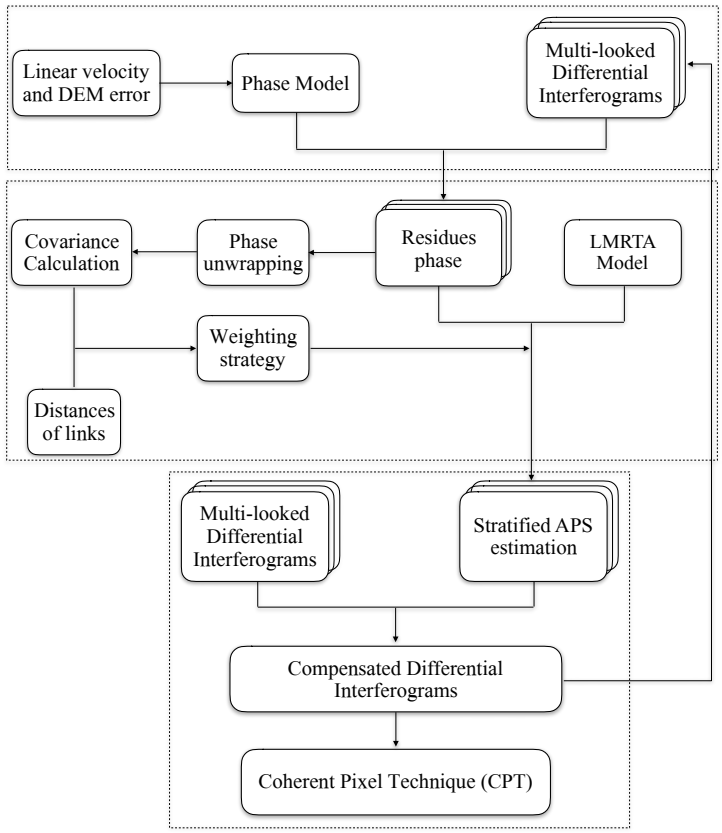

Fig. 3.10. LMRTA diagram for atmospheric artifacts compensation.

APS and the processing can be benefited by an iterative procedure, as shown in Fig. 3.10. The iteration over the residues does not need to recalculate the covariance matrix as the experimental variogram would not be reliable if residual phases were used. The iterative procedure helps to better estimate the stratified APS and the linear terms.

3.3.3 Stratified atmospheric artifacts compensation

The performance of LMRTA is evaluated using Sentinel-1A data. Among all differential interferograms, the pair (20151031-20151206) has been selected to visualize the behavior of LMRTA. Firstly, pixels with coherence values higher than 0.7 from the multilooked, 5x25 (Azimuth x Range), interferograms are selected as PSs. The 15305 pixels selected are linked using a Delaunay triangulation to generate the observation vector $\Delta\phi_{obs}^{i,j}$. Then, Eq. (3.6) is applied to calculate the empirical variogram, and after that the covariance matrix using Eq. (3.8). Finally, conventional, unweighted LMRTA and V-LMRTA methods are used to retrieve the model coefficients that better fit the observation vector $\Delta\phi_{obs}^{i,j}$.

Fig. 3.11 presents the results using the different methods over the selected pair. In detail, Fig. 3.11(a) is the original wrapped differential interferogram, where fringes are strongly correlated with the topography. After the stratified APS compensation, wrapped residual phases for conventional linear model, unweighted LMRTA and V-LMRTA are shown in Fig. 3.11(b), Fig. 3.11(c) and Fig. 3.11(d) respectively. It is clear from the residual fringes that the three methods are able to reduce the number of fringes to some extent. To be specific, one evident fringe still exists in the residue after conventional correction, while there are no apparent topographic related fringes in the residues from both LMRTA, which produces visually almost identical results. The SD analysis on the unwrapped residue phases in Section 3.3.4 shows that V-LMRTA performs better than unweightedt LMRTA. Unwrapped phases for differential interferograms and phase residues have been obtained with SNAPHU [101]. Subfigures in the second row of Fig. 3.11 show scatter plots of unwrapped phases and elevation of the selected PSs. It is clear from Fig. 3.11(f) that the unwrapped phase of the original differential interferogram shows a clear linear topographic trend. Conventional model and both LMRTA are able to correct this trend. An inspection of the phase residues shows the better performance of LMRTA compared with the conventional method, which still presents a residual linear trend as seen in Fig. 3.11(g). The third row in Fig. 3.11 shows the unwrapped phases of PSs over the radar brightness image. Once again, it is clear that LMRTA outperforms the conventional method.

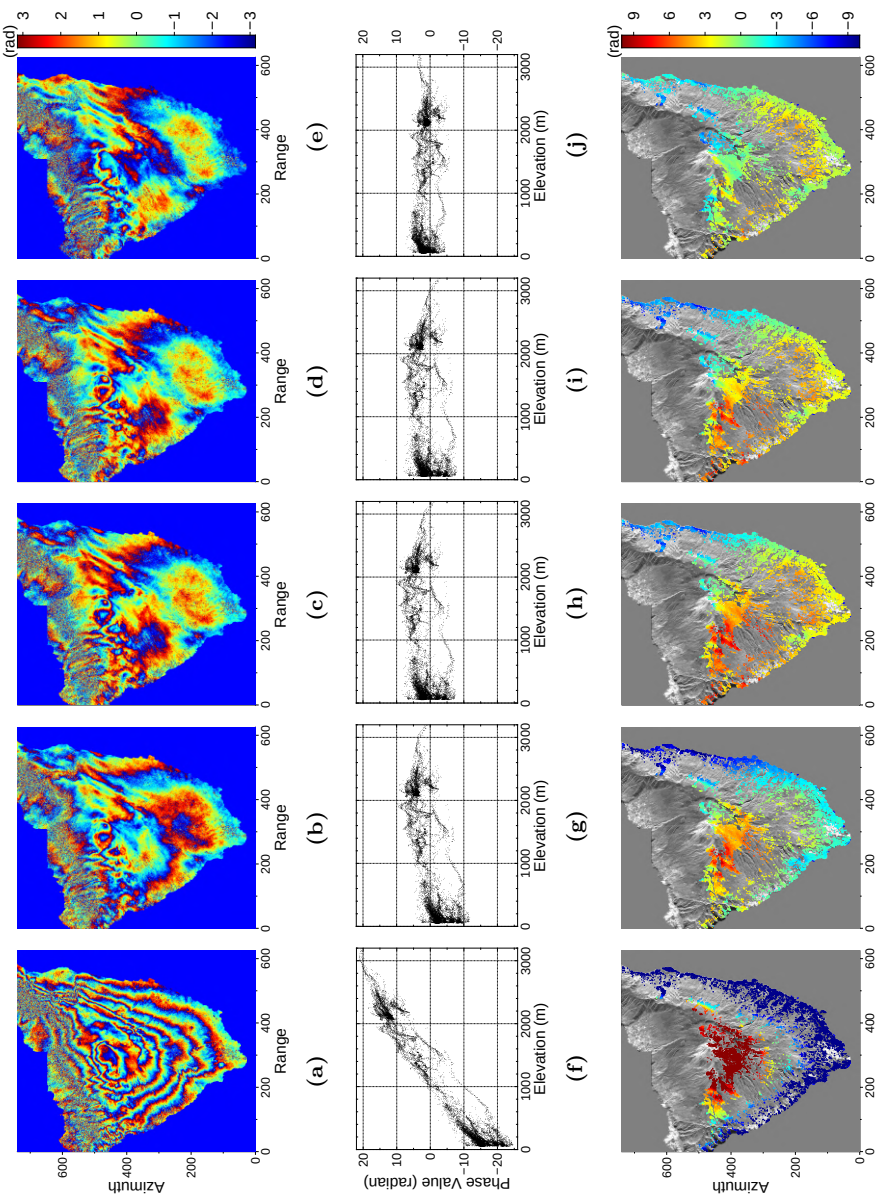

Fig. 3.11. 20151031-20151206 case study of APS compensation over Tenerife island, Spain. Columns from left to right show original phase, residue phase for conventional linear model, unweighted LMRTA, covariance weight V-LMRTA and ERA5 method respectively. Rows from top to bottom represent wrapped phase, phase-elevation scatters and unwrapped phase residue.

The model adjustment could be benefited of an iterative procedure, as shown in Fig. 3.10, that would allow a refinement of the stratified APS estimation. The iterative procedure has been evaluated with the three methods using, as example, two different interferograms. The performance after each iteration is evaluated with the SD of the phase residue. Fig. 3.12(a) shows the 20151031-20151206 case, in which the three methods almost converge after the first regression. After the second iteration there is no significant improvement in the solution. As expected, V-LMRTA provides the solution with the lowest SD. Conversely, Fig. 3.12(b) shows a situation in which the conventional method diverges but unweighted LMRTA and V-LMRTA present identical performance as with the previous case. It can be concluded that the iterative procedure can refine the solution with just a single iteration and, in most of the cases, the marginal benefit obtained does not compensate its computational cost.

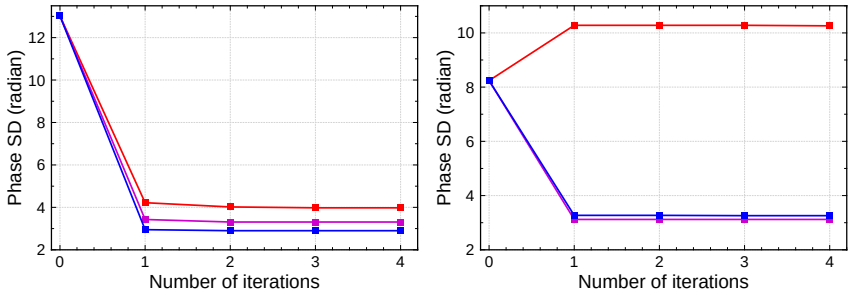

Fig. 3.12. SD of phase residues at each iteration. Red, magenta and blue represent conventional, unweighted LMRTA and V-LMRTA respectively. (a) 20151031-20151206 interferogram, (b) 20150715-20150808 interferogram.

3.3.4 Validation with global meteorological reanalysis data

The proposed method is validated by comparing the phase delays estimated with those obtained from GAM reanalysis data. ERA5 data has been selected for the validation as it is a relative new generation of climate reanalysis data with better performances than other datasets (e.g. ERA-interim, MERRA).

ERA5 is the fifth global ECMWF reanalysis product produced by Copernicus Climate Change Service, providing estimates of temperature, pressure, humidity and geopotential height along 37 pressure levels, with 31 km resolution. These reanalysis parameters are hourly available covering the period from 1979 to present [45].

Based on the vertical profiles of temperature, pressure, and relative humidity on coarse grid nodes provided by GAM, the refractivity index N can be calculated with an empirical equation [102] at different height levels. Once the refractivity index N is computed, the absolute phase delay can be obtained for each pixel of the interferogram by integration. The integration of N along the LOS requires the interpolation of N at the required locations and an external DEM to consider the local topography of each pixel. Details on the derivation of tropospheric delays from the atmospheric reanalysis products are described in [43, 46, 103]. In this Chapter, based on the idea of integrating atmospheric

parameters along zenith direction in Python-based Atmospheric Phase Screen (PyAPS) [43, 46], an improved method calculating APS along LOS direction [104] has been used to validate the algorithm. The improved method will be presented in Chapter 4 in detail.

Fig. 3.11(e), Fig. 3.11(j) and Fig. 3.11(o) show the wrapped phase residue, the scatter plots of unwrapped phase residue versus elevation and the PSs unwrapped phase residue over the radar brightness image after ERA5 APS compensation. Comparing ERA5 result Fig. 3.11(j) with both LMRTA results Fig. 3.11(h) and Fig. 3.11(i), it can be observed that they look very similar. Both LMRTA and ERA5 phase residues present a similar magnitude and fluctuations around zero, despite the latter has a lower SD. This can be explained by the fact that ERA5 can remove the turbulent APS to some extent. However, phase residue from the conventional method (Fig. 3.11(g)) shows a linear trend, which is not consistent with ERA5 result.

After applying a statistical analysis on PSs unwrapped phases obtained from each method, it has been observed that unweighted LMRTA and V-LMRTA can reduce SD from 13.02 to 3.425 and 2.95 rad respectively, while SD from the conventional method is 4.22 rad. With ERA5 method, SD is reduced to 3.141 rad, which is closer to the results provided by V-LMRTA. The statistical comparison further validates that V-LMRTA outperforms the conventional linear method.

3.3.5 Statistical analyses on all interferograms

Besides detailed analyses on the above specific interferogram, a statistical comparison of original differential phases and phase residues using the different methods for 14 interferograms with significant stratified APS has been carried out. In the comparison, the phase SD is used as a quality metric and ERA5 APS is used as reference. As it can be seen from the original interferogram column in Table 3.5, phase SD values are large due to the presence of strong atmospheric artifacts. After applying the different correction methods, SD of the phase residues are listed for each one.

Interferogram 20151112-20151218 (Ifg4) has been selected as example for a detailed analysis. Ifg4 was obtained from two images during the rainy season with a temporal baseline of 36 days and spatial baseline of 20.5 m. As it can be seen from Fig. 3.8(c), the wrapped phase exhibits a clear topography-related pattern that can be associated to stratified APS. After applying the conventional correction method, the SD of phase residue decreased a 51.0%, from 4.696 to 2.303 rad. Moreover, the residue can be reduced up to 1.649 and 1.678 rad using unweighted LMRTA and V-LMRTA respectively. Both LMRTA strategies produce similar results that are closer to the one provided by ERA5.

Table 3.5: Performance of different correction methods for 14 selected interferograms. Values in parentheses are correction percentage, $(original - corrected)/original$.

Interferograms	Spatial baseline	Phase SD				
		Original interfero-gram	Conventional method	Unweighted LMRTA	V-LMRTA	ERA5
20150516-20150715 (Ifg1)	38.0 m	3.951	1.915 (51.5%)	2.044 (48.3%)	2.104 (46.7%)	2.533 (35.9%)
20150715-20150808 (Ifg2)	-30.7 m	8.239	10.283(-)	3.121 (62.1%)	3.169 (61.5%)	4.006 (51.4%)
20151031-20151206 (Ifg3)	-13.6 m	13.020	4.220 (67.6%)	3.425 (73.7%)	2.950 (77.3%)	3.141 (75.9%)
20151112-20151218 (Ifg4)	20.5 m	4.696	2.303 (51.0%)	1.649 (64.9%)	1.678 (64.3%)	1.818 (61.3%)
20151206-20151230 (Ifg5)	-8.6 m	2.063	1.850 (10.3%)	1.761 (14.6%)	1.773 (14.1%)	1.798 (12.8%)
20151218-20160216 (Ifg6)	-21.5 m	6.965	5.985 (14.1%)	5.365 (23.0%)	5.149 (26.1%)	4.414 (36.6%)
20160111-20160123 (Ifg7)	36.8 m	1.848	1.626 (12.0%)	1.592 (13.6%)	1.555 (15.9%)	1.526 (17.4%)
20160603-20160615 (Ifg8)	33.3 m	3.447	3.358 (2.6%)	2.541 (26.3%)	2.553 (25.9%)	2.603 (24.5%)
20160615-20160709 (Ifg9)	19.9 m	3.268	3.169 (3.0%)	2.464 (24.6%)	2.503 (23.4%)	2.533 (22.5%)
20160615-20160721 (Ifg10)	15.5 m	3.277	3.017 (7.9%)	2.569 (21.6%)	2.705 (17.5%)	2.770 (15.5%)
20160615-20160802 (Ifg11)	-50.7 m	5.644	3.575 (36.7%)	3.407 (39.6%)	3.183 (43.6%)	2.969 (47.4%)
20160615-20160814 (Ifg12)	16.5 m	4.581	2.871 (37.3%)	2.142 (53.2%)	2.203 (51.9%)	2.303 (49.7%)
20160709-20160826 (Ifg13)	30.8 m	3.014	3.448 (-)	2.863 (5.0%)	2.606 (13.5%)	2.477 (17.8%)
20160721-20160814 (Ifg14)	17.5 m	6.170	6.017 (2.5%)	2.407 (61.0%)	2.371 (61.6%)	2.925 (52.6%)

Another two interesting pairs (Ifg2 and Ifg13) show that SD phase residues even increased after applying the conventional method, while the other methods can reduce the phase residue to similar levels. It is believed that the poor correction performance for the two pairs with the conventional method is caused by strong turbulent or local atmospheric artifacts. Fig. 3.13 can further prove it. Fig. 3.13(a) shows the original wrapped phase of Ifg2, from which it is clear that the turbulent atmospheric artifacts are significant in area A. Fig. 3.13(b) shows the selected PSs used for estimating the stratified APS for Ifg2. It can be seen that a large amount of pixels are selected in area A for the calculation. A similar pattern can also be found in Ifg13. Fig. 3.13(c) and Fig. 3.13(d) shows the original interferogram and selected PSs of Ifg13, respectively. For this pair, many pixels in area B, C and D, where the interferogram suffers turbulent atmospheric artifacts, are used for stratified APS estimation. Therefore, it can be concluded from the two case studies that the conventional method may fail for stratified APS estimation when turbulent atmospheric component is significant, while the proposed LMRTA method is more robust than the conventional method.

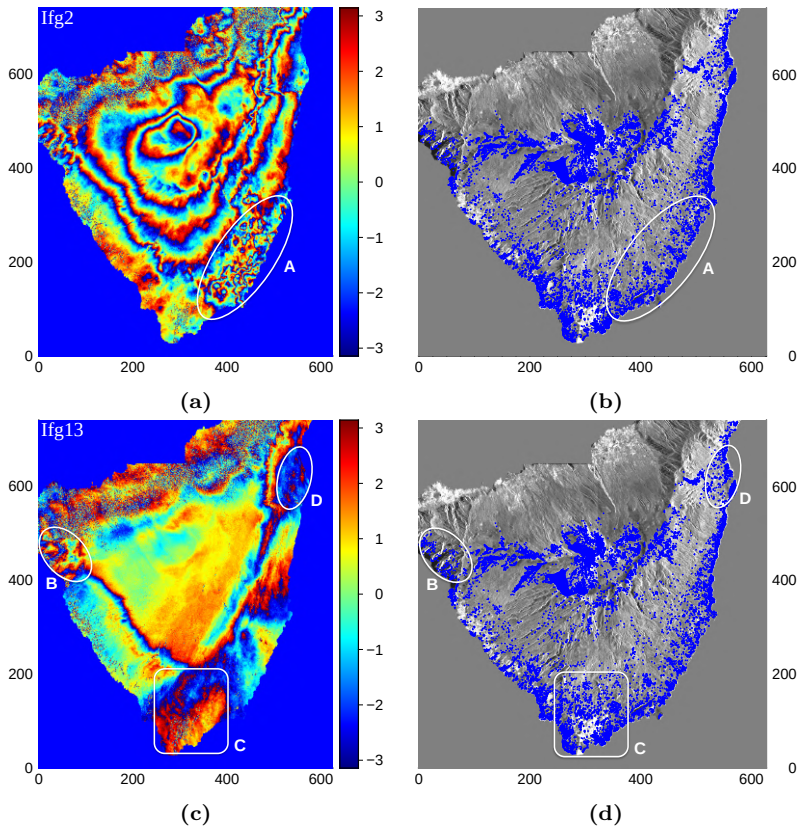

Fig. 3.13. Two case studies, 20150715-20150808 (Ifg2) and 20160709-20160826 (Ifg13). (a) The original wrapped phase of Ifg2. (b) The selected PSs for APS estimation for Ifg2. (c) The original wrapped phase of Ifg13. (d) The selected PSs for APS estimation for Ifg13.

For all pairs in Table 3.5 except Ifg1, LMRTA based methods show more SD reduction

than the conventional one. For Ifg1 case, the conventional method exhibits a correction of 51.5% compared with a 48.3% for the unweighted LMRTA and 46.7% for V-LMRTA, while ERA5 based correction shows the worst performance, 35.9%. The comparison between unweighted LMRTA and V-LMRTA shows that both produce comparable results in SD reduction and, depending on the case, one may achieve a better reduction than the other. The same idea can be applied to the ERA5 based compensation.

In all cases, both LMRTA strategies and ERA5 were able to reduce the APS but they are not able to cancel it completely. For the former, the turbulent APS is not considered in the linear model and thus it can not be compensated. For the latter, the coarse 30 km grid of the atmospheric parameters makes that strong local atmospheric artifacts would not be correctly modelled.

3.4 Summary

In this Chapter, a covariance weighted linear model for removing atmospheric artifacts in mountainous areas has been presented. The proposed approach, LMRTA, includes an improved linear model between stratified APS and topography based on phase differences among selected pixels, PSs, that reduces the impact of turbulent atmosphere. All selected pixels are related using a Delaunay triangulation. The model adjustment step also considers a weighting strategy that minimizes the effect of those arcs between pixels affected by turbulent atmosphere. The weights can be obtained either from the spatial covariance matrix derived from the empirical variogram or simply penalizing the longer links that are prone to be affected by turbulent APS. The performance of this technique has been verified with simulated data and Sentinel-1A SAR data of Tenerife island.

One important feature of the proposed algorithm is that topography related APS can be estimated from interferograms with no need of any auxiliary data, except a DEM. Besides, a distinctive advantage of the proposed approach is its robustness in situations where the interferogram contains turbulent APS or spatially low-pass deformation. The spatial covariance matrix, which characterises turbulent APS, is estimated from the interferogram itself. With the usage of covariance as a weighting strategy in the improved model, the influence of turbulent component can be reduced. As sometimes the estimation of the covariance matrix can be time consuming or prone to errors for heavily decorrelated interferograms, the weighting can also be established using the pixel's distance of each arc. Shorter arcs are considered to be more reliable in the model adjustment than longer ones.

Both simulated and real data have shown than LMRTA approach can robustly estimate the stratified atmosphere in presence of turbulent one and, partially, compensate APS in the interferograms. It is important to highlight the good agreement between LMRTA results and ERA5 based APS.

Further investigations will focus on more accurate variance-covariance matrix estimation, which is a critical step to characterise turbulent APS conditions.

4

Chapter 4

Tropospheric delay mitigation using global weather forecast models

The improved empirical linear model has been proved to be effective for correcting linear correlated atmospheric artifacts over mountainous regions in Chapter 3. However, in situations where the stratified APS is not correlated to topography with a model, no matter how advanced the model is, it definitely cannot lead to a correct APS mitigation. Trying to propose more suitable models, such as a power-law model, or a self-adaptive model is always challenging. As the global weather forecast models, such as ERA5, MERRA2 datasets, are available globally, they provide an alternative way to mitigate atmospheric artifacts. Previous studies [43, 46, 49] conducted by other researchers have demonstrated its feasibility for APS compensation. Although most attempts calculate the phase delays by integrating atmospheric parameters along zenith direction, which is in fact an approximation, a promising compensation can be achieved in some cases. In this Chapter, a realistic integration strategy along LOS direction has been used for estimating atmospheric artifacts based on global reanalysis data. Section 4.1 describes drawbacks of conventional zenith method and the improvements of the direct LOS method. Section 4.2 gives a description of the test sites, datasets. In Section 4.3, Section 4.4 and Section 4.5 the algorithm validation and applications have been carried out in three different test sites, emphasizing the comparison between zenith and LOS method. Finally, in Section 4.6, the performance of different global reanalysis data for APS mitigation has been studied.

4.1 Methodology

4.1.1 Traditional methods based on global atmospheric models

Variations of temperature, pressure and humidity in the troposphere make the refractivity index, N, to be not constant. It is well known that APS is caused by the velocity change of electromagnetic waves, and it is linearly dependent on N, when passing through the troposphere along the LOS direction. The tropospheric medium is mainly made up of a wet component (water vapor) and a dry (hydrostatic) component, so the refractivity index N includes both. N_{dry} depends on the partial pressure of dry air, P, while N_{wet} depends on the water vapour partial pressure, e. Both refractivity components depend on the temperature, T. The relation of N and the different atmospheric parameters can be expressed as: [102]

$$\begin{aligned} N(T,P,e) &= k_1\frac{P}{T} + k_2\frac{e}{T} + k_3\frac{e}{T^2} \\ &= N_{dry} + N_{wet} \end{aligned} \tag{4.1}$$

Where $k_1 = 0.776KPa^{-1}$, $k_2 = 0.716KPa^{-1}$, and $k_3 = 3.75e3K^2Pa^{-1}$.

The atmospheric phase delay term, ϕ_{atm}, of a two-way travelling path between two points, $\vec{r}_1$ and $\vec{r}_2$, is proportional to the integration of the total refractivity $N(T,P,e)$ along the line joining them:

$$\phi_{atm} = \frac{-4\pi}{\lambda}10^{-6}\int_{\vec{r}_1}^{\vec{r}_2}[N_{dry}(\vec{r}) + N_{wet}(\vec{r})]d\vec{r} = \frac{-4\pi}{\lambda}10^{-6}\int_{\vec{r}_{ground}}^{\vec{r}_{sat}}[N_{dry}(\vec{r}) + N_{wet}(\vec{r})]d\vec{r} \tag{4.2}$$

Where λ is the radar wavelength. For an orbital SAR image, $\vec{r}_2$ will be the location of the satellite when the image was acquired, $\vec{r}_{sat}$, and $\vec{r}_1$ will be the ground location of the pixel for which the atmospheric artifacts are calculated, $\vec{r}_{ground}$. For an interferogram, the differential atmospheric delay $\Delta\phi_{atm}$ is the difference between both acquisitions.

With Eq. (4.2), APS correction methods based on meteorological models can calculate phase delays by using atmospheric parameters from local or global weather models. Global and regional atmospheric reanalysis data provide atmospheric variables of temperature, geopotential height, pressure and humidity with relatively high temporal and spatial resolution. To calculate phase delays from these data, for each grid point, the geopotential variable is first converted to a regular vertical metric grid parameter, the geopotential height. Atmospheric parameters are then interpolated from pressure levels to altitude levels based on the geopotential height parameter.

The different methods found in the literature [40, 41, 43, 46, 49] determine the atmospheric phase delays with an approximation. Instead of integrating along the LOS direction with Eq. (4.2), the phase delays are calculated by integrating along the zenith one. So Eq. (4.2) becomes Eq. (4.3),

$$\phi_{atm} = \frac{-4\pi}{\lambda}\frac{10^{-6}}{cos(\theta)}\int_{h_{ground}}^{h_{top}}[N_{dry}(h) + N_{wet}(h)]dh \tag{4.3}$$

Where θ is the local incidence angle (derived from the LOS direction), h_{ground} the height of the ground location and h_{top} the maximum zenithal height.

Once atmospheric phase delays are integrated along a zenithal path on the grid points using Eq. (4.3), a cubic spline interpolation in the vertical direction and a bilinear interpolation in the horizontal one are performed to obtain the phase delays for the entire SAR scene from the sparse grid points. Once having the ZTD along the vertical direction, the cosine of the incidence angle is accounted for back-projecting the result to the LOS direction. The effectiveness of the compound method is validated in several geographic and tectonic settings [40, 41, 43, 49].

4.1.2 Drawbacks of the zenith total delay approach

The way of converting delay from zenithal path to LOS is to divide it by a factor, $cos\theta$, that depends on the local incidence angle, θ, under the assumption that the atmosphere is isotropic. In reality, this is not always true as the atmosphere is a dynamically complex system which is rarely isotropic in nature. Fig. 4.1 provides a simple example to illustrate the heterogeneity of the atmosphere. The cloud located in vortex P clearly affects the path along LOS while it is not present in the zenithal path. So the projection of the zenithal delay is not a good approximation of the LOS delay. In practice, water vapour, pressure and temperature parameters can change spatially under naturally chaotic weather conditions making isotropic assumption unacceptable.

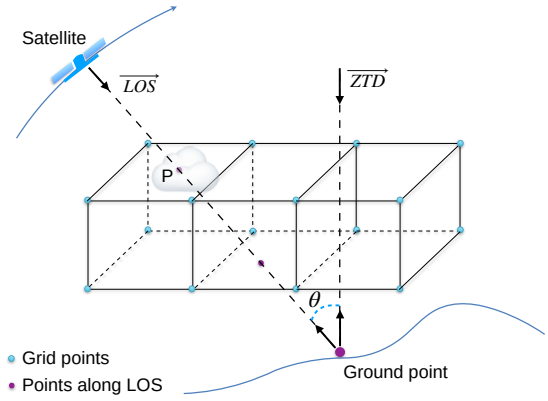

Fig. 4.1. An example of realistic atmospheric heterogeneities along the LOS path. The cloud clearly affects on the LOS directional but not in the zenithal one.

Besides, the new generation of SAR satellites can operate TOPS acquisition mode, such as Sentinel-1 and TerraSAR-X. TOPS employs a rotation of the antenna in both along track and cross track directions. Consequently, incidence angle varies in a relatively large range when compared with using conventional stripmap mode. Fig. 4.2 shows Interferometric Wide Swath (IW) and Extra Wide Swath (EW) modes of Sentinel-1, which are implemented as three and five subswaths TOPS SAR modes. The incidence angle range for IW and EW is 29.1° - 46.0° and 18.9° - 47.0°, respectively [105]. Hence atmospheric heterogeneity along zenithal and LOS direction occurs with high probability in such a big incidence angle. Consequently, the projection of ZTD to LOS delays is not a reliable approach.

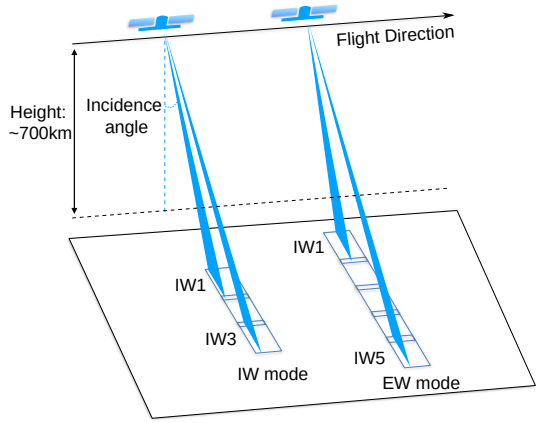

Fig. 4.2. Sentinel-1 IW and EW acquisition modes. Incidence angle varies in a relative big range.

4.1.3 Precise LOS phase delay calculation

In order to avoid possible errors caused by the approximation in Z-LOS method, the tropospheric delays actually can be estimated more accurately by integrating the refractivity along the LOS direction using Eq. (4.2).

The steps of the D-LOS algorithm are the following:

1) Determination of the sampling locations along the LOS path

The locations of both ground points and zero-Doppler satellite locations are expressed in Cartesian coordinates using the World Geodetic System 1984 (WGS84) ellipsoid with ellipsoidal heights, see the geometry in Fig. 4.3. For a general point, firstly, the three dimensional Cartesian coordinates for the ground-range point $\vec{r}_{ground}$ and its corresponding satellite zero-Doppler location $\vec{r}_{sat}$ are determined. An external DEM is back-projected to slant-range coordinates using the precise orbits to determine for each pixel of the image its corresponding geodetic coordinates. The LOS vector, $\overrightarrow{LOS}$, is calculated from the Cartesian coordinates of the ground point and the satellite,

$$\overrightarrow{LOS} = \vec{r}_{sat} - \vec{r}_{ground} \tag{4.4}$$

After calculating the LOS vector, the direction vector $\hat{u}_{LOS}$, which describes the LOS direction, is calculated from the unit vector

$$\hat{u}_{LOS} = \frac{\overrightarrow{LOS}}{\|\overrightarrow{LOS}\|} = [\hat{u}_x, \hat{u}_y, \hat{u}_z] \tag{4.5}$$

Once the direction vector is determined, the coordinates (P_{ix}, P_{iy}, P_{iz}) for any arbitrary point P_i along LOS can be easily obtained. The required sampling, ΔLOS, depends on the resolution of the available GAM data. In practice, for an efficient computation and

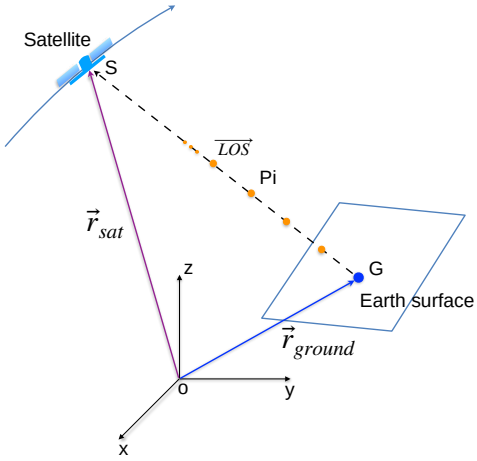

Fig. 4.3. Geometry of LOS path in Cartesian coordinate system.

with no loss of reliability a LOS spatial sampling of 200 m has been set.

$$\begin{aligned} P_{ix} &= G_x + (\Delta LOS \cdot i)\hat{u}_x \\ P_{iy} &= G_y + (\Delta LOS \cdot i)\hat{u}_y \\ P_{iz} &= G_z + (\Delta LOS \cdot i)\hat{u}_z \end{aligned} \tag{4.6}$$

with i an integer.

With the above equations, locations along LOS for each ground-range point can be determined. After that, an interpolation strategy is designed to obtain the atmospheric parameters on these locations from the available GAM data.

2) Interpolation of atmospheric parameters

What GAM datasets provide are a grid in geographic coordinates of meteorological parameters, which include pressure, temperature and humidity. For example, with ERA5 data, sampling values of the grids are 37 pressure levels in altitude and 31 km in horizontal. In order to obtain the required finer spatial sampling of the atmospheric state parameters on the desired locations, a cubic spline interpolation along the vertical direction and a bilinear interpolation in the horizontal plane are utilized. Additionally, as refractivity N above a reference elevation is relatively stable, locations with elevations higher than a specific threshold can be considered negligible. The determination of the reference elevation is discussed in Section 4.3.1.

When dealing with the vertical interpolation, the atmospheric parameters need to be interpolated with the same datum of the DEM, WGS84 in this paper. The different height types, geoidal or ellipsoidal, and all geodetic datums should be taken into consideration. One parameter included in GAM data is the geopotential, $\Phi(h)$, which is widely used in the meteorology community. It can be easily converted to geopotential height, H_p, simply dividing by the gravity constant at mean sea level, g,

$$H_p = \frac{\Phi(h)}{g} \tag{4.7}$$

Then, the geometric altitude H_g referring Earth's mean sea level is a function of the geopotential altitude H_p:

$$H_g = \frac{EH_p}{E - H_p} \tag{4.8}$$

in which E is the Earth radius. Finally, as the DEM used considers ellipsoid heights, the ellipsoid altitude H_e is obtained by adding the geoid height N obtained from the Earth Gravitational Model 1996 (EGM96) geopotential model.

$$H_e = H_g + N \tag{4.9}$$

Once all altitudes are ellipsoidal referred to the WGS84 datum, the atmospheric parameters can be interpolated along the vertical direction. It has to be noticed that the precise orbits of the satellites are also in Cartesian coordinates referred to WGS84 and so all calculations are unified to the same framework.

4.2 Test sites, ERA5 dataset and SAR data processing

4.2.1 Tenerife island, Spain

Tenerife island is situated in the Atlantic Ocean opposite the northwestern coast of Africa. It is a rugged and volcanic island sculpted by successive eruptions throughout its history. Fig. 4.4a shows the location of the test site. The center of the island is dominated by the volcano Teide. With an elevation of 3718 m above sea level it is the third largest volcano in the world. A total of 15 eruptions have been historically recorded on the island [106]. Among various geodetic monitoring tools spread on this island, InSAR techniques have demonstrated its capacity for volcano monitoring purposes [107–109]. However, as the topography variation (from sea level to 3718 m) on Tenerife is significant jointly with the proximity of the sea, most differential interferograms are affected by both stratified and turbulent atmospheric artifacts. The work in [110] applied a method using the WRF model [111] to mitigate atmospheric effects, but without considering the realistic phase delay calculation along LOS. Their results show WRF as a promising tool for APS mitigation while failing at anisotropic atmospheric situations.

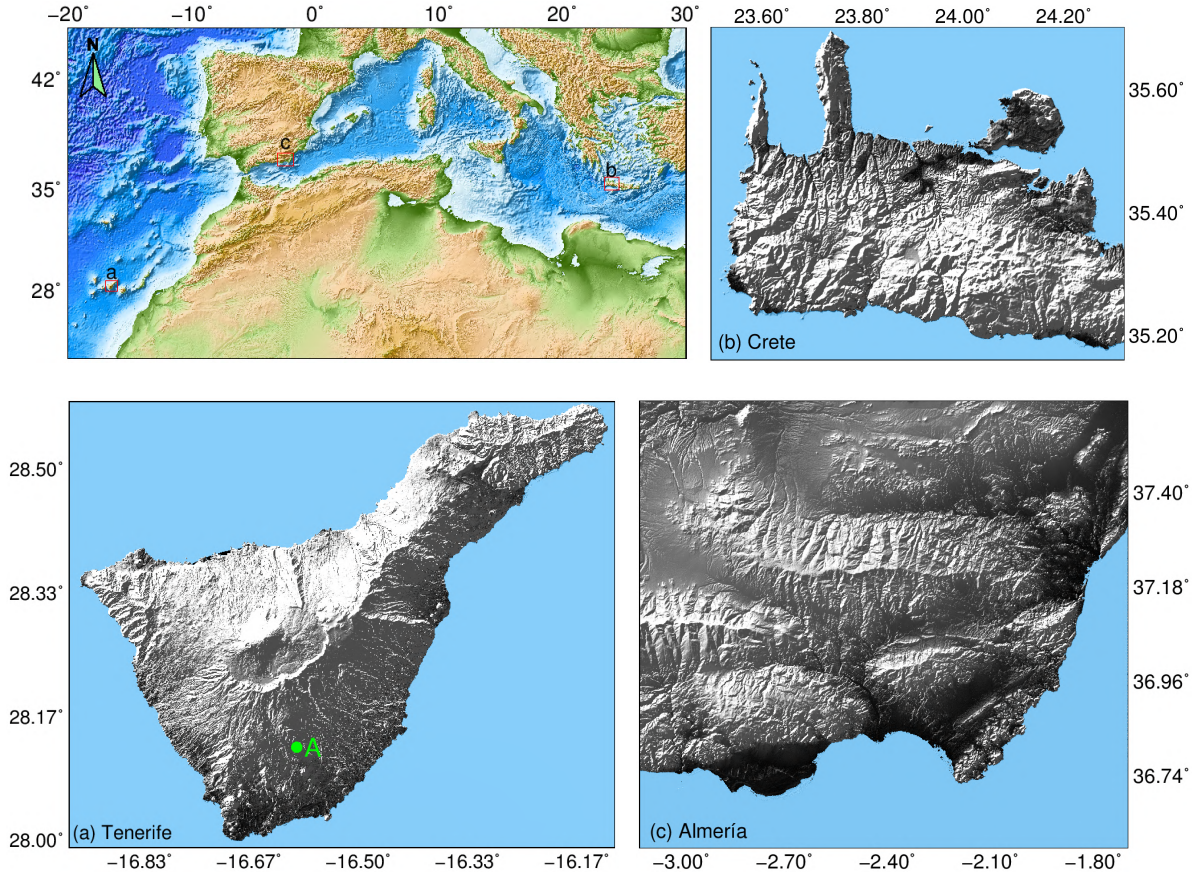

Fig. 4.4. Overview geographic locations of the test sites: Tenerife island, Spain, Almería, Spain and Crete, Greece. (a), (b) and (c) shows local topography of each study area. The ERA5 meteorological data at the grid point A will be taken as an example to visualize the vertical interpolation in Section 4.3.1.

4.2.2 Crete, Greece

The island of Crete is located in the Eastern Mediterranean (Fig. 4.4), which lies within the outer fore-arc of the largest and most active subduction zone in Europe. PSI techniques have been explored to detect the active vertical surface deformation patterns across Crete [112]. However, its offshore location and significant topography incur atmospheric artifacts which need to be considered. Previous study [103] showed that Crete is an ideal study area, because it represents a complicated set of tropospheric conditions involving maritime-terrestrial heating and moisture contrasts combined with extensive topographical variations.

4.2.3 Almería, Spain

Almería basin lies in one of the most arid parts of Europe, receiving an average rainfall of only 250 mm per year [113]. Given historical patterns of agricultural and urban development, the water demand has been largely supplied from ground water, leading to the situation of water overexploitation. Consequently, Almería basin suffers ground subsidence induced by aquifer exploitation. PSI has become the optimum technique for periodically monitoring subsidence. A study from [113] by using DInSAR revealed that between 2003 and 2009, this region suffered a subsidence rate ranging from 1.7 to 5 $mm/year$. Unfortunately, interferograms in this area are also vulnerable to APS contamination due to the strong topography and its coastal location (Fig. 4.4c), which may lead to unreliable estimations of subsidence patterns and values.

4.2.4 ERA5

In this thesis, the advanced D-LOS algorithm is validated using ERA5 dataset, which is a global atmospheric reanalysis product provided by the ECMWF. ERA5 is the latest generation of atmospheric reanalysis data after ERA-Interim generated using Copernicus Climate Change Service Information [45]. This product covers the period from 1979 to present as ERA-Interim covers. Compared with the 6 hours temporal and 79 km spatial sampling of ERA-Interim data, ERA5 provides a much higher resolution in both time and space. Hourly reanalysis data is available at a horizontal resolution of 31 km with ERA5 data. The higher temporal resolution minimizes the errors due to the time difference between SAR acquisition and meteorological data. The nearest ERA5 data to the SAR images acquisition times are selected. Another advantage of ERA5 data is that uncertainty estimates for all parameters are available at 3-hour intervals and at a horizontal resolution of 62 km. The uncertainties can be used as reliability weights when interpolating the atmospheric parameters, as well as potentially applied to evaluate the trustworthiness of the calculated APS maps.

4.2.5 SAR datasets and data processing

The performance of Z-LOS and D-LOS algorithms are evaluated based on Sentinel-1 SAR datasets from the ESA. In the three test sites, the selected SAR images are acquired under complex weather conditions from different seasons in order to validate the

general applicability of the corrections. Differential interferograms were generated using SUBSIDENCE-GUI software, developed by UPC [20], with USGS SRTM DEMs and precise orbits from Copernicus POD Service to remove topographic phase components. All differential interferograms have been unwrapped using the SNAPHU package [114].

4.3 Algorithm validation in Tenerife island

The D-LOS algorithm is being validated demonstratively in Tenerife island using Sentinel-1 and ERA5 data, with explicit comparison with Z-LOS. The SAR images in Tenerife are acquired at 07:02 in the morning, very close to the hourly ERA5 reanalysis data. The atmospheric conditions between SAR images and ERA5 data are assumed functionally simultaneous, as each are separated by only two minutes.

4.3.1 Implementation of the improved method

1) Cubic spline interpolation of atmospheric parameters

Although ECMWF provides 37 pressure levels reanalysis data higher than 40 km above the sea level, in practice beyond a certain elevation the parameters can be considered constant. A cubic spline interpolation is applied on grid points from sea level to a reference elevation for the temperature, the pressure and the relative humidity along the vertical direction. Fig. 4.5 visualizes the vertical interpolation results for different parameters at the grid point A (see Fig. 4.4a). It is clear that the curves for all parameters are smooth, with no abrupt changes, and so the cubic spline interpolation is adequate. The interpolation results at the point A represent a general situation of the low-pass behaviour of the parameters. The interpolated data along the vertical direction will further provide input data for the horizontal interpolation on the desired locations along the LOS direction.

2) Maximum altitude determination

As mentioned above, refractivity of tropospheric changes in both temporal and spatial domains. However, since the interferometric phase is the pixel-wise difference between two SAR acquisitions, the atmospheric delays depend on the refractivity variations rather than their singly imaged absolute values. Other meteorological measuring tools such as sounding measurements provide detailed vertical profile of atmospheric state. The work in [16] analysed radiosonde data in De Bilt, the Netherlands, and found that the variability of the refractivity above 5 km can be considered negligible. The work in [43] assumed negligible effects of atmospheric stratification above 30 km. The work in [30] studied weather balloon data and found that relative delays above 7-13 km height do not differ significantly. In the Tenerife island case and for grid point A, 153 relative phase delays obtained from all possible combinations of 18 ERA5 data from different days are displayed as a scatter plot in Fig. 4.6. It can be clearly seen that the relative phase delays converge to zero with the increasing of altitude. In order to optimize the integration of refractivity along the LOS direction it is not necessary to consider all elevations but only those that affect the relative phase delays. The maximum altitude to consider, h_{top}, can be set to those for which the standard deviation of the relative delays is smaller than 1 rad. The

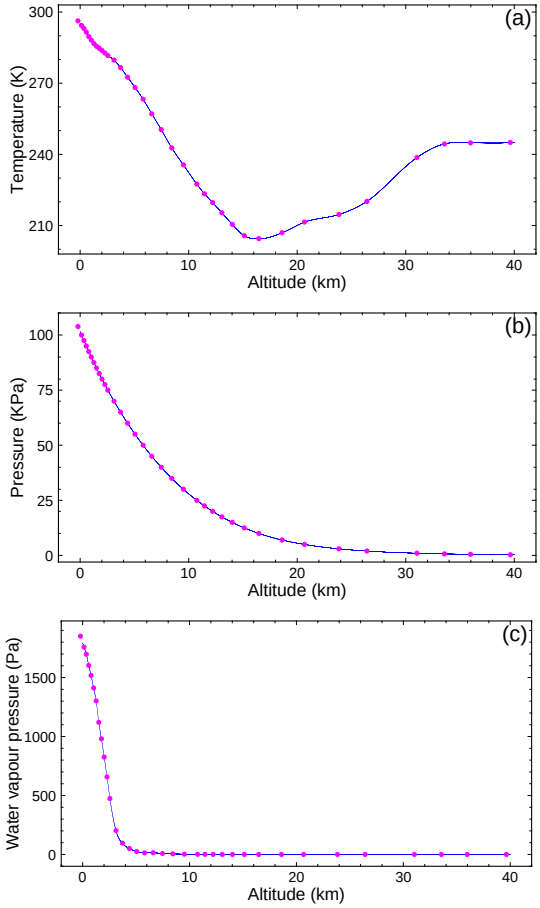

Fig. 4.5. Spline interpolation for temperature, pressure and water vapour pressure along the vertical direction.

maximum altitude value to be considered in the integration for the Tenerife case can be set to 28 km.

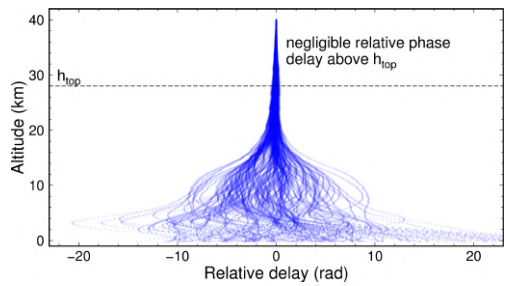

Fig. 4.6. Relative tropospheric phase delay along vertical direction. The darker the color is, the more the scatters overlap.

4.3.2 Tenerife island case study analysis

In order to reduce as much as possible the phase contributions caused by DEM inaccuracies and deformation in the interferometric phase, the spatial perpendicular baselines and temporal baselines have been limited to be less than 50 m and 36 days, respectively. In addition, as it can be seen in Table 4.1, the interferograms are all made from two acquisitions covering two consecutive months to minimize the temporal baseline and, at the same time, maximize the phase quality. The one year time span also guarantees a diversity of climate and weather conditions. Fig. 4.7 shows all the selected differential interferograms covering the period from September 2015 to September 2016. At a first glance the phases are strongly correlated with topography. This phase pattern can also be caused either by errors on the DEM or the orbital information. In order to exclude this factor, the relationship between the number of fringes and the spatial baseline has been analysed. Fig. 4.8 shows a scatter plot of the interferograms, in which it is evident that the number of fringes does not follow a linear trend with the spatial baselines.

Table 4.1: Statistical comparison of different mitigation methods for 12 Sentinel-1 interferograms used over the Tenerife island. Values in parentheses are correction percentage (Original-Residual)/Original.

Ifg.	SLC1	SLC2	Baseline	Phase SD		
				Original	Z-LOS residual	D-LOS residual
Ifg1	25/09/2015	07/10/2015	18.2 m	5.32	3.57 (33%)	1.94 (64%)
Ifg2	07/10/2015	12/11/2015	-29.7 m	5.66	2.89 (49%)	2.54 (55%)
Ifg3	12/11/2015	18/12/2015	20.5 m	4.59	2.44 (47%)	1.65 (64%)
Ifg4	06/12/2015	11/01/2016	-14.1 m	5.99	1.75 (71%)	1.40 (77%)
Ifg5	23/01/2016	04/02/2016	10.6 m	4.23	3.30 (22%)	2.75 (35%)
Ifg6	28/02/2016	11/03/2016	20.0 m	4.15	2.36 (43%)	2.14 (48%)
Ifg7	11/03/2016	16/04/2016	-11.6 m	3.74	2.39 (36%)	2.04 (45%)
Ifg8	04/04/2016	10/05/2016	44.9 m	4.01	3.25 (19%)	2.47 (38%)
Ifg9	10/05/2016	15/06/2016	-12.2 m	2.98	3.62 (-)	2.30 (23%)
Ifg10	15/06/2016	09/07/2016	19.9 m	3.46	2.97 (14%)	2.37 (32%)
Ifg11	21/07/2016	14/08/2016	17.5 m	6.79	3.83 (44%)	2.62 (61%)
Ifg12	26/08/2016	07/09/2016	21.7 m	6.62	4.85 (27%)	2.64 (60%)
Mean					(37%)	(50%)

To underscore the complexity of atmospheric artifacts in Tenerife, a scatter plot relating height and unwrapped original phase of 105,137 selected PSs for interferogram 20160721-20160814 (Ifg11) is shown in Fig. 4.9(f). From the scatter plot, it is clear that there is no strict linear or apparent power-law correlation between atmospheric artifacts and topography, therefore correction methods based on empirical models may fail for interferograms having similar characteristics as this one.

Fig. 4.9 shows the correction results of Ifg11 by using different methods, in which the first row presents the original interferogram, the predicted APSs and its corresponding residuals. The unwrapped phase-elevation scatter plots are shown in the second row. Atmospheric artifacts can be clearly seen in the unwrapped original interferogram (Fig. 4.9(a)), with phase patterns increasing from coast (low elevation) towards the center

of the area (top of the mountain). The short temporal baseline also ensures that the phase disturbances due to localized terrain deformation are extremely small and therefore do not affect the analysis of the overall behavior of the atmospheric compensation.

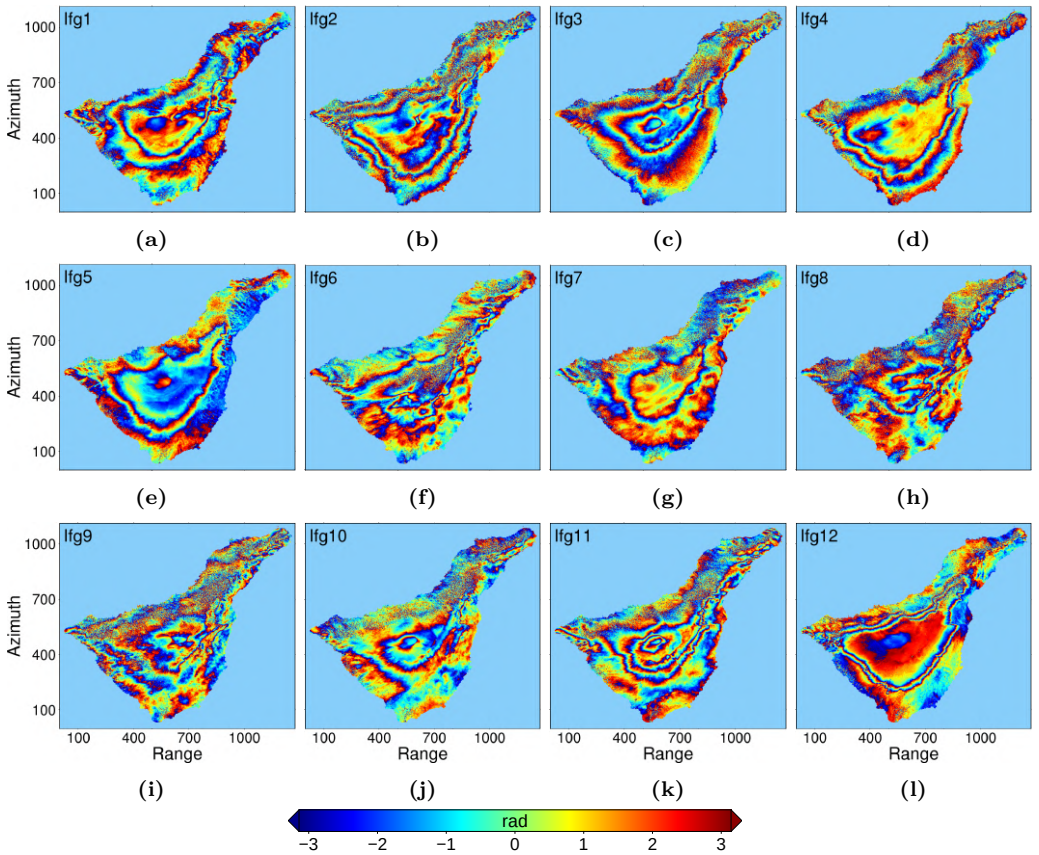

Fig. 4.7. Original wrapped differential interferograms covering one entire year over Tenerife island, Spain. Each interferogram connects two consecutive months. Detailed temporal and spatial baselines information for each interferogram can be found in Table 4.1.

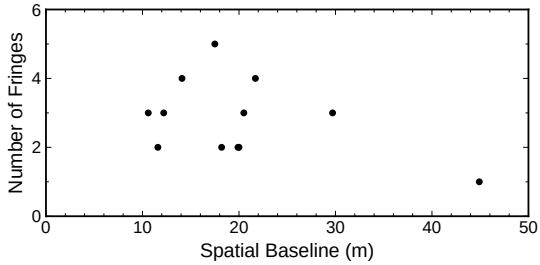

Fig. 4.8. Relationship between number of fringes and spatial baseline.

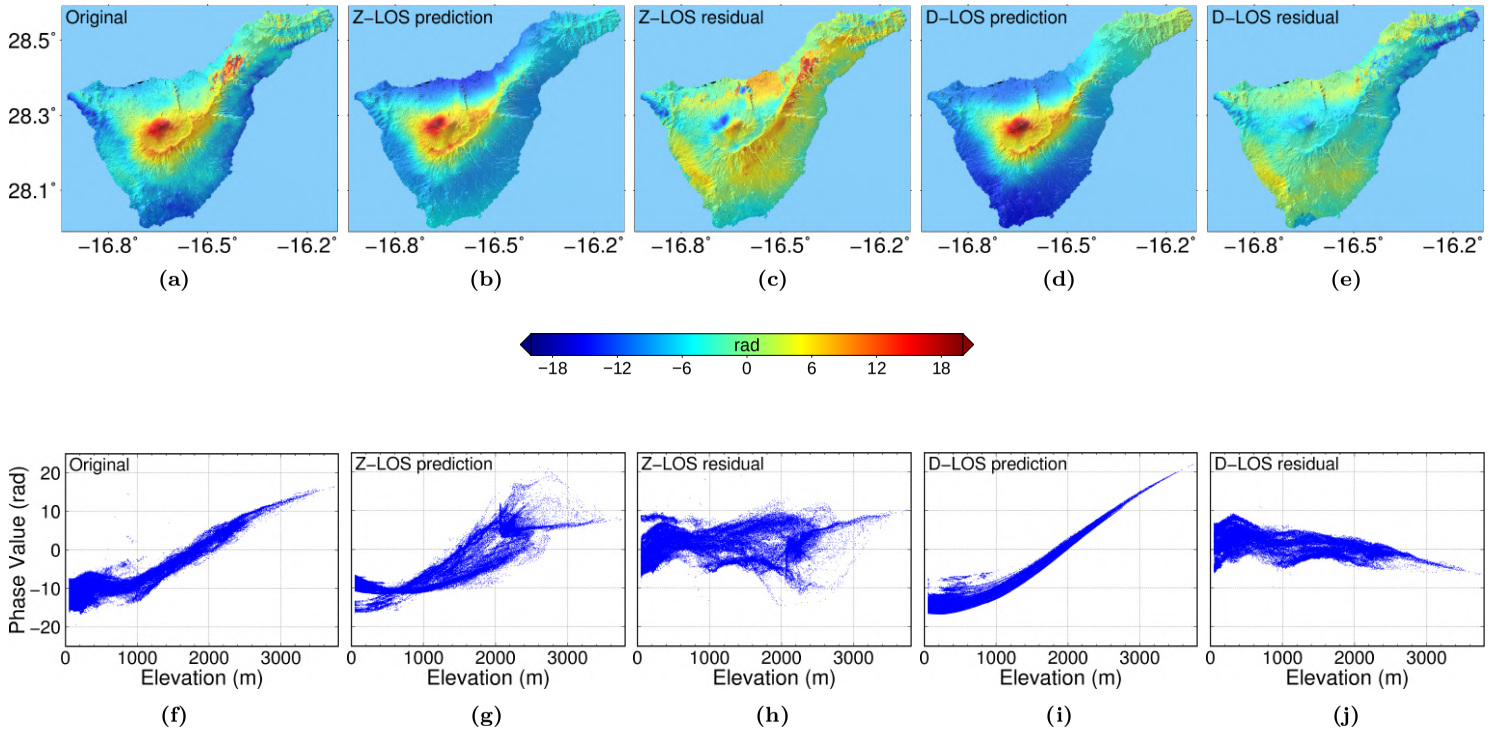

Fig. 4.9. 20160721-20160814 (Ifg11) case study of APS compensation over Tenerife. (a)-(e) represents the original interferogram, Z-LOS predicted APS, residue phase after Z-LOS correction, D-LOS predicted APS and residue phase after D-LOS correction, respectively. (f)-(j) is phase-elevation scatters for original phase, Z-LOS predicted APS, residue phase after Z-LOS correction, D-LOS predicted APS and residue phase after D-LOS correction, respectively.

With the traditional zenith to LOS method (Z-LOS), i.e., zenith path delay is first calculated and then back-projected to LOS divided by a factor $cos\theta$, APS can be mitigated to some extent. Fig. 4.9(b) and Fig. 4.9(c) show the estimated Z-LOS APS and its residual phase after APS correction, respectively. From the predicted APS, a similar delay trend is observed across the whole interferogram. After correcting with Z-LOS delays, long-wavelength tropospheric delays can be removed. As it can be seen from the residual phase, the phase dispersion has been reduced. But Z-LOS method fails in places where the topography changes abruptly. As a result, the residual phase (Fig. 4.9(c)) exhibits a large variation around the top of the mountain and a significant residual phase appears along the SW to NE direction in the middle of the interferogram. Besides, the corresponding phase-elevation scatter plots of predicted APS (Fig. 4.9(g)) and residual phase (Fig. 4.9(h)) also prove the limitations of Z-LOS method estimating delays, especially at elevations between 2000 m and 3700 m, where the phases vary significantly. Looking at the residual phase-elevation plots (Fig. 4.9(h)), phases fluctuate around zero, but with a wide variation. From the statistical point of view, the Z-LOS method reduces for this particular case the SD from 6.79 to 3.83 *rad*.

With the D-LOS method, both predicted APS and residual phase show a better performance when compared with Z-LOS. Specifically, D-LOS predicted APS presents a very similar phase pattern with the original interferogram in terms of magnitude and location, especially at the center of the interferogram. The uniformity of the residual phase in Fig. 4.9(e) further demonstrates its excellent performance. Compared with the Z-LOS results, the residual interferogram presents a smaller phase dispersion. The clear improvement can also be seen when comparing the estimated APS phase-elevation scatter plots (Fig. 4.9(i)) with the original one (Fig. 4.9(f)) as they both show an almost identical trend. A further inspection of the phase residues in Fig. 4.9(j) shows that the residual phases are distributed around zero with a narrow variation. After applying the D-LOS correction the SD is being reduced by a 61%, down to 2.62 *rad*.

4.3.3 Statistics analyses

To evaluate whether the improvements shown in the above case can also be achieved in a more general situation, statistical analyses of 12 short temporal baseline interferograms in Tenerife covering an entire year have been carried out. In Table 4.1, the *Original* column shows large phase SD for each differential interferogram, due to strong APS contamination. After applying the Z-LOS correction method, all interferograms except Ifg9 present a phase SD reduction. For Ifg9, the SD even increased from 2.98 to 3.62 *rad*. In other words, the Z-LOS method cannot correct the APS properly in this specific case. In the best case (Ifg4), the Z-LOS approach achieved a 71% SD reduction. On the other side, the D-LOS method performance is comprehensively better than the Z-LOS method. For all pairs, D-LOS can achieve a considerable SD reduction. The best case occurs in Ifg4, reducing the SD a 77% from 5.99 to 1.40 *rad*, while even in the worst case (Ifg9), it provides a 23% reduction. The statistical SD values of *Original*, *Z-LOS residual* and *D-LOS residual* in Table 4.1 are visualized in Fig. 4.10. Once again, it is clear that both Z-LOS and D-LOS can mitigate APS delay, but D-LOS consistently outperforms the Z-LOS approach.

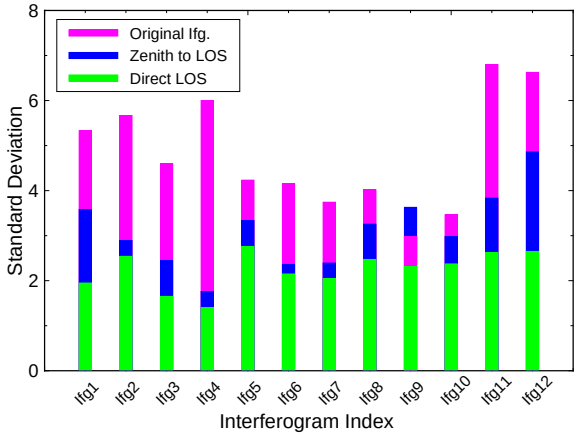

Fig. 4.10. SD comparison of original interferograms (magenta bars), residual phases corrected from Z-LOS method (blue bars) and residual phases after D-LOS correction (green bars) on all the 12 pairs in Tenerife.

4.4 Application for Crete, Greece

In Crete, strong variation of topography and an extensive coastline is prone to suffering tropospheric phase delays. From the one year dataset of Sentinel-1 images, eight representative interferograms, each one covering two consecutive months (see Table 4.2) have been generated. They represent almost one year of climate conditions except the period from December to March. The interferograms from December to March have been discarded as the area was affected by snow on the Lefka Ori mountain, making the differential phases useless. It is also noted that in this area the time difference between Sentinel-1 acquisition and ERA5 reanalysis is 24 minutes. It is acceptable compared with other global reanalysis data (e.g. ERA-Interim, MERRA) with 6 hours interval.

Table 4.2: Statistical comparison of different mitigation methods for 8 Sentinel-1 interferograms used in Crete, Greece. Values in parentheses are correction percentage (Original-Residual)/Original.

Ifg.	SLC1	SLC2	Baseline	Phase SD		
				Original	Z-LOS residual	D-LOS residual
Ifg1	24/04/2017	06/05/2017	-15.8 m	5.12	3.30 (36%)	1.31 (74%)
Ifg2	06/05/2017	11/06/2017	-21.6 m	4.20	2.17 (48%)	2.08 (50%)
Ifg3	11/06/2017	29/07/2017	40.9 m	4.04	3.82 (5%)	3.43 (15%)
Ifg4	17/07/2017	22/08/2017	-52.8 m	5.14	4.78 (7%)	4.33 (16%)
Ifg5	22/08/2017	03/09/2017	-28.1 m	4.66	4.17 (11%)	3.12 (33%)
Ifg6	27/09/2017	09/10/2017	-37.4 m	4.80	3.69 (23%)	2.89 (40%)
Ifg7	21/10/2017	02/11/2017	-12.8 m	5.63	4.13 (27%)	3.01 (47%)
Ifg8	26/11/2017	08/12/2017	44.0 m	2.88	2.34 (19%)	2.07 (28%)
Mean					(22%)	(38%)

In Fig. 4.11 one interferogram (Ifg8), formed from two acquisitions during the wet season, is selected to illustrate the performance of the D-LOS algorithm. The short temporal and spatial baseline preclude deformation and DEM phase errors, so the primary phase component can be considered as atmospheric artifacts in the original unwrapped interferogram (Fig. 4.11(a)). The main visible feature is the phase trend from low elevations to the top of the mountains. This feature is more visible looking at the phase-elevation scatter plots in Fig. 4.11(f).

With the Z-LOS method, this feature can be partly estimated (Fig. 4.11(b)) and so the dominant trend can be removed with the correction, as it can be seen in Fig. 4.11(c). However, paying attention to certain areas the Z-LOS method has over-predicted the tropospheric delay locally. The scatter plots of Z-LOS predicted and corrected phases shown in Fig. 4.11(g) and Fig. 4.11(h) further prove this. From these plots, it is clear that the Z-LOS predicted phase delay shows a large variance, producing relatively large fluctuations in the residual phases. Statistically, the phase SD is reduced a 19% from 2.88 to 2.34 *rad*.

With the D-LOS algorithm, the patterns of predicted APS in Fig. 4.11(d) show a good correspondence with the original interferogram, both in location as well as amplitude. The D-LOS corrected interferogram (Fig. 4.11(e)) shows relatively small phase values, fluctuating around zero. The observed D-LOS phase-elevation pattern shown in Fig. 4.11(i) matches the features of the original interferogram. Additionally, it is important to highlight the smaller variance in the residual phase compared with the Z-LOS one. The good correspondence between original interferogram and D-LOS prediction is also confirmed by a significant SD reduction in the phase residues, a 28% from 2.88 to 2.07 *rad*.

Additionally, statistical analyses for all eight interferograms have been carried out and listed in Table 4.2. In this test site, both Z-LOS and D-LOS methods can achieve variance reductions for all interferograms. Moreover, once again the D-LOS algorithm outperforms the Z-LOS approach for each individual pair in terms of SD reduction. For Z-LOS, the best correction case is achieved for Ifg2, showing a 48% variance reduction. While Ifg1 is the best case for D-LOS, where the phase SD is reduced a 74%. For both methods, the worst correction is for Ifg3, with reductions of 5% and 15% respectively. Fig. 4.12 shows graphically the performance of both methods detailed in Table 4.2.

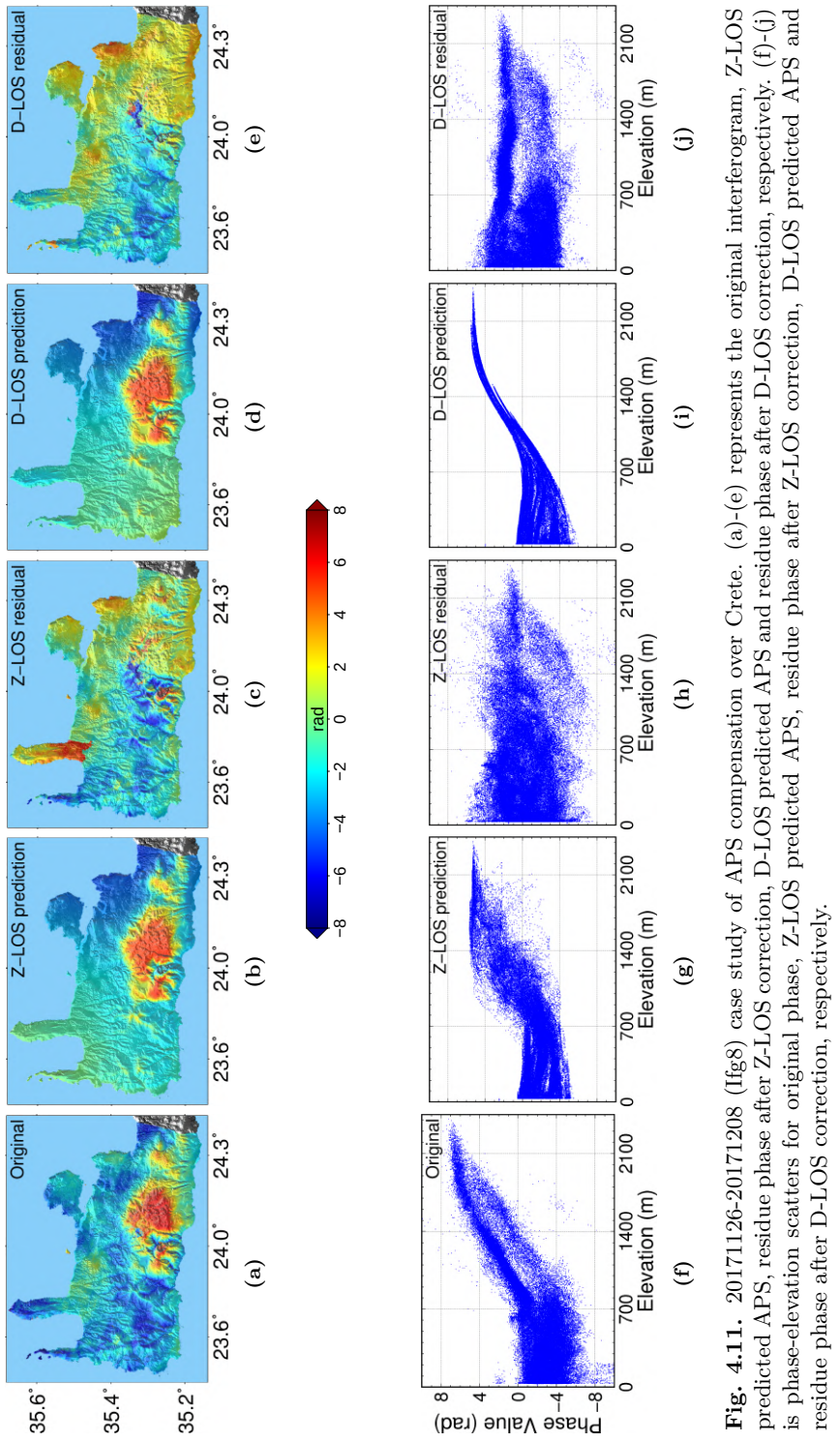

Fig. 4.11. 20171126-20171208 (Ifg8) case study of APS compensation over Crete. (a)-(e) represents the original interferogram, Z-LOS predicted APS, residue phase after Z-LOS correction, D-LOS predicted APS and residue phase after D-LOS correction, respectively. (f)-(j) is phase-elevation scatters for original phase, Z-LOS predicted APS, residue phase after Z-LOS correction, D-LOS predicted APS and residue phase after D-LOS correction, respectively.

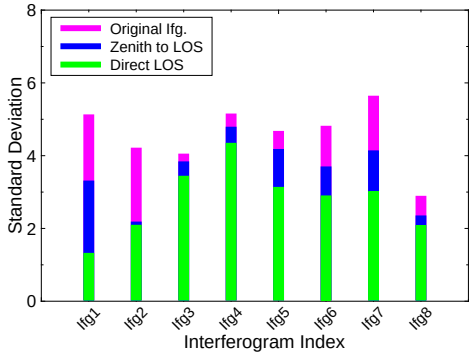

Fig. 4.12. SD comparison of original interferograms (magenta bars), residual phases corrected from Z-LOS method (blue bars) and residual phases after D-LOS correction (green bars) on all the 8 pairs in Crete.

4.5 Application for Almería, Spain

Almería is a region located in the southeast of the Iberian Peninsula. Its southeast coastline opens to western Mediterranean Sea, while its interior northwest is mountainous. It is interesting to highlight that, in the center of the study area, there is a basin surrounded by mountains, so the atmospheric conditions were expected to be complicated due to the Mediterranean climate and the presence of mountains. To evaluate the performance of APS correction, twelve interferograms covering one year with short temporal spans are selected in this test site. Among them, the pair 20171031-20171124 (Ifg11) is explicitly analysed as a typical example (Fig. 4.13).

The time difference between ERA5 and Sentinel-1 acquisition is less than 10 minutes in this case. Again, it can be assumed that the atmospheric conditions would be very similar in such a short time difference. Fig. 4.13(a) shows how the differential interferometric phase due to the atmospheric artifacts is strongly correlated with the topography. The Z-LOS predicted phase, shown in Fig. 4.13(b), is able to partially retrieve the trend of the original interferogram, especially in the flat areas, but it fails at some of the mountainous locales. The bad performance of the estimated APS is better highlighted with the residual phases shown in Fig. 4.13(c). The phase SD is reduced only a 8%, from 2.54 to 2.33 *rad* with the Z-LOS correction. A significant improvement in the performance can be observed with the D-LOS approach. Specifically, the D-LOS prediction shown in Fig. 4.13(d) exhibits a very similar phase pattern with the original one in terms of the shape and amplitude. As Fig. 4.13(e) shows, the tropospheric delays all-over the interferogram have been reduced except in some localized areas located near the top of some mountains. With the D-LOS method, the phase SD is reduced a 39% to 1.79 *rad*.

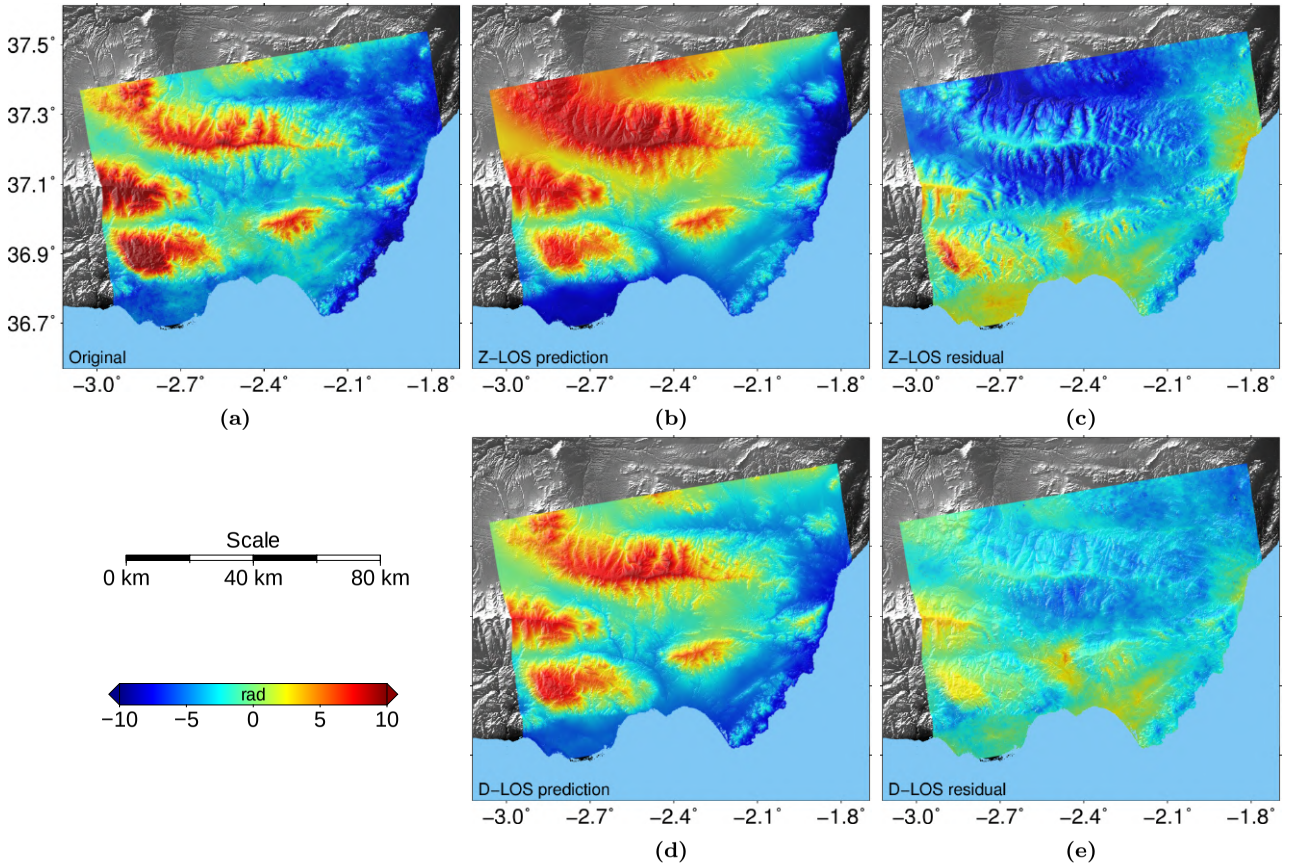

Fig. 4.13. 20171031-20171124 (Ifg11) case study of APS compensation over Almería. (a) original interferogram. (b-c) Z-LOS predicted APS and corrected interferogram with Z-LOS method. (d-e) D-LOS predicted APS and corrected interferogram with D-LOS method.

Both methods have been applied to the all the interferograms and the performance results are listed in Table 4.3 and graphically illustrated in Fig. 4.14. It is clear from Fig. 4.14 that, for most interferograms, the Z-LOS mitigation has reduced the tropospheric delays, except for Ifg3 and Ifg7. For these two cases, the SD values actually have been increased. After correcting with the D-LOS method, all interferograms show an obvious SD reduction. Overall, compared with the average 14% mitigation achieved by the Z-LOS method, the D-LOS algorithm is able to achieve a 29% reduction on average.

Table 4.3: Statistical comparison of different mitigation methods for 12 Sentinel-1 interferograms used in Almería, Spain. Values in parentheses are correction percentage (Original-Residual)/Original.

Ifg.	SLC1	SLC2	Baseline	Phase SD		
				Original	Z-LOS residual	D-LOS residual
Ifg1	17/12/2016	10/01/2017	81.5 m	4.19	4.09 (2%)	3.52 (16%)
Ifg2	22/01/2017	27/02/2017	-43.1 m	4.13	3.81 (8%)	3.46 (16%)
Ifg3	27/02/2017	11/03/2017	28.4 m	5.38	6.28 (-)	3.29 (39%)
Ifg4	11/03/2017	28/04/2017	-12.4 m	5.13	4.28 (17%)	3.86 (25%)
Ifg5	04/04/2017	10/05/2017	-14.1 m	4.37	4.01 (8%)	3.68 (16%)
Ifg6	28/05/2017	09/06/2017	33.8 m	5.93	4.23 (29%)	3.25 (45%)
Ifg7	09/06/2017	03/07/2017	-31.8 m	4.60	5.20 (-)	3.22 (30%)
Ifg8	27/07/2017	08/08/2017	-19.4 m	6.12	4.71 (23%)	3.54 (42%)
Ifg9	08/08/2017	01/09/2017	43.0 m	7.53	6.97 (7%)	5.52 (27%)
Ifg10	01/09/2017	07/10/2017	-25.3 m	4.66	3.50 (25%)	3.17 (32%)
Ifg11	31/10/2017	24/11/2017	22.3 m	2.95	2.71 (8%)	1.79 (39%)
Ifg12	12/11/2017	06/12/2017	-49.5 m	2.54	2.33 (8%)	2.00 (21%)
Mean					(14%)	(29%)

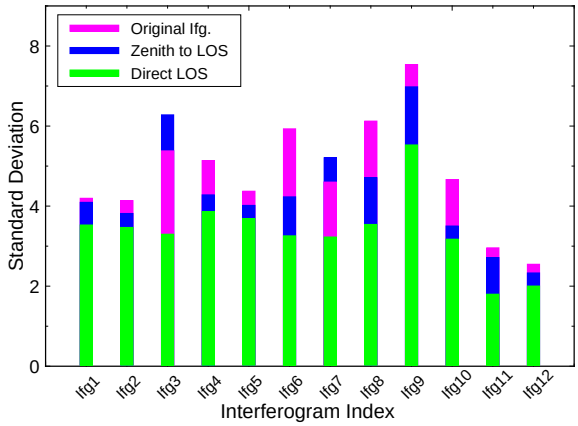

Fig. 4.14. SD comparison of original interferograms (magenta bars), residual phases corrected from Z-LOS method (blue bars) and residual phases after D-LOS correction (green bars) on all the 12 pairs in Almería.

4.6 Comparison of different global atmospheric models

The improvements of D-LOS correction method compared with Z-LOS based method have been validated in the above sections using ERA5 pressure levels data. Nowadays, besides ERA5 global reanalysis data, other global weather forecast models, which are developed by different institutions and designed for variety of climate applications, are also available for public use. On account of different mathematical models are used in those global numerical prediction models, the reanalysed weather forecast data can be distinct from one model to the others. Thus, it is interesting to explore the capability of those reanalysis data for mitigating APS application. In this Section, with D-LOS calculation algorithm, the performance of using different global weather forecast datasets (ERA-Interim, ERA5 and MERRA2) to correct APS for InSAR are evaluated and discussed in the three test sites.

4.6.1 ERA-Interim

The ERA-Interim is a global atmospheric reanalysis data produced by the ECMWF, which was started from 2006 and was maintained until the end of 2018. ERA-Interim is based on IFS release Cy31r2, used for operational forecasting at ECMWF. Its product covers the period from 1979 to 2019, describing weather, ocean-wave, land-surface conditions, troposphere as well as stratosphere. It provides atmospheric variables every 6 hours with an approximate spatial resolution of 79 km [115]. In terms of ERA-Interim model levels data, there are 137 levels defined. In this Chapter, for the purpose of mitigating APS for InSAR, it is straightforward to use the 37 pressure levels, which is interpolated from model levels data.

4.6.2 MERRA

Modern Era-Retrospective Analysis for Research and Applications (MERRA) is a NASA global reanalysis product using the GEOS-5, providing estimates of temperature, water vapor partial pressure, and geopotential height along 42 pressure levels, at 1/2x2/3 degrees resolution along longitude and latitude respectively. These reanalysis parameters are generated every 6 hours (at 00:00, 06:00, 12:00 and 18:00 UTC) daily covering the period from 1979 to present [116]. There are two versions of MERRA data: MERRA and MERRA2. Compared to MERRA, the assimilation system in MERRA2 enables assimilation of modern hypersperctral radiance and microwave observations, along with GPS-Radio Occultation datasets. The MERRA2 will replace the original MERRA dataset and is the one used in this Chapter.

In order to explore the performance of different global forecast data for correcting APS, the above described datasets, including ERA5, are utilized in this Chapter. The main parameters for these models are summarized in Table 4.4. In addition to this table, the distribution of grids points for each dataset on the three test sites is displayed in Fig. 4.15, in which grids points in each rectangle are used for the calculation of APS.

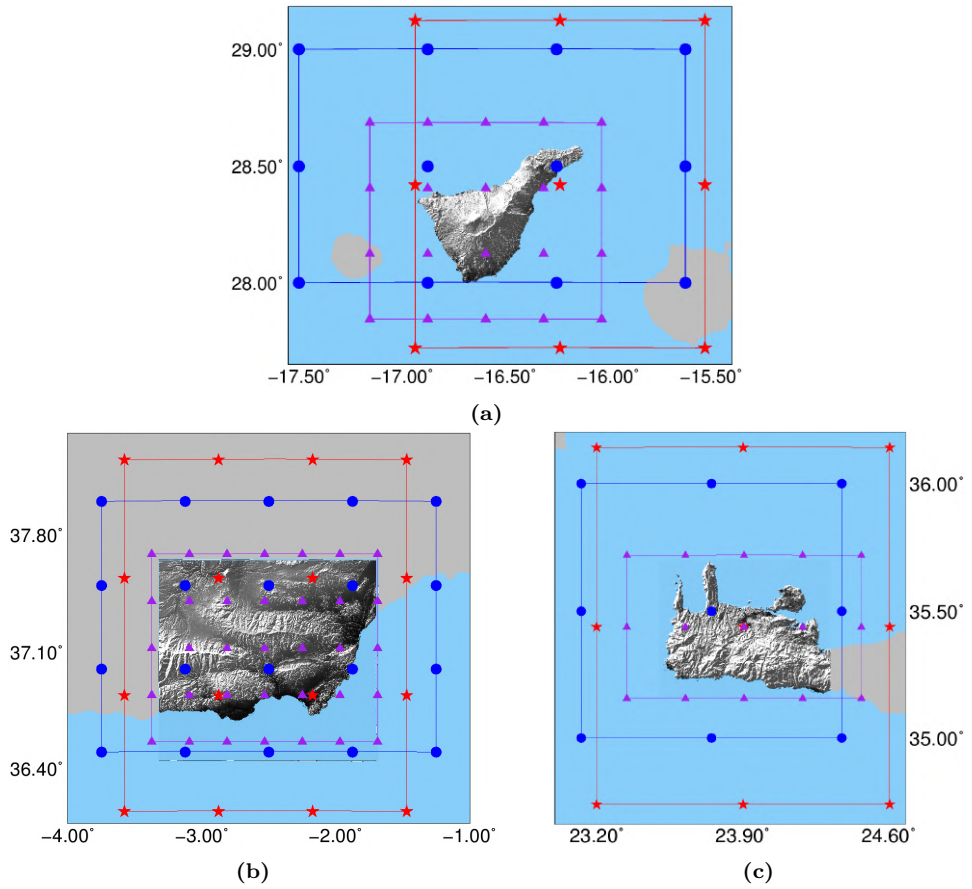

Fig. 4.15. Distribution of meteorological data for Tenerife (a), Almería (b) and Crete (c) test sites. Red stars represent the ERA-Interim data. Purple triangles correspond ERA5 grids data. Blue circles stand for MERRA2 grids. Each rectangle shows the range of grids data used for APS calculation.

Table 4.4: Comparison of different global atmospheric models, ERA-Interim, ERA5 and MERRA2.

Dataset	Spatial resolution	Temporal resolution	Pressure levels
ERA-Interim	0.75x0.75 deg	6 hours	37
ERA5	0.28x0.28 deg	1 hour	37
MERRA2	0.50x0.67 deg	6 hours	42

4.6.3 Tenerife, Spain

Firstly, to simulate the atmospheric phase delay closer to the SAR acquisitions, the closest weather assimilation data are chosen. In Tenerife test site, all the SAR images used in the experiment are acquired at 07:02 Coordinated Universal Time (UTC) in the morning. Therefore, the global reanalysis data at 06:00, 07:00 and 06:00 UTC for ERA-Interim,

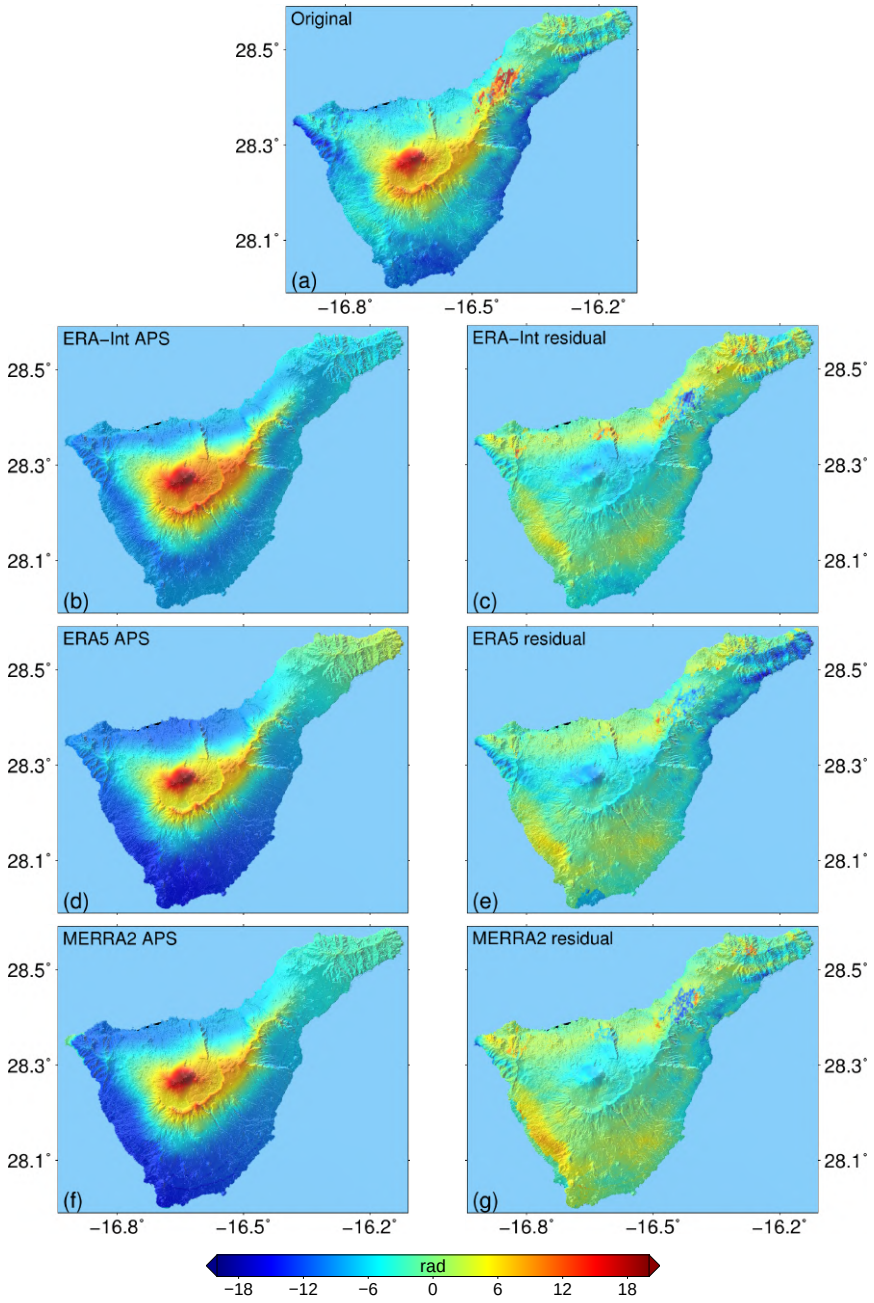

Fig. 4.16. 20160721-20160814 (Ifg11) case study of APS compensation over Tenerife using ERA-Interim, ERA5 and MERRA2 reanalysis data. (a) represents the original interferogram. (b), (d) and (f) shows D-LOS predicted APS using ERA-Interim, ERA5 and MERRA2 data respectively. (c), (e) and (g) represents the corresponding residual phase.

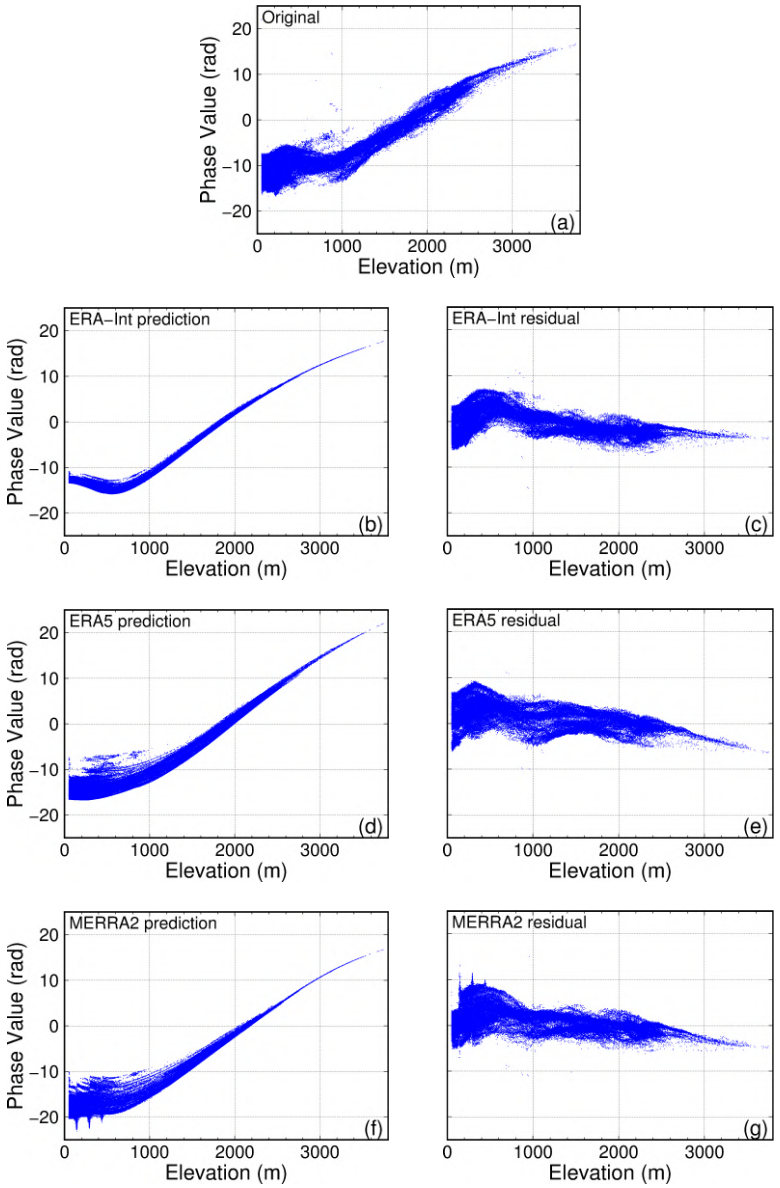

Fig. 4.17. 20160721-20160814 (Ifg11) case study of phase-elevation scatters for APS compensation over Tenerife using ERA-Interim, ERA5 and MERRA2 reanalysis data. (a) is phase-elevation scatters for the original interferogram. (b), (d) and (f) represents the phase-elevation scatters for ERA-Interim, ERA5 and MERRA2 prediction. (c), (e) and (g) is the scatters for the residual after ERA-Interim, ERA5 and MERRA2 correction respectively.

ERA5 and MERRA2 are used respectively. Similar to the discussion in Section 4.3.2 in Chapter 4, the interferogram 20160721-20160814 (Ifg11) is taken as an example for

detailed interpretation, while the remaining 11 pairs will be analysed statistically.

Fig. 4.16 represents compensation results using different global weather forecast models. As it is clearly labeled in the subfigures, Fig. 4.16(a) shows the original unwrapped differential interferogram. Fig. 4.16(b), Fig. 4.16(d) and Fig. 4.16(f) illustrates the estimated APS from ERA-Interim, ERA5 and MERRA2 reanalysis data respectively. Fig. 4.16(c), Fig. 4.16(e) and Fig. 4.16(g) shows the corresponding residual phase after correction. In general, all the three reanalysis data have the ability to mitigate the tropospheric delays to some extent for this particular case. As it can be seen that the simulated APS by the three datasets have a similar pattern with the original interferogram. Meanwhile, the phase fluctuation in the residual phases after each correction has reduced to a relative low level.

It is hardly to evaluate which one has the best performance visually, no matter from the estimated APS or the residual phases. Hence, phase-elevation scatters results are presented in Fig. 4.17 as well, to further explore the capability that the different reanalysis datasets can achieve. The phase-elevation scatters from ERA-Interim (Fig. 4.17(b)), ERA5 (Fig. 4.17(d)) and MERRA2 (Fig. 4.17(f)) shows a very similar trend to the one from the original interferogram. On account of the fact that neither a strict linear regression nor a power-law function can model this trend, the empirical model based methods would definitely overestimate or underestimate the topography related atmospheric artifacts. From this point of view, the weather forecast data can lead to a better correction than empirical models. The relative slight fluctuation in the phase-elevation scatters (Fig. 4.17(c), Fig. 4.17(e), Fig. 4.17(g)) from the residual figures also demonstrates the significant mitigation by the three global reanalysis data. Once again, their performances are similar with each other from the phase-elevation scatters, consequently it is hardly to conclude which one is the best.

During the period of this interferogram, there are no apparent activities related to ground movement. Therefore, in such a short spatial baseline (17.5 m) and temporal baseline (24 days), the phase deviation should mainly come from atmospheric artifacts. The SD of the original interferogram is 6.79 rad, while the SD for the residual phase is 2.56 rad, 2.62 rad and 2.49 rad after ERA-Interim, ERA5 and MERRA2 correction respectively, corresponding to 62%, 61% and 63% phase reductions. From the statistical point of view, the differences between the three datasets correction are small enough to be ignored.

Fig. 4.18 visually presents the differences between the estimated APS by using the three datasets. It can be seen clearly that these values are quite consistent over the entire island. Once again, it proves that the three datasets have demonstrated a similar feasibility for APS correction for this particular case.

To further investigate the correction performance of these global weather reanalysis data, a statistical analysis is applied to all the 12 interferograms. As it can be seen in Table 4.5, using SD as an assessment metric, the correction based on ERA-Interim and MERRA2 can achieve SD reduction for almost all the interferograms except the one Ifg9, in which the SD even increases after ERA-Interim and MERRA2 correction. Statistically, the ERA-Interim data can achieve 49.0% SD reduction on average for the 11 interferograms, while the MERRA2 results have a 48.7% phase reduction on average. Compared to the ERA-Interim and MERRA2 datasets, on the one hand, the ERA5 data

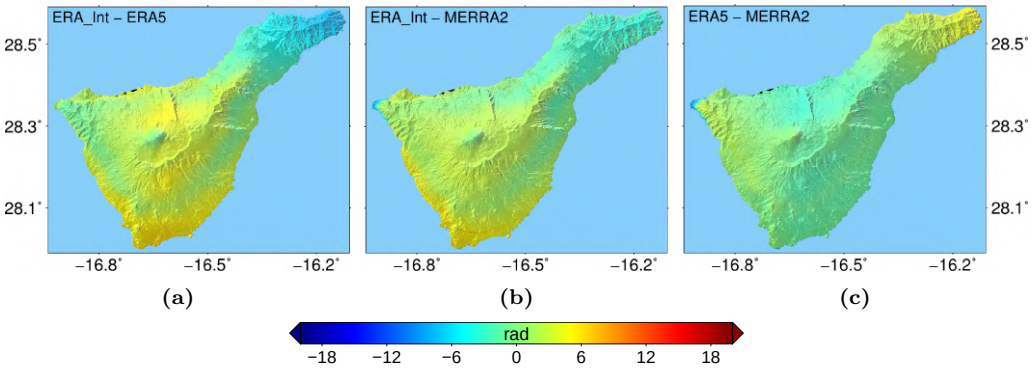

Fig. 4.18. Differences between the estimated APS for the 20160721-20160814 (Ifg11) case study over Tenerife. (a) is the difference between ERA-Interim APS and ERA5 one. (b) represents the APS difference between ERA-Interim and MERRA2. (c) is the APS difference between ERA5 and MERRA2.

Table 4.5: Statistical comparison using D-LOS mitigation method with different GAM data for 12 Sentinel-1 interferograms in the Tenerife island. Values in parentheses are correction percentage (Original-Residual)/Original.

Ifg.	Interferogram pair	Phase SD	SD residual		
		Original	ERA-Interim	ERA5	MERRA2
Ifg1	20150925-20151007	5.32	3.63 (32%)	1.94 (64%)	2.77 (48%)
Ifg2	20151007-20151112	5.66	2.81 (50%)	2.54 (55%)	3.31 (42%)
Ifg3	20151112-20151218	4.59	2.20 (52%)	1.65 (64%)	2.65 (42%)
Ifg4	20151206-20160111	5.99	1.68 (72%)	1.40 (77%)	3.23 (46%)
Ifg5	20160123-20160204	4.23	2.25 (47%)	2.75 (35%)	1.53 (64%)
Ifg6	20160228-20160311	4.15	1.90 (54%)	2.14 (48%)	1.82 (56%)
Ifg7	20160311-20160416	3.74	1.71 (54%)	2.04 (45%)	1.87 (50%)
Ifg8	20160404-20160510	4.01	2.61 (35%)	2.47 (38%)	2.66 (34%)
Ifg9	20160510-20160615	2.98	3.18 (-)	2.30 (23%)	3.15 (-)
Ifg10	20160615-20160709	3.46	2.33 (33%)	2.37 (32%)	2.49 (28%)
Ifg11	20160721-20160814	6.79	2.56 (62%)	2.62 (61%)	2.49 (63%)
Ifg12	20160826-20160907	6.62	3.43 (48%)	2.64 (60%)	2.45 (63%)
Mean			(49.0%)	(50.2%)	(48.7%)

has the ability to reduce phase SD for all the interferograms, including the one Ifg9. On the other hand, the SD reduction that the ERA5 can achieve is up to 50.2% for the 12 interferograms, which is higher than the other two datasets.

In order to further explore the distinctive correction performance for the Ifg9 case, Fig. 4.19 presents the original interferogram, estimated APS by using ERA-Interim, ERA5 and MERRA2 data. It can be seen visually from the original interferogram (Fig. 4.19(a)) that there is a phase trend from the South-West to the North-East in the region with relatively low altitude. Besides, at the top of the mountain, atmospheric artifacts are significant as well. Among the three estimated APS, the one using ERA5 data (Fig. 4.19(c)) can obtain a similar atmospheric artifacts trend especially in the South-West and North-

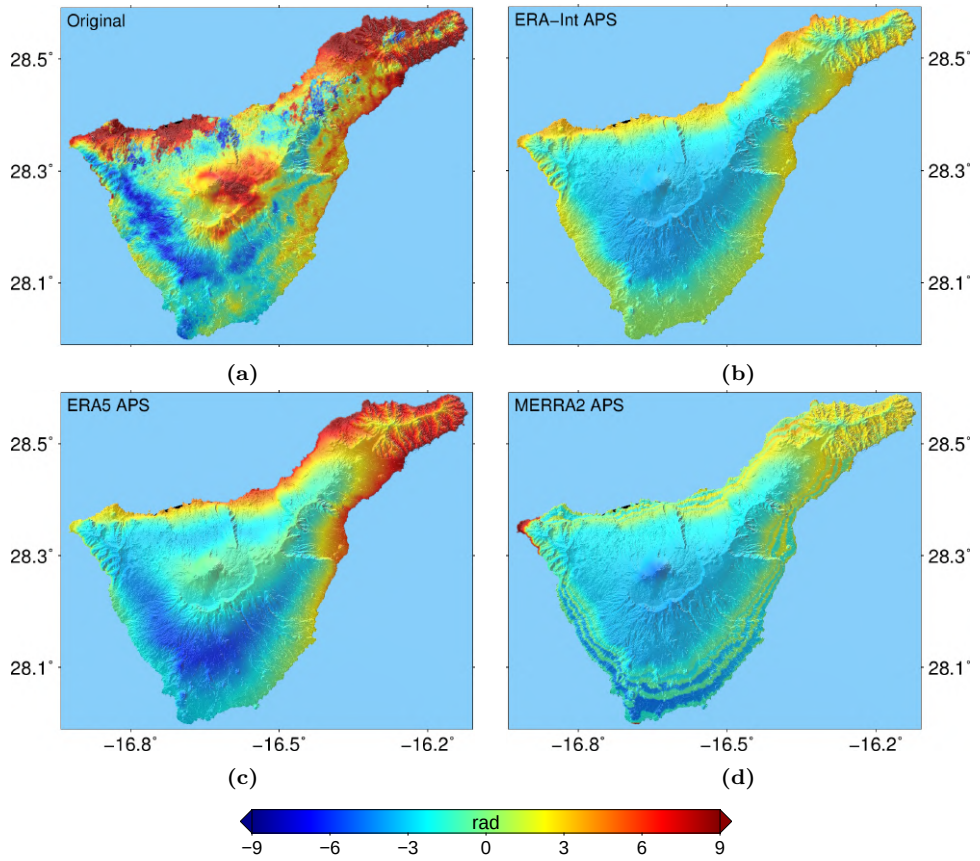

Fig. 4.19. 20160510-20160615 (Ifg9) case study of APS compensation in Tenerife using ERA-Interim, ERA5 and MERRA2 reanalysis data. (a) represents the original interferogram. (b), (c) and (d) shows D-LOS predicted APS using ERA-Interim, ERA5 and MERRA2 data respectively.

East area. But it fails to correct the part at the top of the mountain and in the North. As a result, the ERA5 correction can only reduce the SD by 23%. The other two reanalysis data perform worse on this correction. From Fig. 4.19(b) and Fig. 4.19(d) it can be seen that they can hardly obtain the atmospheric artifacts pattern. After the two corrections, the SD values even increase compared to the original one.

4.6.4 Almería, Spain

The comparison analyses of ERA-Interim, ERA5 and MERRA2 APS correction are also applied to Almería, Spain. In this case, the weather reanalysis data at 18:00 UTC, very close to the Sentinel-1 SAR images acquisition time (18:10 UTC), for all the three datasets are chosen to simulate the atmospheric artifacts. Similar to the Tenerife test site, a case study for Ifg11 and statistical comparison for 12 interferograms will be discussed in Almería as following.

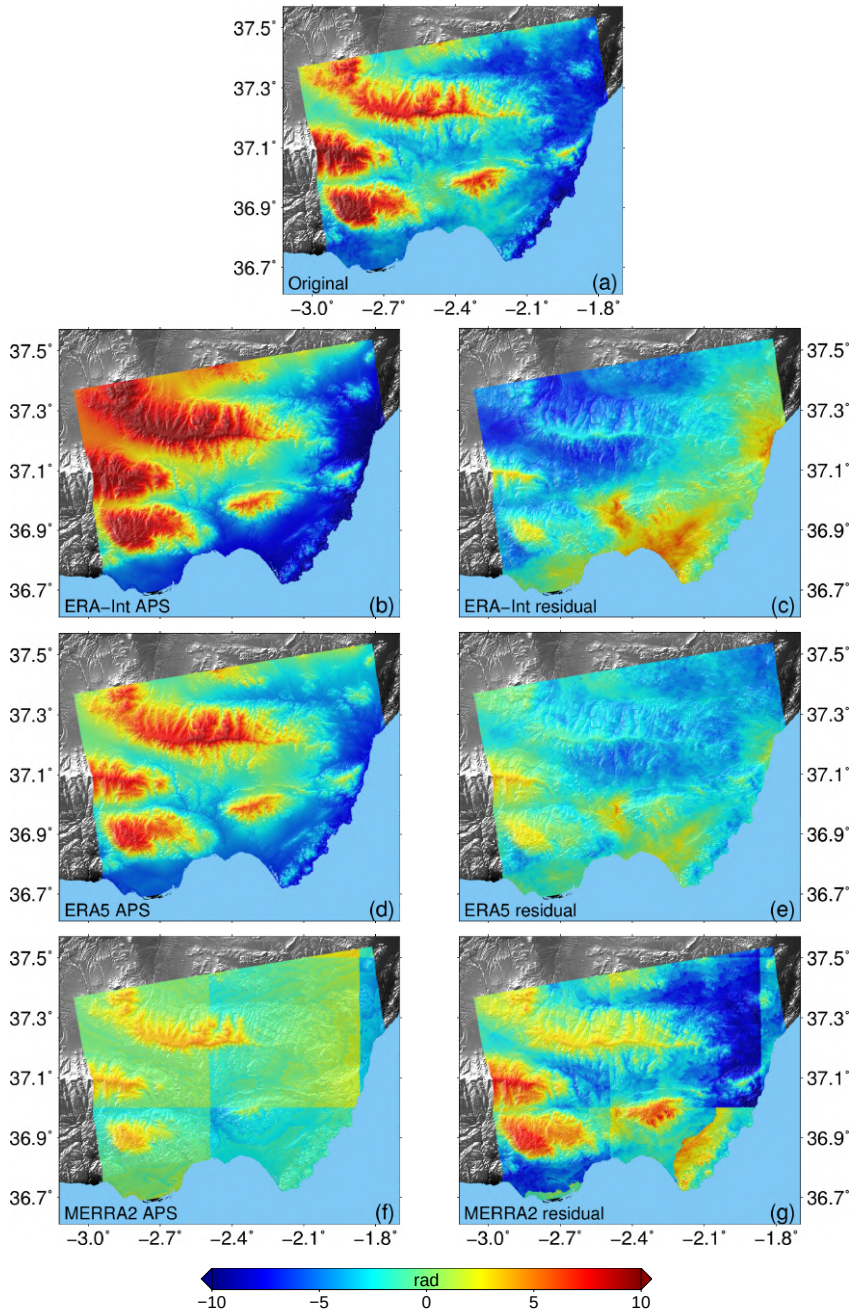

Fig. 4.20. 20171031-20171124 (Ifg11) case study of APS compensation over Almería using ERA-Interim, ERA5 and MERRA2 reanalysis data. (a) represents the original interferogram. (b), (d) and (f) shows D-LOS predicted APS using ERA-Interim, ERA5 and MERRA2 data respectively. (c), (e) and (g) represents the corresponding residual phase.

The compensation results for the Ifg11 case is shown in Fig. 4.20, depicting the original interferogram, estimated APS from ERA-Interim, ERA5 and MERRA2, as well as the residual phases after correction. For this particular case, an apparent difference can be observed from the three global reanalysis data corrections. To be more specific, from Fig. 4.20(b), the ERA-Interim data can obtain a similar atmospheric pattern than the original interferogram, but it underestimates the magnitude of the phase delay. As it can be seen that with the same color scale, the color for the ERA-Interim estimated APS is more intense compared to the original phase, especially in the North-West mountainous area (dark red) and the South-East coastal line (dark blue). The residual phase in Fig. 4.20(c) further demonstrates the underestimation, in which the magnitude is still significant, particularly in the North-West mountainous region and the South-East bay. Compared to the ERA-Interim, a significant improvement can be noticed in the ERA5 compensation from both the estimated APS and residual phase. The ERA5 simulated APS (Fig. 4.20(d)) looks like a duplicate of the original interferogram not only from the pattern but also from the magnitude point of view. As a result, the residual phase (Fig. 4.20(e)) after employing the correction shows a relative uniform distribution, without significant phase fluctuation. In terms of the MERRA2 data, it cannot model the atmospheric artifacts for this particular case. On the one hand, the phase magnitude simulated by MERRA2 data (Fig. 4.20(f)) is much less than the original interferogram as well as the ones estimated by ERA-Interim and ERA5 data. On the other hand, an inconsistent phenomenon among different bursts can be seen from the estimated APS in Fig. 4.20(f). It is probably caused by the discontinuous atmospheric parameters among the grid points provided by MERRA2 in this test site. The MERRA2 correction consequently even deteriorates the original interferogram. After applying it, substantial phase variation can be observed from the residual phase in Fig. 4.20(g). From the above visual analysis, the ERA5 correction performs the best among the three global weather forecast data. While the MERRA2 leads to the worst correction. A statistical analysis also agrees the above conclusion. The best SD reduction is conducted by ERA5 correction, which decreases the SD from 2.95 *rad* to 1.79 *rad* by a 39% reduction. The ERA-Interim ranks the second, decreasing the SD up to 2.13 *rad*, with 28% reduction. However, after applying MERRA2 correction, the SD even increases, which means a deterioration caused by the MERRA2 data.

Moreover, statistical analyses are conducted to all the 12 pairs to further explore the APS mitigation by global reanalysis datasets. The results in Table 4.6 show distinct difference among the three weather forecast data. Firstly, regarding the ERA-Interim mitigation, it is true that the phase SD is reduced for all the 12 interferograms. But an attentive observation reveals that the SD reduction is very slightly for 5 pairs (Ifg2, Ifg5, Ifg7, Ifg8 and Ifg12), only ranging from 1% up to 8%. Therefore, it is hardly to conclude the correction for the five pairs is reliable or not. For the other seven interferograms, the ERA-Interim data can perform better from the SD reduction point of view. Overall, 15.7% phase reduction can be achieved on average for the 12 interferograms by ERA-Interim data correction. Secondely, using ERA5 data, an outstanding performance is presented in terms of SD reduction. In general, every simulated atmospheric artifacts by ERA5 is able to decrease the phase deviation for a corresponding interferogram. In the best case (Ifg6), the estimated phase delays can reduce the variance by 45%, while even the worst cases (Ifg1, Ifg2 and Ifg5) the SD reduction is up to 16%. Compared to the average 15.6% reduction by ERA-Interim, the number almost doubles for ERA5

Table 4.6: Statistical comparison using D-LOS mitigation method with different GAM data for 12 Sentinel-1 interferograms in Almería, Spain. Values in parentheses are correction percentage (Original-Residual)/Original.

Ifg.	Interferogram pair	Phase SD	SD residual		
		Original	ERA-Interim	ERA5	MERRA2
Ifg1	20161217-20170110	4.19	3.71 (11%)	3.52 (16%)	3.80 (9%)
Ifg2	20170122-20170227	4.13	4.10 (1%)	3.46 (16%)	3.70 (10%)
Ifg3	20170227-20170311	5.38	4.03 (25%)	3.29 (39%)	4.26 (21%)
Ifg4	20170311-20170428	5.13	3.55 (31%)	3.86 (25%)	3.16 (38%)
Ifg5	20170404-20170510	4.37	4.27 (2%)	3.68 (16%)	4.33 (1%)
Ifg6	20170528-20170609	5.93	4.67 (21%)	3.25 (45%)	4.33 (27%)
Ifg7	20170609-20170703	4.60	4.38 (5%)	3.22 (30%)	5.87 (-)
Ifg8	20170727-20170808	6.12	5.61 (8%)	3.54 (42%)	6.61 (-)
Ifg9	20170808-20170901	7.53	5.90 (22%)	5.52 (27%)	6.89 (8%)
Ifg10	20170901-20171007	4.66	3.17 (32%)	3.17 (32%)	4.18 (10%)
Ifg11	20171031-20171124	2.95	2.13 (28%)	1.79 (39%)	3.29 (-)
Ifg12	20171112-20171206	2.54	2.50 (2%)	2.00 (21%)	2.32 (9%)
Mean			(15.7%)	(29.0%)	(14.8%)

data, 29.0% to be exactly. Thirdly, the correction based on MERRA2 data provides the worst results. In detail, this data is unable to model the atmospheric artifacts for three interferograms, i.e. Ifg7, Ifg8 and Ifg11, in which the phase SD increases after MERRA2 compensation. It is also hardly to mitigate the APS for Ifg5, because the phase deviation only decreases from 4.37 *rad* to 4.33 *rad* by 1% reduction. Overall, the MERRA2 data can only achieve an average 14.8% phase SD reduction in the Almería test site.

From the above discussion, it can be concluded that the ECMWF family datasets (ERA-Interim and ERA5) provide better APS compensation than MERRA2 for the 12 interferograms in Almería. Furthermore, the latest generation ERA5 data outperforms the last ERA-Interim comprehensively.

4.6.5 Crete, Greece

The compensation method based on different global reanalysis datasets is further applied to Crete, Greece. The SAR images are acquired at 04:24 UTC. For the purpose of minimizing the influence of time difference, ERA-Interim data at 06:00, ERA5 at 04:00 and MERRA2 at 06:00 UTC are used to simulate atmospheric artifacts. In the following, a case study (Ifg8) is visually depicted and discussed, followed by statistical analyses for all the interferograms.

Fig. 4.21 displays the original interferogram, estimated APS as well as residual phases for the Ifg12 case study by using the three global reanalysis datasets. Visually, it seems that the simulated APS (Fig. 4.21(b), (d) and (f)) from the three datasets represents a similar pattern with the original interferogram, a phase trend correlated with the topography. If we inspect them in a meticulous way, minor differences can be found. With respect to the original interferogram, besides a phase trend from the low terrain to the mountainous region, localized atmospheric artifacts (blue clusters) can also be found in

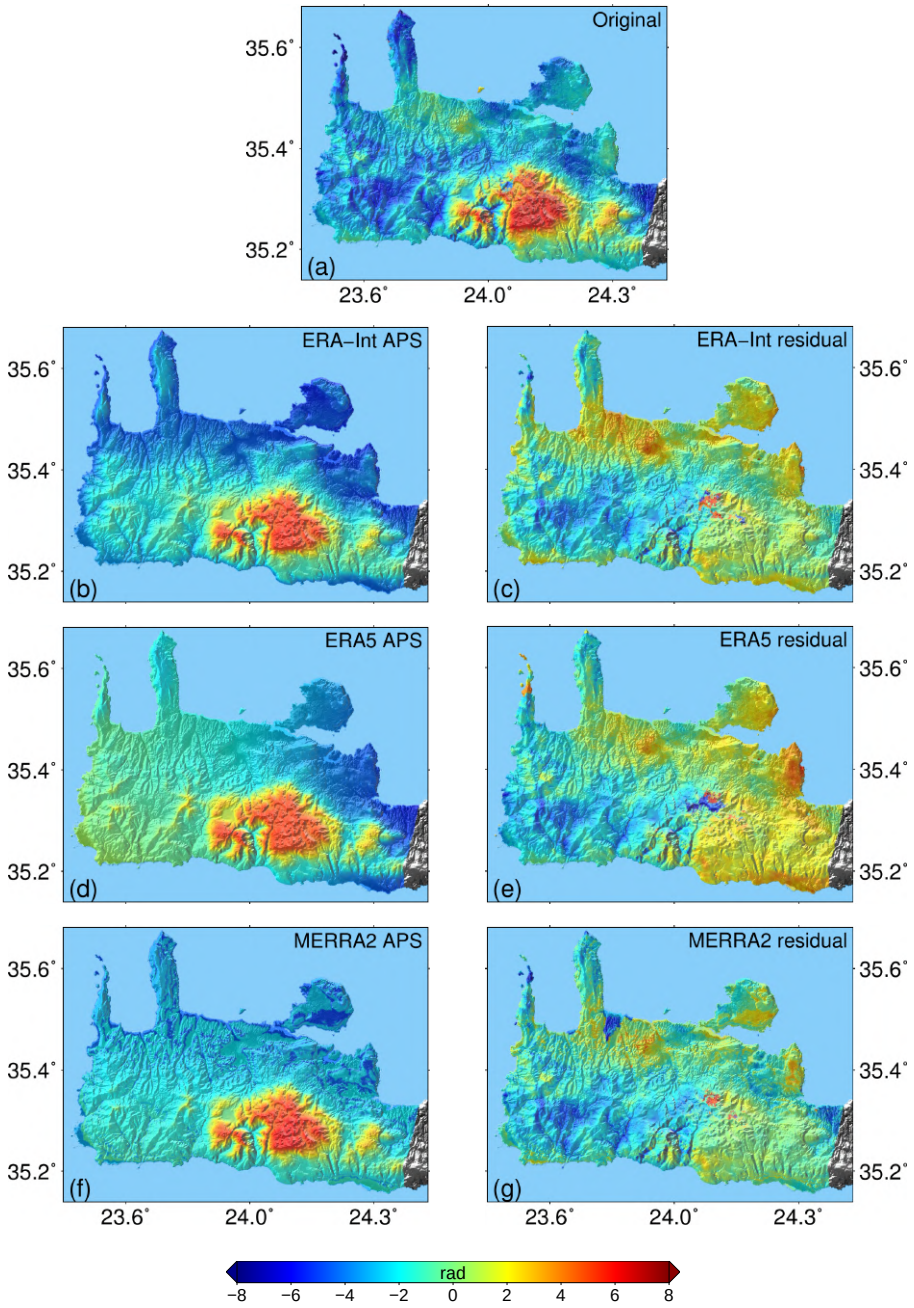

Fig. 4.21. 20171126-20171208 (Ifg8) case study of APS compensation over Crete using ERA-Interim, ERA5 and MERRA2 reanalysis data. (a) represents the original interferogram. (b), (d) and (f) shows D-LOS predicted APS using ERA-Interim, ERA5 and MERRA2 data respectively. (c), (e) and (g) represents the corresponding residual phase.

the low terrain regions. Regarding the APS estimated from ERA-Interim in Fig. 4.21(b), an additional trend along the North to South direction is apparent. In terms of the APS simulated from ERA5 data in Fig. 4.21(d), there is an extra trend from the West to the East. From this point of view, the MERRA2 provides a better APS prediction. As no additional trend is generated in Fig. 4.21(f) except the APS trend related to topography. All the three datasets can hardly capture local atmospheric components. The residual phase after each correction provides more information for the assessment. As it can be seen from Fig. 4.21(c), a considerable trend has been removed from the original interferogram, but a slight trend along West-East and a comparative large residual phase in the North coastline still exist. Compared to ERA-Interim correction, a more apparent West-East residual trend can be seen from the ERA5 residual phase Fig. 4.21(e). Among the three residual phases, MERRA2 shows the best APS correction. It can be seen in Fig. 4.21(g) that the residual phase is consistent over the entire image. Unfortunately, it seems that the three global weather forecast datasets are unable to simulate and compensate localized atmospheric artifacts. As the blue clusters are still noticeable among the three residual phase figures.

In order to evaluate the goodness of the correction performance on the case study that can be achieved for other interferograms, statistical analyses are carried out to all the eight interferograms by evaluating its phase deviation. Overall, as it can be seen in Table 4.7 the phase SD is reduced for all the interferograms by all the ERA-Interim, ERA5 and MERRA2 data, with no exception. Among them the MERRA2 data achieves the best performance, with an average reduction of 43.8% for the eight pairs. Regarding the ECMWF family datasets, the latest ERA5 is continuing to perform better, having an average SD reduction of 37.9%, compared to 29.9% for ERA-Interim. But for 2 (Ifg3 and Ifg8) out of 8 cases, the ERA5 has a slight worse performance than ERA-Interim. For the specific case study (Ifg8), the phase variance is decreased by 45%, 28% and 48% for ERA-Interim, ERA5 and MERRA2 respectively, which agrees the visual analyses discussed in Fig. 4.21.

Table 4.7: Statistical comparison using D-LOS mitigation method with different GAM data for 8 Sentinel-1 interferograms in Crete, Greece. Values in parentheses are correction percentage (Original-Residual)/Original.

Ifg.	Interferogram pair	Phase SD	SD residual		
		Original	ERA-Interim	ERA5	MERRA2
Ifg1	20170424-20170506	5.12	2.46 (52%)	1.31 (74%)	2.18 (57%)
Ifg2	20170506-20170611	4.20	3.63 (14%)	2.08 (50%)	2.48 (41%)
Ifg3	20170611-20170729	4.04	3.13 (23%)	3.43 (15%)	2.11 (48%)
Ifg4	20170717-20170822	5.14	4.60 (11%)	4.33 (16%)	3.95 (23%)
Ifg5	20170822-20170903	4.66	4.04 (13%)	3.12 (33%)	3.11 (33%)
Ifg6	20170927-20171009	4.80	3.09 (36%)	2.89 (40%)	2.56 (47%)
Ifg7	20171021-20171102	5.63	3.10 (45%)	3.01 (47%)	2.65 (53%)
Ifg8	20171126-20171208	2.88	1.57 (45%)	2.07 (28%)	1.50 (48%)
Mean			(29.9%)	(37.9%)	(43.8%)

From the above discussion for Crete, Greece test site, it can be concluded that the MERRA2 data provides more benefit for APS compensation than the ECMWF family

datasets (ERA-Interim and ERA5). The ERA5 data shows better results than ERA-Interim in statistic, even though in few situations, the ERA-Interim exhibits its advantage.

4.7 Summary

In this Chapter, a realistic calculation strategy based on the ERA5 atmospheric reanalysis data has been implemented to mitigate atmospheric artifacts for InSAR. Compared to the conventional Z-LOS method, the advanced D-LOS approach calculates the tropospheric delay along the real LOS path rather than an approximation. Detailed comparison analyses between the two methods have been carried out over Tenerife, Crete and Almería with Sentinel-1 data. The advanced D-LOS method in all the three test sites demonstrates its robustness and better performance than the Z-LOS method.

Overall, the realistic D-LOS method outperforms the Z-LOS method in all the three test sites. On the one hand from the statistical point of view for all the interferograms, D-LOS approach presents more significant variance reduction than does using the Z-LOS method. In Tenerife island, D-LOS can achieve 23-77% SD reduction for twelve interferograms with an average level of 50%, while Z-LOS achieved only 14-71% and an average decrease of 37%. In Crete, Greece site, after applying D-LOS correction, the SD decreased around 15-74%, with an average reduction of 38%, compared with 5-48% and corresponding average level of 22% for the Z-LOS method for eight interferograms. Over Almería, the Z-LOS method achieved a SD reduction of 14% on average, while the D-LOS strategy showed a better performance, reaching a 29% on average for twelve interferograms. On the other hand, D-LOS approach succeeds to mitigating atmospheric artifacts in some specific interferograms where SD of residual phases even increases with Z-LOS approach.

It is noted that both Z-LOS and D-LOS strategies can remove long-wavelength tropospheric delays partially. Consequently, SD reductions can be seen with the both methods for most interferograms. Moreover, D-LOS approach demonstrates its robustness in correcting atmospheric artifacts in some localized areas (e.g. areas with high-elevation and/or surface heterogeneity) where Z-LOS method fails. This merit has been proved by exhibiting more SD reductions after D-LOS correction than Z-LOS method.

After the comparison analyses of the Z-LOS and D-LOS algorithm, the D-LOS method is further applied to different global reanalysis datasets, ERA-Interim, MERRA2, for correcting APS in the same three test sites. In general, all the three datasets have shown the feasibility to correct atmospheric artifacts partially. Among them, the latest ERA5 data from the ECMWF family is the robustest, especially compared to the last generation of ERA-Interim data. In the Tenerife and Almería test sites, statistical analyses show a better performance of ERA5 data compared to ERA-Interim and MERRA2 data. In the Crete site, MERRA2 demonstrates the best correction in terms of the average SD reduction on the eight interferograms. While in this case for most interferograms, the difference between ERA5 and MERRA2 is not significant. From our test, it seems that the MERRA2 data may not provide a stable APS compensation. Because it provides the worst correction in Almería and a moderate correction in Tenerife. By contrast, the ERA5 data is more reliable.

The APS correction technique based on GAM data can be applied to all weather conditions globally without any empirical model assumption. With the development of GAM, on account of its global coverage, both high temporal and spatial resolution and more accurate atmospheric parameters, the compensation method is very promising for near real-time InSAR applications.

As atmospheric artifacts from differential interferograms are in great agreement with APS from atmospheric reanalysis data, it demonstrates a potential ability to study atmospheric dynamic using InSAR. On the one hand, it is possible to retrieve atmospheric water vapour mapping from differential interferograms. Compared with GPS data, InSAR is a promising technique to retrieve water vapour product with global coverage and higher resolution. On the other hand, InSAR technique can also provide potential enrichment of datasets used for research using numerical weather models, especially in very localized areas for turbulent atmosphere research. Even now, the latest suite of numerical weather prediction models have difficulty in accurately predicting meso- and micro-scale atmospheric dynamics, due mainly to computational discretization and observational scarcity. It is believed that atmospheric delays from InSAR can provide a promising observation dataset for weather data assimilation.

5

Chapter 5

Tropospheric delay mitigation using local numerical weather prediction models

In Chapter 4 reanalysis datasets from global numerical models have been used to mitigate APS in interferograms. Its feasibility has been demonstrated with different case studies, in which for most of the interferograms the original APS was dramatically reduced. However, due to the relative large scale in time and space of global reanalysis data, some strong and localized APS cannot be retrieved correctly. In this Chapter, local numerical models will be exploited to correct atmospheric phase delays from interferograms. Compared to global reanalysis data, owing to the relative higher spatial and temporal resolution of local numerical models, it can be expected they have better capacity to mitigate local atmospheric artifacts. The main contents in this Chapter focus on runing the local numerical WRF model, APS estimation based on the WRF output, and mitigation from interferograms, as well as results comparison with GAM data. An introduction of APS mitigation using local numerical weather models is provided in Section 5.1. Section 5.2 describes details of local numerical weather models, particular the WRF model and its setups. In Section 5.3, the D-LOS calculation method is applied to the WRF output to correct APS. Moreover, the correction performance is discussed by setting different resolution domains in the WRF model. Finally, its performance is also evaluated by comparing the results to the ones from the ERA5 data in Section 5.3.

5.1 Introduction

Atmospheric artifacts can be estimated from weather forecast data. The detailed calculation procedures of the D-LOS method based on global numerical models have been given in Chapter 4. It has demonstrated its feasibility to correct APS, especially for stratified atmospheric artifacts component in large scale areas. However, global reanalysis datasets from the ECMWF, NCEP or others have a relative large scale in spatial and temporal domain. As a consequence, they may make the correction unreliable for local atmospheric artifacts in high spatial resolution interferograms. Compared to global forecast models, local numerical models have the possibility to solve the low resolution problem. As it indicates in reference [111] that regional models, the WRF for example, can predict finer atmosphere parameters from continental to regional scale with resolutions from hundreds of kilometers down to below a kilometer, and can also simulate the atmosphere at the acquisition times of SAR images. Several studies for APS mitigation based on regional numerical models are available in the literature. The reference [40] explores atmospheric noise mitigation based on the NCAR-Penn State Mesoscale Model Version 5 (MM5) weather model. Its application over Hawaii shows variance reduction at wavelengths of 30 km. In the literature [117], authors present a Medium Resolution Imaging Spectrometer (MERIS) and MM5 combined method to recover atmospheric artifacts in Mount Lebanon nearby the Mediterranean Sea, showing promising results. With the WRF, the up-to-date local numerical model, more encouraging compensation results have been presented in references [21, 110, 118, 119]. From all the available experiments and results in the literature, it has been proved that the local numerical weather forecast models work in some case studies. However, the performance of regional weather models is essentially dependent on the initial constrains and model physics parameters settings, etc. In some complex situations, the numerical weather models may fail to simulate atmospheric artifacts. The authors in reference [120] found that in the study area around Mount St. Helens, USA, the MM5 model is unable to model the refractive changes and provides no mean benefit for mitigating APS in interferograms. Fortunately, due to the development in weather forecast modeling research area, including a wide range of data sources, more satellites atmosphere measuring, GPS stations, etc., the more accurate and spatially dense meteorological data can improve the performance of weather forecast modelling. For example, using the latest global reanalysis ERA5 data as initial conditions, the latest WRF model has the potential to improve the weather parameters predictions in contrast to using the MM5 model based on relative outdated reanalysis data such as ERA-Interim.

In this Chapter, we have extended APS estimation and compensation for interferograms based on the latest WRF model. On the one hand, the latest global reanalysis ERA5 data is used as initial atmosphere state for running the local WRF model. On the other hand, different physics parameters setups, including resolutions, land surface and the way of nesting domains, in the WRF model running are tested and discussed. Moreover, the more accurate D-LOS APS calculation is used rather than the Z-LOS method. The schematic diagram of using local numerical models to compensate APS is shown in Fig. 5.1, which is composed of three main blocks, i.e. collecting observation data as input, local model running and APS simulation and compensation in interferograms.

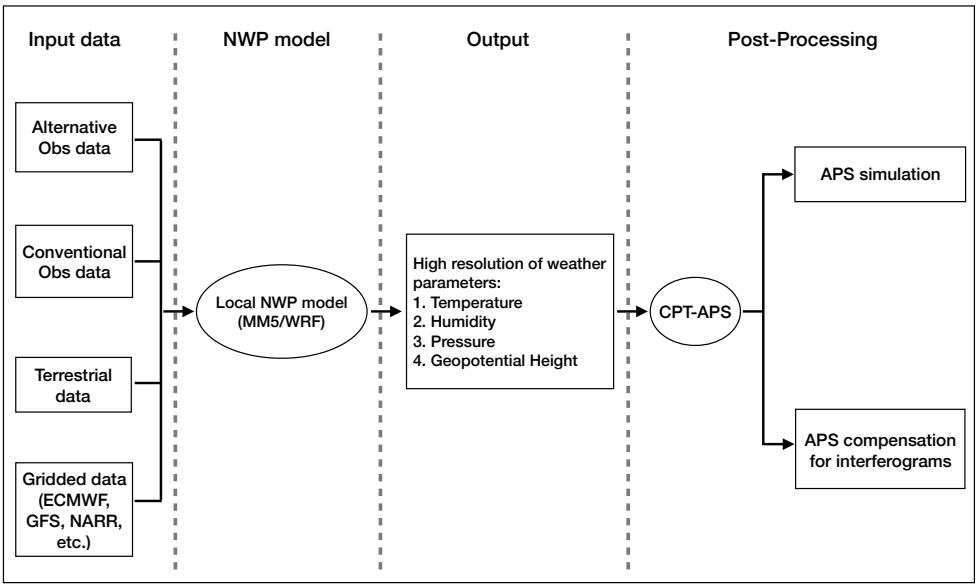

Fig. 5.1. Diagram of local NWP model for high resolution weather parameters simulation and APS compensation for interferograms.

5.2 Local numerical weather prediction models

Numerical weather models use mathematical models constructed with primitive dynamical equations based on current weather conditions to produce meteorological information for future time at given locations. In principle, it can solve these equations with parameterizations for soil, vegetation, surface water, turbulent diffusion, convection, etc. With all the parameters solved, the atmospheric models then can predict microscale atmosphere phenomena such as tornadoes, turbulent flow over buildings, synoptic and global flows. NWP models began in the 1920s by Lewis Fry Richardson [121]. It was not until the advent of the computer in 1950 that numerical calculation promoted its development to practical use. Nowadays more powerful computers are able to handle with more complicated equations and increase the size of initial datasets. As a result, weather prediction is more accurate and reliable. The principle of numerical weather prediction is based on the fluid of atmosphere. Numerical weather models take advantage of the current state of atmosphere at a given time and use the equations of fluid dynamics and thermodynamics to predict the atmosphere conditions at some time in the future. In order to do so, initial atmosphere state as constrains and a certain dynamical model are compulsory. To determine the initial atmosphere conditions, a wide variety of methods are used to gather observational atmosphere data such as radiosondes, weather satellites, pilot reports along aircraft routes, ship reports, weather stations at ground level as well as buoys at sea. After gathering all the observations, the irregularly spaced data are processed by data assimilation to obtain regular values usable by model mathematical algorithms. The numerical weather models then handle regular atmosphere parameters as inputs to produce high spatial and temporal resolution weather parameters in three dimensions.

From the scale point of view, a numerical weather model can be either a global, covering the continent, or a local one, covering only the interested area. Atmospheric models, in general, work on horizontal domain and vertical domain. Global models usually use spectral methods for the horizontal domain and finite-difference methods for the vertical dimension, while regional ones often use finite-difference methods in all the three dimensions. Regional models use finer grid spacing to resolve explicitly smaller-scale meteorological phenomena, since their smaller domain decreases computational demands. Normally regional models use a compatible global model for initial conditions of the edge. By now, many agencies, institutes and universities around the world have developed a variety of numerical weather prediction models appropriate to different applications. A list of these models is summarized in Table 5.1. Among them, some of the well known global numerical models include Global Forecast System (GFS) developed by the National Oceanic and Atmospheric Administration (NOAA) and IFS developed by the ECMWF. The well known regional numerical models contain MM5 and WRF developed by the NCEP, NCAR. For the purpose of compensating APS in interferograms, indispensable outputs from the local weather models are temperature, geopotential height, pressure as well as humidity.

Table 5.1: Comparison of different numerical weather prediction models.

Model	Agency	Coverage	Resolution
GFS	NOAA	Global	up to 28 km
IFS	ECMWF	Global	up to 9 km
NOGAPS	US Navy	Global	0.5° (50 km)
GEM	Meterorological Service of Canada	Global	up to 24 km
UM	UK Met Office	Global	up to 4.4 km
ICON	German Weather Service	Global	up to 6.5 km in Europe
WRF	NCEP, NCAR	Regional	under 1 km
NAM	NCEP	Regional	12 km in North America
RAMS	Colorado State University	Regional	under 1 km
MM5	Penn State University, NCAR	Regional	up to tens of meters
ARPS	University of Oklahoma	Regional	up to the tornado-scale
GEM-LAM	Meterorological Service of Canada	Regional	up to 2.5 km

5.2.1 WRF

The WRF model is the next-generation mesoscale numerical weather prediction system designed for both atmospheric research and operational forecasting applications. Based on actual atmospheric observations, WRF can produce simulations by taking advantage of physics, numerics and data assimilation. WRF can be used in a wide range of applications, such as meteorological studies, idealized simulations, data assimilations, across scales ranging from tens of meters to thousands of kilometers. The WRF system contains two dynamical cores, the Advanced Research WRF (ARW) core and the Nonhydrostatic Mesoscale Model (NMM) core. The ARW has been developed and maintained by NCAR's Mesoscale and Misroscale Meteorology Laboratory. The NMM core was developed by the National Centers for environment prediction, and is currently used in their hurricane WRF

system. The ARW core is more suitable for our study to produce desired atmospheric parameters.

One important input for the WRF system is a global atmosphere data with a relative coarse spatial and temporal resolution as an initial. After a series of complicated processing steps, the WRF model can produce atmosphere parameters at a higher resolution. Fig. 5.2 shows one example of using the WRF model to improve the resolution. Fig. 5.2(a) and Fig. 5.2(b) are the temperature of the first layer (from bottom to top) of 31 *km* ERA5 data at 18:00:00, 19:00:00 UTC time on 31 October 2017, respectively. Fig. 5.2(c) is the corresponding temperature predicted by the 5 *km* WRF model at 18:10:00 UTC.

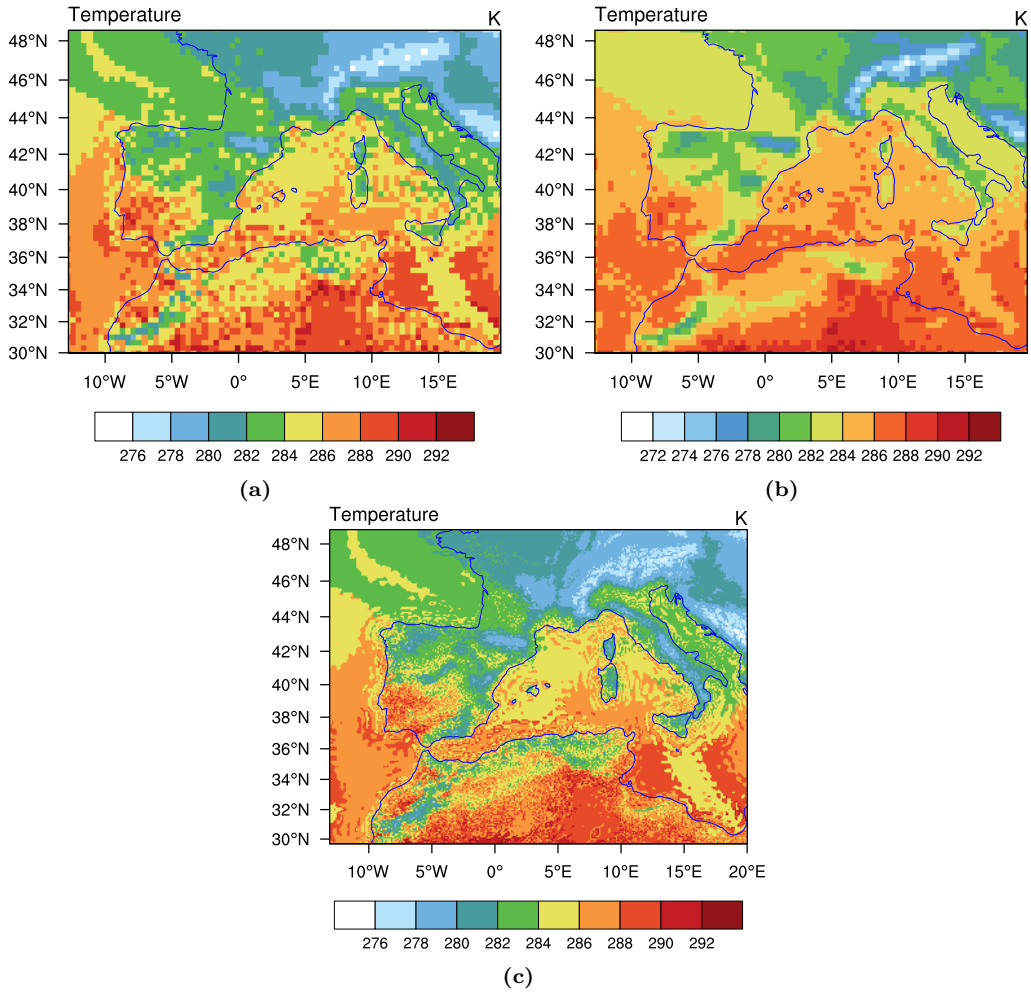

Fig. 5.2. Comparison of temperature between ERA5 and the WRF prediction in the Mediterranean region. (a) The 31 *km* resolution of temperature (the bottom layer) from the ERA5 model level data at 18:00:00 UTC time on 31 October, 2017. (b) The same temperature data as (a), but from the ERA5 at 19:00:00 UTC time. (c) The predicted temperature from 5 *km* resolution WRF model at 18:10:00 UTC.

5.2.1.1 WRF model scheme

The flow chart (Fig. 5.3) shows how does the WRF system generate finer atmosphere parameters. It consists of the WRF Preprocessing System (WPS) and ARW module. The WPS module is mainly used for preparing data for real data simulation. The preparation includes defining simulation domains, interpolating terrestrial data (such as terrain, land use, and soil types) to the simulation domain, describing and interpolating meteorological data from external source to the simulation domain. The ARW module is composed of several initialization programs for idealized, real-data simulations, and the numerical integration program. Several basic features related the WPS and ARW module will be explained in the following part. It can be very easy for experts in the weather forecast community, but probably not so simple for the InSAR community.

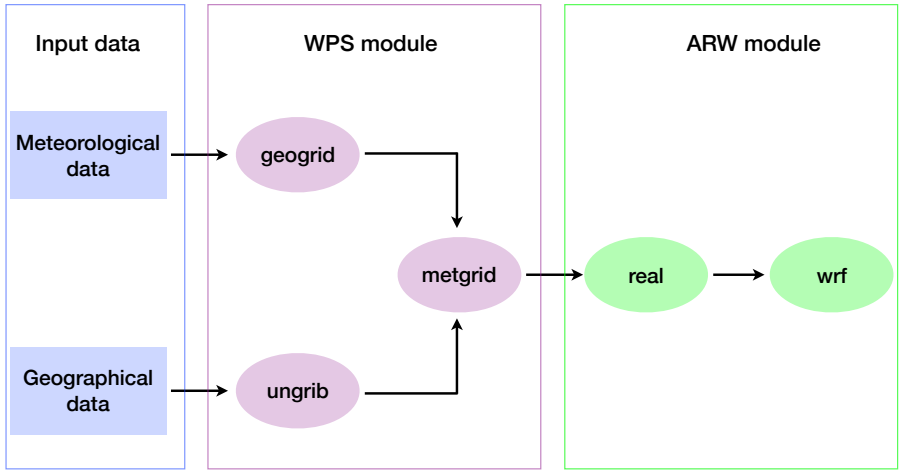

Fig. 5.3. The flow chart of the WRF model, which is mainly composed of the WPS and ARW module.

The WPS consists of three programs (geogrid, ungrib and metgrid) whose functions are to prepare input data for the ARW model to do real-data simulations. All the three programs read parameters from a common file named namelist.wps, in which the record for each of the programs is separated. The functions of the three programs are listed as follows.

- geogrid: The geogrid program defines model domains and interpolates static geographical data to the grids. The required parameters determining the model domains can be read from the above mentioned namelist.wps file. With these parameters, the geogrid program will compute the latitude, longitude and map scale factors at each grid point. Additionally the geogrid will integrate varieties of static geographical data, such as soil categories, terrain height, land use category, vegetation fraction. The static geographical data are available in different resolutions and can be downloaded from the WRF users page (http://www2.mmm.ucar.

edu/wrf/users/download/get_sources_wps_geog.html). Generally a resolution of the data near to that of the simulation domain is preferred for integration processing. The fields and interpolation methods are described in a table file called GEOGRID.TBL. To run the WRF model successfully, several mandatory fields are required. Meanwhile some static data are optional for specific applications. For the purpose of APS mitigation, the mandatory fields are based on the description in the WRF website (http://www2.mmm.ucar.edu/wrf/users/download/get_sources_wps_geog.html). It is also briefly described in Table 5.2.

- ungrib: The ungrib program extracts meteorological fields in GRIB-formatted files, provided by a global or regional model, and writes these fields into an intermediate file. GRIB files from other models typically contain more fields than that needed to initialize the WRF model, so the ungrib uses a table called Vtables to define the desired fields. The WRF package provides the most common used Vtables, including variable tables for NCEP/NCAR, GFS, ECMWF, etc. Users can also create their own Vtable for other models by using any of the provided Vtables as a template.

- metgrid: The metgrid horizontally interpolates the intermediate-format data produced by the ungrib program onto the simulation domains defined by the geogrid program. Outputs from the metgrid program are used as inputs to the ARW program. Parameters controlling the interpolation procedure, such as interpolation method for each individual field, are provided in the METGRID.TBL file.

The above three steps are essential to run the WPS module and provide input data for the following ARW module. The ARW is composed of two main programs: real and wrf module. The real is mainly used to interpolate the data to the model coordinates vertically, which is called WRF initialization. And the wrf program is used to generate the model forecast products.

- real: Actually, there are two large classes of simulations in the WRF model. One is for ideal initialization situation and the other is for utilizing real data to generate real WRF initialization. In this thesis, we only focus on the real initialization situations. By the way, the WPS processing is necessary for the real data cases but not for the ideal situations. Based on the horizontally interpolated output data from the WPS, the purpose of the real program is to build initialization data for the wrf program. The detailed steps include computing a base reference profile for geopotential and column pressure, initializing meteorological variable, defining a vertical coordinate and interpolating data to the model's vertical coordinate.

- wrf: The core of the WRF model is the wrf module, which is essentially a numerical integration program. Its vertical coordinate is either a terrain-following or hybrid vertical hydrostatic pressure coordinate. Regarding the time integration, the model uses the Runge-Kutta 2nd and 3rd order integration scheme. And in spatial discretization, 2nd to 6th order advection schemes are used in both the horizontal and vertical coordinate.

5.2.1.2 WRF model setup

All the above described programs are basic and essential for a real-data simulation. Moreover, a successful run of the WRF model should build on correct parameter settings. In this Section, required meteorological fields for running real-data cases are described. Besides two important controlling files, i.e., the namelist.wps for the WPS and the namelist.input for the ARW module, are explicitly explained.

In the WRF system, static parameters, such as soil type, vegetation type, and soil moisture, all determine how much radiation goes into warming and how much moisture is drawn up into the adjacent atmosphere. Thus, they are important to parameterize. For running the WPS module, several static geographical data are compulsory, which are listed in Table 5.2.

Table 5.2: Compulsory static geographical data for the WRF model.

Static data	Sources	Resolution
Albedo	Modis	-
Green Fraction	Modis	-
Fraction of Photosynthetically Active Radiation	Modis	-
Leaf Area Index	Modis	30 arc sec
Maximum Snow Albedo	Modis	-
Landuse (20 class)	Modis	30 arc sec
Orographic gravity wave drag	-	10 arc min
Soil temperature	-	1 arc deg
Soil type (top)	-	30 arc sec
Soil type (bottom)	-	30 arc sec
Global Multi-resolution Terrain Elevation Data 2010	-	30 arc sec
variance of sub-grid-scale orogoraphy	-	2 arc min

By using the above static data, the WPS module can generate intermediate data as input for the ARW program. In order to initialize a real-data simulation successfully, the real.exe program in the ARW module requires a minimum set of meteorological variables, which are described in Table 5.3.

Once having the compulsory static data for the WPS module and required fields for running the ARW, users should be also familiar with two important controlling files: the namelist.wps and namelist.input. The WPS and ARW programs read all the required parameters, such as simulation time, domains, from the two files. As mentioned in previous sections, the WRF model can be used for a variety of applications. Hence, a lot of parameters are involved for different applications. In this thesis, for the purpose of mitigating APS from interferograms, the following parameters have to be considered.

Regarding the namelist.wps file related to parameters for the WPS block, there are four records in it, i.e., “share”, “geogrid”, “ungrib” and “metgrid”. First of all, in the share part, the core of the WRF has to be set and in our cases the ARW core is selected. And then, the coarse domain and any nested domains are defined in the “geogrid” record. The parameters in the “ungrib” and “metgrid” record can use the default ones. A detailed description of each variable is given in Table 5.4.

Table 5.3: Required fields for the ARW programs.

Parameters	Field name in intermediate file	Units
Air temperature	TT	K
Relative humidity	RH	%
Specific humidity	SPECHUMD	kg/kg
Wind u-component	UU	m/s
Wind v-component	VV	m/s
Geopotential height	GHT	m
Pressure	PRESSURE	Pa
Surface pressure	PSFC	Pa
Mean sea-level pressure	PMSL	Pa
Skin temperature	SKINTEMP	K
Soil height	SOILHGT	m
Land-sea mask	LANDSEA	$fraction$
Soil moisture	SM	m^3/m^3
Soil temperature	ST	K

Table 5.4: Description of variables in the WPS namelist file.

Variables	Description
&share record	
max_dom	An integer specifying the total number of domains
start_date	Specifying the starting UTC date
end_date	Specifying the ending UTC date
interval_seconds	An integer number specifying the time interval of input meteorological data in seconds
&geogrid record	
e_we	An integer specifying the west-east dimension
e_sn	An integer specifying the south-north dimension
dx	The grid distance in the x direction
dy	The grid distance in the y direction
map_proj	A character string specifying the projection. It can be "lambert", "polar", "mercator", "lat-lon". In this thesis, "mercator" projection is used.
ref_lat	The latitude of the center point of the coarse domain
ref_lon	The longitude of the center point of the coarse domain
geog_data_path	A character string specifying the path of static geographical data

The variables in Table 5.4 are required for running the WPS module and other variables not mentioned in this table can be kept as default in the namelist.wps file. It is also interesting to mention that the simulated region is determined by several variables, which is shown in Fig. 5.4.

In terms of the namelist.input file for the ARW module, first of all, some variables for controlling dimensions and resolutions of the domains should match those in the

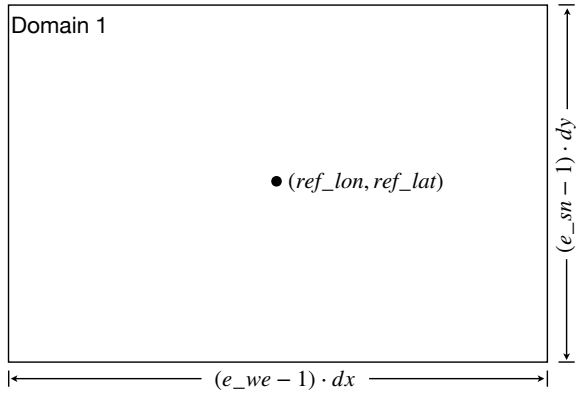

Fig. 5.4. The simulated domain of the WRF model is determined by ref_lon, ref_lat, e_we, e_sn, dx and dy setups.

namelist.wps for the WPS. Besides, other variables should be set according to real situations. Several important parameters are described in Table 5.5.

Table 5.5: Description of variables in the ARW namelist file.

Variables	Description
&time_control	
run_days	run time in days
run_hours	run time in hours
run_minutes	run time in minutes
start (end) _year	the starting (ending) year
start (end) _month	the starting (ending) month
start (end) _day	the starting (ending) day
start (end) _hour	the starting (ending) hour
start (end) _minute	the starting (ending) minute
start (end) _second	the starting (ending) second
interval_seconds	It must match the interval seconds from namelist.wps file.
history_interval	history output file interval in minutes
& domains	
p_top_requested	pressure of the top layer to use in the model
num_metgrid_levels	number of vertical levels in WPS output
num_metgrid_soil_levels	number of soil levels in WPS output

The WRF model can run in multiple domains. In both the namelist.wps and the namelist.input file, variables for one coarse domain and nested domains can be set in multiple columns. If only one domain is used, entries in the first column will be used and entries in other columns will be ignored.

5.3 APS correction based on the WRF model

The above sections have elaborately explained what is the WRF model and its setups for APS mitigation purpose. In this Section, the implementation of using the WRF output to mitigate APS from interferograms has been carried out. As discussed in Chapter 4, the accurate D-LOS method outperforms the conventional Z-LOS method, in this Chapter, the realistic D-LOS algorithm will be utilized based on the local numerical weather forecast WRF model.

To demonstrate the feasibility of using the WRF model to mitigate APS, the global ERA5 data will be used as initial conditions for running the WRF model for example. As commented in Chapter 4, ERA5 is the latest version of ECMWF reanalysis data. Unlike using the pressure level data in Chapter 4, for running the WRF, it is necessary to utilize the model levels and surface level data. ERA5 model levels data was produced using 4D-Var data assimilation in CY41R2 of ECMWF's IFS, with 137 hybrid pressure levels in the vertical direction, with the top level at 0.01 hPa. The ERA5 dataset contains one high resolution (31 km) realisation (HRES) and a reduced resolution ten member ensemble (EDA). In this thesis, the hourly available HRES data is used. In terms of the test sites, two regions (Tenerife, Spain, Almería, Spain) are chosen for demonstrating the generality.

5.3.1 Evaluation in Tenerife, Spain

Tenerife island is located in the Atlantic Ocean. It enjoys a warm tropical climate that is controlled to a great extent by the trade winds. Its humidity is condensed principally over the north and northeast of the island, creating cloud banks that range between 600 and 1,800 m in height. As shown in Chapter 4, many interferograms covering this island are contaminated by atmospheric artifacts. To evaluate the correction performance of using the WRF model, 12 interferograms with short temporal and spatial baselines covering one entire year have been studied. These interferograms are the same as the ones in Chapter 4.

To run the WRF model, the most two closest hourly ERA5 data (model levels and surface level) to SAR acquisitions are used to initialize the conditions. In Tenerife case, as the Sentinel-1 SAR images are acquired at 07:02 UTC time, the ERA5 data at 07:00 and 08:00 UTC are taken as input. As mentioned earlier, the WRF model is able to generate high spatial resolution simulations for atmospheric fields at the SAR images acquisition time. Meanwhile, it also has a multiple nest capability to deal with both large scale effects from a coarse resolution domain and local effects from a finer resolution domain. In Tenerife, on the one hand, in the spatial domain, three nested domains with horizontal resolution of 27, 9 and 3 km are set respectively. As it is found in [122] that, a two-way grid nesting is generally superior to one-way nesting, the two-way nesting method with one input file is chosen in the WRF model. The simulated area is also controlled by the "e_we" and "w_sn" parameters, corresponding to grids size. For the three domains, we defined their grids size as 148x121, 103x103, 103x103, respectively. On the other hand, in the time domain, 10 min history interval is set to generate the WRF forecast output. Consequently, the atmospheric profile at 07:00, which is closer to the SAR acquisition time (07:02), is used to calculate the APS delays.

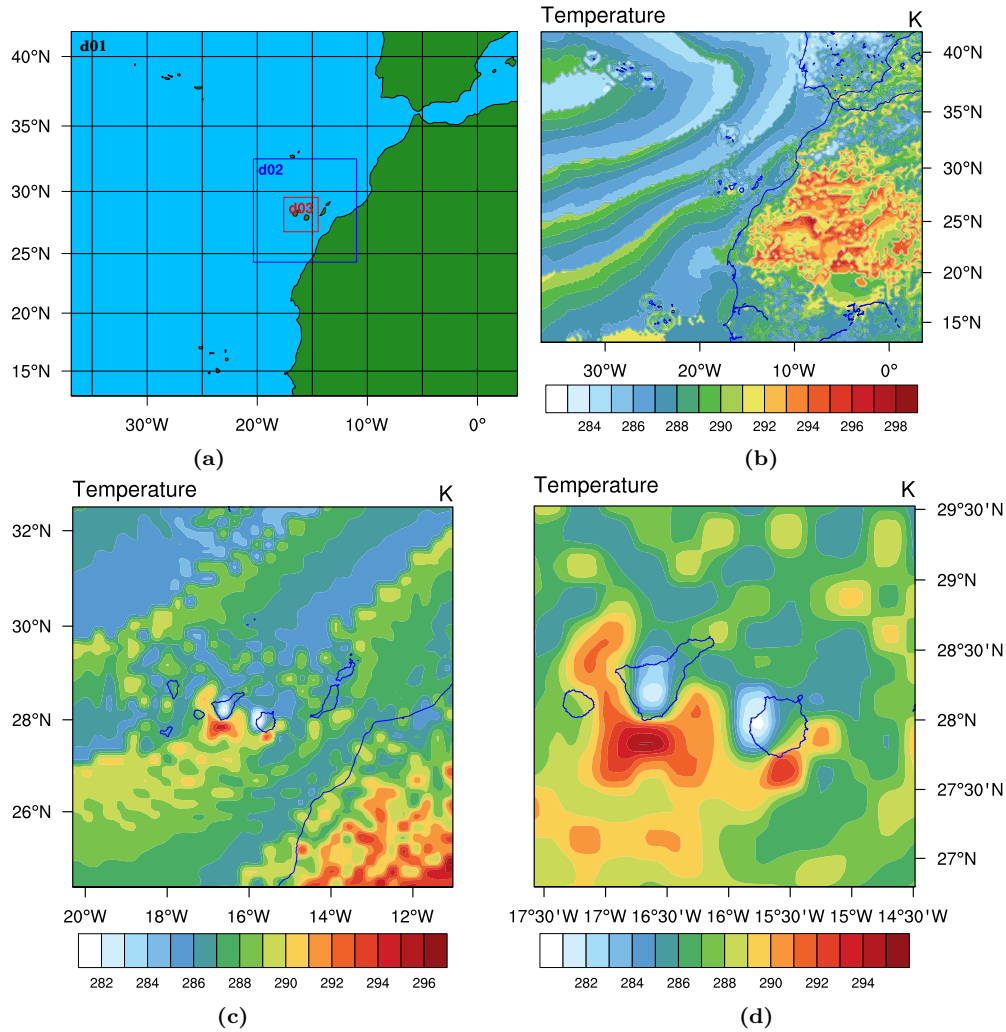

Fig. 5.5. Illustration of temperature for the three WRF domains results on 21 July 2016. (a) Three WRF domains configuration. (b) The first layer (from bottom to top) of temperature for the first domain (27 *km* resolution). (c) The temperature for the second domain (9 *km* resolution). (d) The temperature for the third domain (3 *km* resolution).

In order to illustrate multiple domains simulation results, the ERA5 data on 21 July 2016 is used as an example to demonstrate it. The multiple domains results are visualized in Fig. 5.5, in which Fig. 5.5(a) represents the three WRF domains configuration, Fig. 5.5(b) shows the temperature of the first layer (from bottom to top) for WRF 27 *km* resolution domain (d01), Fig. 5.5(c) shows the corresponding temperature parameter for the 9 *km* resolution domain (d02), and Fig. 5.5(d) displays the 3 *km* domain result (d03).

For the demonstration of APS compensation in interferograms, the interferogram 20160721-20160814 (Ifg11) is chosen as a case study, and the other 11 interferograms

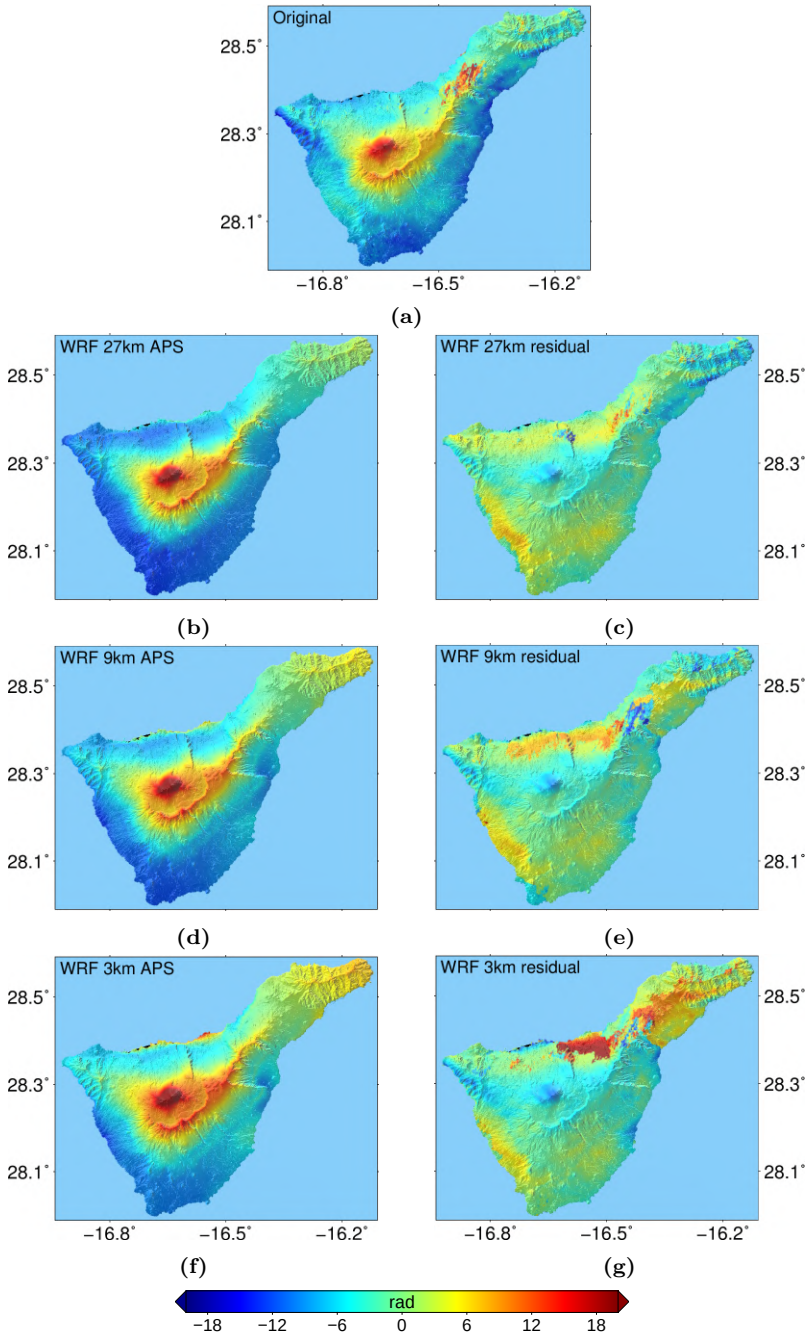

Fig. 5.6. 20160721-20160814 (Ifg11) case study of APS compensation over Tenerife using WRF model with different resolutions. (a) original interferogram. (b-c) D-LOS predicted APS and residual phase with 27 *km* WRF. (d-e) D-LOS predicted APS and residual phase with 9 *km* WRF. (f-g) D-LOS predicted APS and residual phase with 3 *km* WRF.

will be statistically analysed. It is expected that the WRF model will have a better performance than using the original ERA5 data, due to the higher spatial resolution as well as the closer atmospheric parameters to the SAR acquisition time. However, the cases in Tenerife just show the opposite results.

On the one hand, in terms of the case study (Ifg11), the correction results using the WRF model with different resolutions are shown in Fig. 5.6, in which Fig. 5.6(a) shows the original interferogram, Fig. 5.6(b), Fig. 5.6(d) and Fig. 5.6(f) presents the simulated APS for 27 km, 9 km and 3 km domain respectively, and the subfigure Fig. 5.6(c), Fig. 5.6(e) and Fig. 5.6(g) exhibits the corresponding residual phases after each correction. From the large scale point of view, the simulated APS from three different resolutions WRF model shows a similar pattern with atmospheric artifacts in the original interferogram. As a result, the main atmospheric artifacts correlated with topography can be mitigated to some extent. It can also be seen from the residual phases, the phase dispersion has been reduced. Meanwhile, if we pay attention to the local scale, the increasing of spatial resolution in running the WRF model does not show any improvement for the APS correction. Just on the contrary, as the resolution increases, the worse mitigating performance can be seen in this case, especially in the north part of the island. To be more specific, compared with the 27 km WRF model result, the 9 km residual phase represents big phase dispersion along the north coastline. Moreover, the 3 km WRF model performs even worse than the 9 km model. Because it is apparent that in the 3 km residual phase, the phase dispersion extends from the north coastline to the North-East part of the island. Besides, the SD assessment on this case study further proves the above discussion. The 27 km, 9 km and 3 km WRF model can reduce the SD from 6.79 rad to 2.59, 2.90 and 3.68 rad, respectively, which is corresponding to 62%, 57% and 46% reduction.

On the other hand, the statistical analysis is applied to all the 12 interferograms in Tenerife. It can be seen from the statistical results in Table 5.6 that in most cases the WRF model has the ability to remove APS to some extent, on account of the phase SD reduction. In the WRF internal comparison, the 27 km WRF model shows the best mitigation performance, while the 3 km model presents the worst results. On average, the WRF model with 27 km, 9 km and 3km resolution shows 44%, 38% and 32% SD reduction respectively. It is also noticed that for the Ifg5 case, the WRF model with different resolutions even deteriorates the original interferogram. If the best WRF results (27 km WRF) are compared to the results from the ERA5 reanalysis data, the statistical analyses in Table 5.6 show that the time consuming WRF model even performs worse than the global reanalysis data in term of the average SD reduction.

5.3.2 Evaluation in Almería, Spain

As it is shortly described in Section 4.2.3, interferograms covering Almería region, in the southeast of Spain, suffer atmospheric artifacts contamination. Consequently, applying InSAR techniques in this region to retrieve subsidence without correcting APS may result in unreliable estimation. In this Section, the D-LOS integration method based on the WRF model data is used to compensate the APS in Almería.

In Almería, the WRF model is conducting similarly with the one in Tenerife. As it is can be seen in the Tenerife case, the difference between different WRF resolutions is

Table 5.6: Statistical comparison using the WRF model with different resolutions for 12 Sentinel-1 interferograms in the Tenerife island. Values in parentheses are correction percentage (Original-Residual)/Original.

Ifg.	Interferogram pair	SD	SD residual			
		Ifg.	ERA5	27km WRF	9km WRF	3km WRF
Ifg1	20150925-20151007	5.32	1.94 (64%)	1.77 (67%)	2.26 (58%)	3.03 (43%)
Ifg2	20151007-20151112	5.66	2.54 (55%)	3.06 (46%)	5.18 (8%)	5.44 (4%)
Ifg3	20151112-20151218	4.59	1.65 (64%)	2.27 (51%)	2.36 (49%)	2.50 (46%)
Ifg4	20151206-20160111	5.99	1.40 (77%)	2.22 (63%)	2.36 (61%)	2.51 (58%)
Ifg5	20160123-20160204	4.23	2.75 (35%)	5.24 (-)	5.61 (-)	5.91 (-)
Ifg6	20160228-20160311	4.15	2.14 (48%)	1.96 (53%)	2.34 (44%)	2.77 (33%)
Ifg7	20160311-20160416	3.74	2.04 (45%)	3.64 (3%)	3.12 (17%)	3.68 (2%)
Ifg8	20160404-20160510	4.01	2.47 (38%)	2.54 (37%)	2.95 (26%)	2.98 (26%)
Ifg9	20160510-20160615	2.98	2.30 (23%)	2.43 (18%)	2.45 (18%)	2.45 (18%)
Ifg10	20160615-20160709	3.46	2.37 (32%)	2.82 (18%)	2.93 (15%)	2.96 (14%)
Ifg11	20160721-20160814	6.79	2.62 (61%)	2.59 (62%)	2.90 (57%)	3.68 (46%)
Ifg12	20160826-20160907	6.62	2.64 (60%)	2.56 (61%)	2.59 (61%)	2.65 (60%)
Mean			(50%)	(44%)	(38%)	(32%)

not significant. One possible reason is that with two-way grid nesting using one input file, nested domains do not benefit from high resolution static fields [111]. Thus, in the Almería case, a two-way grid nesting with two input files is chosen in the WRF model. To be specific, in this case all static and meteorological data for the nest(s) are obtained from the original nest's input files directly, rather than from the coarse grid. Similar to the Tenerife case, the WRF model in Almería is also run in three nested domains with 10 min interval in time. In spatial domain, the grids size for the 27, 9, 3 km nested domain is defined as 111x91, 103x103, 103x103, respectively.

The predicted atmospheric parameters from the three domains WRF model are used to generate the atmospheric artifacts screen and further utilized to correct the interferograms in Almería. The compensation results for the interferogram 20171031-20171124 (Ifg 11) are shown in Fig. 5.7, in which Fig. 5.7(a) is the original interferogram, Fig. 5.7(b), Fig. 5.7(d), Fig. 5.7(f) shows the simulated APS from the 27 km, 9 km and 3 km domain respectively, and the subfigure Fig. 5.7(c), Fig. 5.7(e) and Fig. 5.7(g) presents the corresponding residual phase after each correction. In general, it can be seen visually that the three domains WRF model can remove the most part of the atmospheric artifacts, particularly for the topography related component. Meanwhile the performance of the three corrections is very similar with each other. From the statistical point of view, the 27 km WRF model can reduce the SD from 2.95 to 2.20 rad by 25% reduction, while the 9 km and 3 km model accomplishes 34% and 35% reduction respectively. It seems that from this specific case study, the higher resolution the model is, the better performance the mitigation can achieve. However, applying the statistical analysis to all the twelve interferograms, it turns out that the 27 km, 9 km and 3 km model achieves 24%, 25% and 25% SD reduction on average (see Table 5.7). It is found that the higher resolution model only achieves slightly better performance than low resolution model. Moreover, it is interesting to point out that for the Ifg8 case, the 9 km and 3 km model increases the

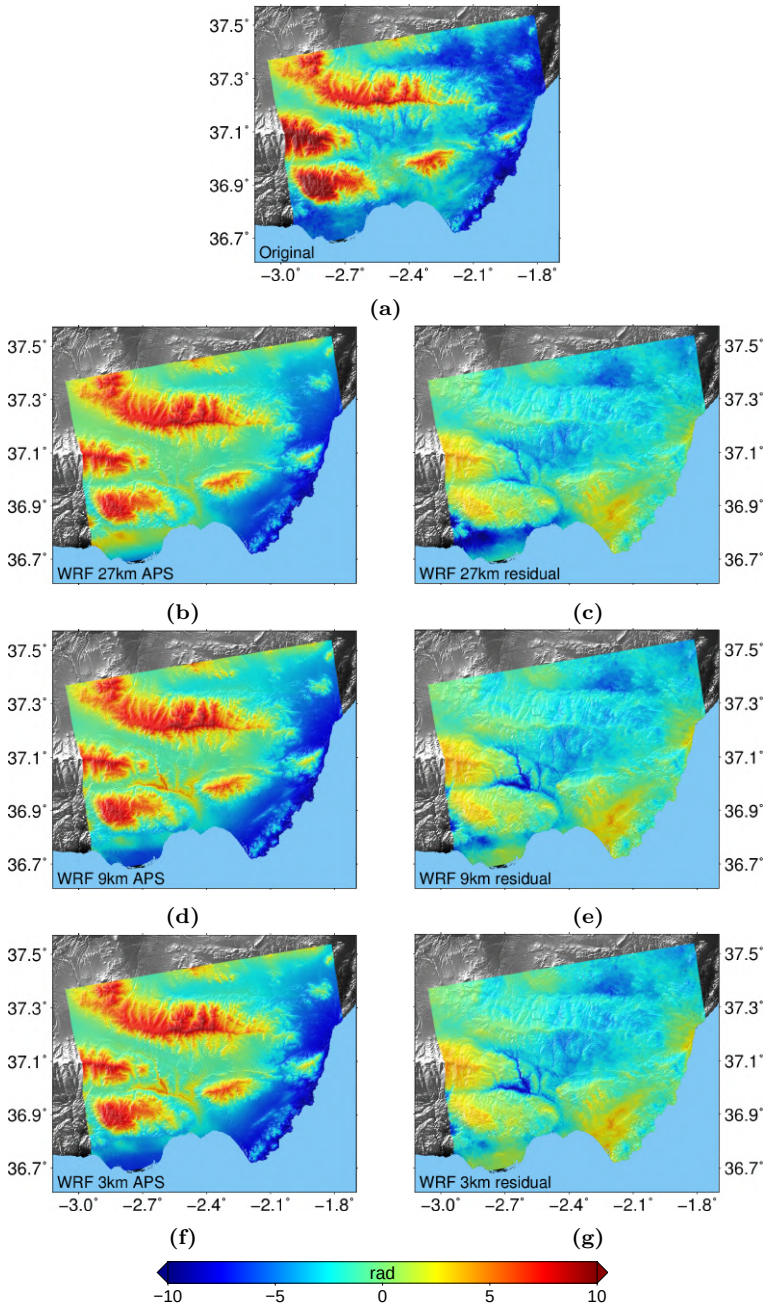

Fig. 5.7. 20171031-20171124 (Ifg11) case study of APS compensation over Almería using WRF model with different resolutions. (a) original interferogram. (b-c) D-LOS predicted APS and residual phase with 27 *km* resolution WRF. (d-e) D-LOS predicted APS and residual phase with 9 *km* resolution WRF. (f-g) D-LOS predicted APS and residual phase with 3 *km* resolution WRF.

SD rather than reduces it. Overall, the increased spatial resolution of the WRF model does not show significant improvements on correcting the atmospheric artifacts. Besides, the computational burden of running a higher resolution model is tremendous higher than a low resolution one. The comparison between results from the original ERA5 data and the ones from the WRF model also shows an agreement with the cases in Tenerife. In other words, the ERA5 data can achieve a better APS correction than the WRF model on account of the average SD reduction. With ERA5 correction, the average SD reduction can reach up to 29%, while using the WRF model, it can only achieve around 25%.

Table 5.7: Statistical comparison using the WRF model with different resolutions for 12 Sentinel-1 interferograms in Almería, Spain. Values in parentheses are correction percentage (Original-Residual)/Original.

Ifg.	Interferogram pair	SD	SD residual			
		Ifg.	ERA5	27km WRF	9km WRF	3km WRF
Ifg1	20161217-20170110	4.19	3.52 (16%)	3.51 (16%)	3.55 (15%)	3.55 (15%)
Ifg2	20170122-20170227	4.13	3.46 (16%)	3.35 (19%)	3.13 (24%)	3.10 (25%)
Ifg3	20170227-20170311	5.38	3.29 (39%)	3.26 (39%)	3.29 (39%)	3.26 (39%)
Ifg4	20170311-20170428	5.13	3.86 (25%)	2.15 (58%)	2.74 (47%)	2.46 (52%)
Ifg5	20170404-20170510	4.37	3.68 (16%)	3.41 (22%)	3.72 (15%)	3.77 (14%)
Ifg6	20170528-20170609	5.93	3.25 (45%)	2.97 (50%)	2.98 (50%)	3.00 (49%)
Ifg7	20170609-20170703	4.60	3.22 (30%)	4.00 (13%)	4.06 (12%)	4.14 (10%)
Ifg8	20170727-20170808	6.12	3.54 (42%)	5.91 (3%)	6.81 (-)	7.07 (-)
Ifg9	20170808-20170901	7.53	5.52 (27%)	6.25 (17%)	6.64 (12%)	6.66 (12%)
Ifg10	20170901-20171007	4.66	3.17 (32%)	3.35 (28%)	3.71 (20%)	3.79 (19%)
Ifg11	20171031-20171124	2.95	1.79 (39%)	2.20 (25%)	1.95 (34%)	1.92 (35%)
Ifg12	20171112-20171206	2.54	2.00 (21%)	2.48 (2%)	2.36 (7%)	2.36 (7%)
Mean			(29%)	(24%)	(25%)	(25%)

5.4 Summary

As it is concluded in the Chapter 4 that the global weather forecast data have the feasibility to correct atmospheric artifacts to some extent, but for localized components there is still room for improvement. The motivation of using local weather forecast models is derived from its ability to generate high spatial and temporal resolution meteorological parameters. It is therefore expected that localized atmospheric artifacts can be compensated by using the local weather forecast models. In this Chapter, the output produced by the WRF model is used as input for the D-LOS integration method to mitigate APS from interferograms. In order to do so, a brief overview of local weather forecast models is firstly given. Then the details of running the latest local WRF model is explained. Once the desired meteorological parameters are generated by the WRF model, the D-LOS method is thereafter applied to correct the atmospheric artifacts.

The D-LOS correction method based on the WRF model has been validated on the Tenerife, Spain, Almería, Spain test sites. In Tenerife, firstly if we compare the WRF results with the ones from the global reanalysis ERA5 data, the WRF model presents

a worse correction performance than the ERA5. On the one hand, for some cases, the Ifg5 for example, the WRF model fails to reduce its phase SD, while the ERA5 can correct it with a 35% reduction. On the other hand, for the twelve interferograms, 50% phase reduction can be achieved on average by the ERA5 data, which is better than the results from all the three domains WRF model. Secondly, an internal comparison of the three domains WRF shows that the correcting ability decreases with the increasing of the spatial resolution. As the phase SD reduction decreases from 44% for the 27 km domain to 38% for the 9 km and up to 32% for the 3 km domain. In Almería, in general the three domains WRF model shows a similar correction ability with the ERA5 data. For the twelve interferograms, the ERA5 can achieve 29% phase variance reduction on average, while the 27 km WRF model can reduce it by 24%. For the 9 km and 3 km case, the number is 25% on average, excluding the Ifg8 case. Because in this case, both the 9 km and 3 km WRF models even add phase variance to the original interferogram, rather than reduce it.

From the test cases, it can be found that the latest local weather forecast model, WRF, cannot achieve our expectation to correct localized atmospheric artifacts by taking advantage of its high spatial resolution. By now, the current WRF model may simulate meteorological parameters precisely and reliably in other regions, or other meteorological parameters well rather than the ones used for calculating phase delays. The bad performance of the WRF model for APS correction also arises an opportunity to improve the WRF model by assimilating the phase delays from interferograms.

6

Chapter 6

Application for Gansu of APS correction methods

In the previous Chapters, a linear-based empirical method and a D-LOS integration method based on both global and local numerical weather forecast data have been developed and validated in several regions. In these test sites, by analysing phase deviations for original differential interferograms and residual phases, it has been proved that atmospheric artifacts can be removed to some extent. However, these validations are implemented to interferograms with no significant deformations. In practice, ground deformations and atmospheric artifacts are usually mixed together, especially in mountainous regions where interferograms are prone to suffer strong atmospheric artifacts contaminations. Meanwhile, in mountainous regions, geohazards, such as landslide, debris flow, occur very often. Therefore it is necessary to remove atmospheric artifacts from interferograms prior to applying any InSAR techniques. In this Chapter, the developed methods will further be applied to a region in Gansu, China, where there are significant deformations caused by landslide and human activities. The interferogram 20160418-20160512 is carefully analysed in this site. By applying and comparing all the methods developed in this thesis, it can be seen that the V-LMRTA method and D-LOS integration method based on ERA5 data have a good APS correcting performance, but the MERRA2 data and WRF model cannot achieve the equivalent performance. In addition, it has been proved that atmospheric artifacts mitigation can make a difference to reveal deformation phenomena. However, the failure of the APS correction also reminds us that no matter what APS compensation methods are, it needs to be carefully evaluated before applying it.

6.1 Introduction

The study area is located in the east of Qinghai province and the west of Gansu province, China. Fig. 6.1(a) shows the geographical location of the study area. It lies in a mountainous region and its geological structure belongs to the Loess Plateau, which is characterized by its most distinctive feature, namely, the highly friable loess soil. A west-east valley lies in the center, surrounded by a stretch of mountains. The relative elevation difference of the study area is up to 2800 m. This district has a semi-arid climate, with extensive monsoonal influence. Rainfall tends to be heavily concentrated in hot summer, while winters are cold and dry. This region is also blessed with an abundance of natural resources, such as oil, coal, gas, shale. Therefore it is prone to attract human activities related to natural resources extraction, which contributes to the deterioration of geohazards.

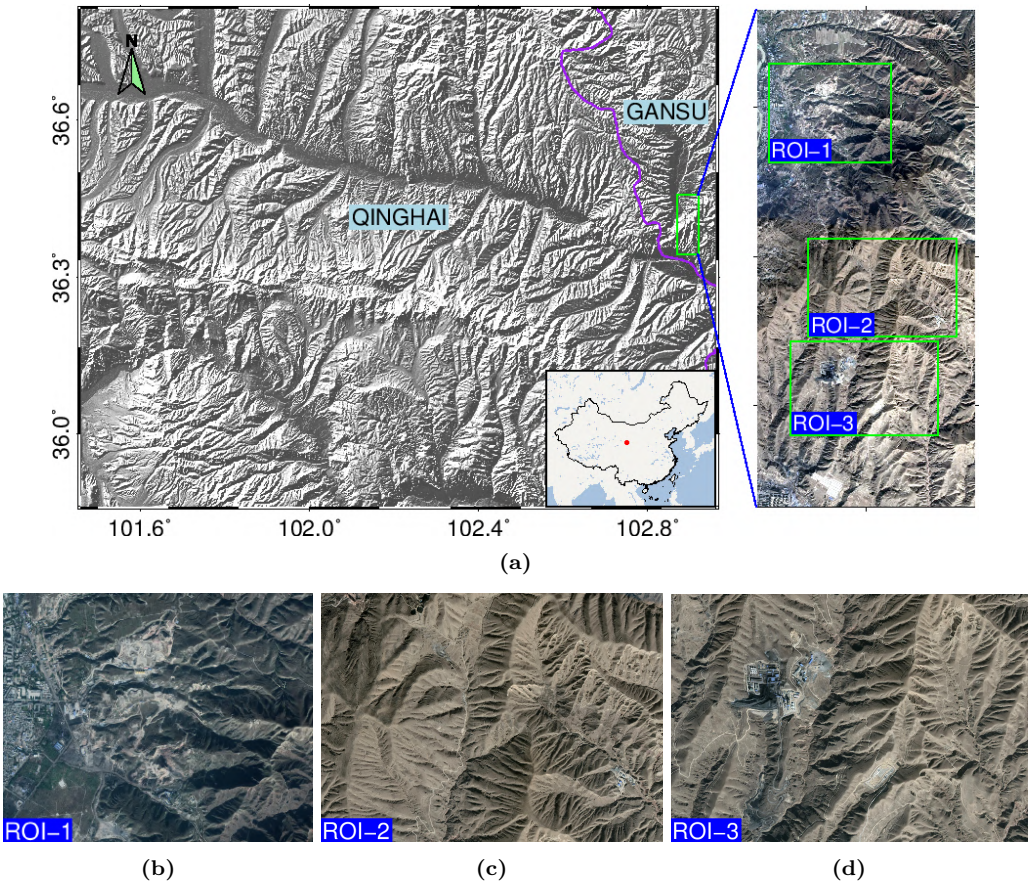

Fig. 6.1. Geography location of the study area, Gansu province, China. (a) The topography of the study area as well as zoom in of the deformation area in google earth. (b) ROI-1, corresponding to a quarry. (c) ROI-2, corresponding to a landslide area. (d) ROI-3, corresponding to a coal mining area.

Honggu district, labeled in a green rectangle in Fig. 6.1(a), is a region suffering coal mining, quarry construction activities. As a consequence, ground deformation spreads over this district. Although we do not have extra information in terms of the progress of the mining, quarrying activities and ground truth deformation in this area, the deformation phenomenon caused by the human activities can be clearly seen in interferograms, especially after the APS correction. Besides, optical images from google earth can further identify these surface deformation phenomena. Fig. 6.1(a) indicates three ROIs, corresponding to a quarry (ROI-1), landslide area (ROI-2) and a coal mining area (ROI-3). Zoom in figures for the three ROIs are shown in Fig. 6.1(b), Fig. 6.1(c), Fig. 6.1(d), where the resources extraction areas and suspect landslide area can be clearly seen with the naked eye.

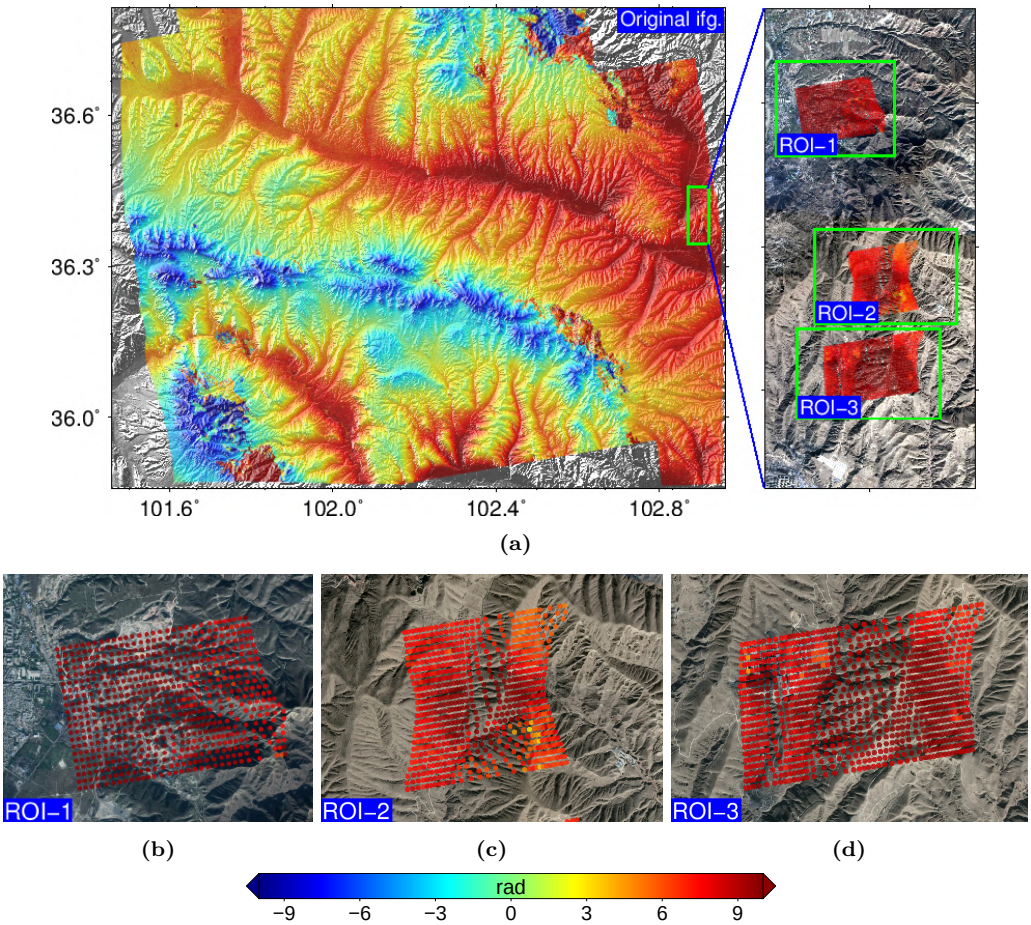

Fig. 6.2. Original differential interferogram for 20160418-20160512 case study in Gansu, China. (a) An overview of the original differential interferogram in the study area. (b) Zoom in for the ROI-1, corresponding to a quarry. (c) Zoom in for the ROI-2, corresponding to a landslide area. (d) Zoom in for the ROI-3, corresponding to a coal mining area.

InSAR technique is an ideal tool to reveal the ground deformation in such a wide mountainous area. As in addition to laborious work, other traditional monitoring ap-

proaches are difficult to implement. However, differential interferograms in such a mountainous area are usually contaminated by atmospheric artifacts. Fig. 6.2(a) shows the 20160418-20160512 differential interferogram, from which it is clear to see that the atmospheric artifacts is prominent, spreading all over the interferogram and covering up the deformation areas. From the zoom in figures in Fig. 6.2(b), Fig. 6.2(c) and Fig. 6.2(d), it is challenging to retrieve deformation information from the atmospheric artifacts and deformation mixed signals. In the following sections, the developed methods in this thesis will be applied to separate the two mixed signals in the interferogram.

6.2 Implementation and results discussion

In this Section, the developed V-LMRTA method in Chapter 3, the D-LOS method based on the MERRA2 and ERA5 data in Chapter 4 and the D-LOS method based on the WRF model in Chapter 5 are implemented to the 20160418-20160512 interferogram in Gansu test site. This interferogram pair has a temporal baseline of only 24 days and a spatial baseline of 58.4 m. In such a short baselines case, it is assumed that coherence is preserved. In addition, after removing the topographic phase contribution, it is expected that the prominent phase components are made of atmospheric artifacts and deformations. As it is shown in Fig. 6.2(a), the atmospheric artifacts are correlated with topography. At first sight, it is difficult to identify the deformation area in the original differential interferogram. As we do not have detailed ground truth information, the performance of these methods will be evaluated from two aspects. One is based on phase SD reduction all over the interferogram. The second one is a comparison analysis focusing on the three ROIs between the original and corrected interferogram.

6.2.1 Simulated atmospheric artifacts

The estimated APS delays are shown in Fig. 6.3, in which Fig. 6.3(b), Fig. 6.3(c), Fig. 6.3(d) and Fig. 6.3(e) presents the APS estimated by the V-LMRTA method, MERRA2, ERA5 and 27 km WRF model, respectively. With regard to the pattern of atmospheric artifacts, all the methods are able to generate a similar one to the original differential interferogram (Fig. 6.3(a)), except the one calculated from MERRA2 data, in which no phase trend is obtained. In addition, it is clear that the estimated APSs share a very similar pattern to the topography. In terms of the amplitude, among the four results, the V-LMRTA method shows the best performance, while the WRF model performs the worst. Because in low altitude areas, the WRF model estimates the APS in a opposite trend in some areas. Note that the result presented by the ERA5 is promising, as a similar pattern can be observed in the estimated APS. Moreover, it is noted that the V-LMRTA APS is almost a duplicate of the original differential interferogram.

6.2.2 V-LMRTA residual

After subtracting the V-LMRTA APS from the original differential interferogram, the phase residual is presented in Fig. 6.4(a). On the one hand, on the large scale, the residual phase is consistent all over the entire image, except some random phases at the tops

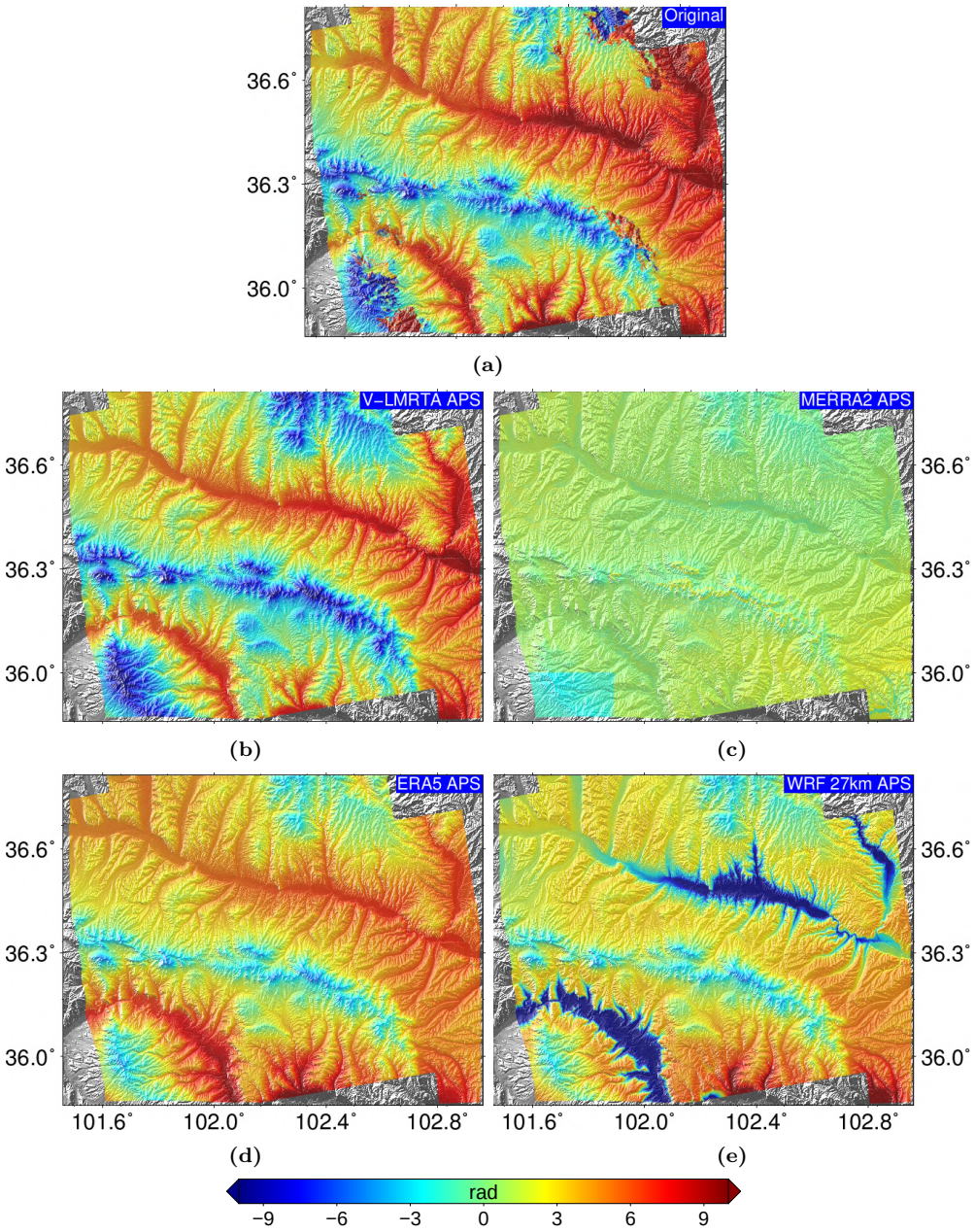

Fig. 6.3. Original differential interferogram and APSs estimated from different methods for the 20160418-20160512 case in Gansu, China. (a) The original differential interferogram. (b) The APS calculated by V-LMRTA method. (c) The APS calculated from MERRA2 data. (d) The APS calculated from ERA5 data. (e) The APS calculated from 27km WRF model.

of mountains probably due to snow cover. In other words, the topography related atmospheric artifacts can be removed by the V-LMRTA model. The outstanding correction

can also prove that the atmospheric artifacts are linearly correlated with topography in this particular case. From the statistical point of view, the phase SD for the original differential interferogram is 2.70 *rad*. After the V-LMRTA correction, the value can be reduced to only 1.05 *rad* for the residual phase, showing 59.3% reduction. On the other hand, on the local scale, if we pay attention to the ROIs, the areas affected by deformation clearly appear on the APS cleaned interferogram. To be more specific, deformation phenomena caused by quarrying in ROI-1, landslide in ROI-2 and coal mining activity in ROI-3 are clearly seen in the residual interferogram. Corresponding zoom in figures are shown in Fig. 6.4(b), Fig. 6.4(c) and Fig. 6.4(d).

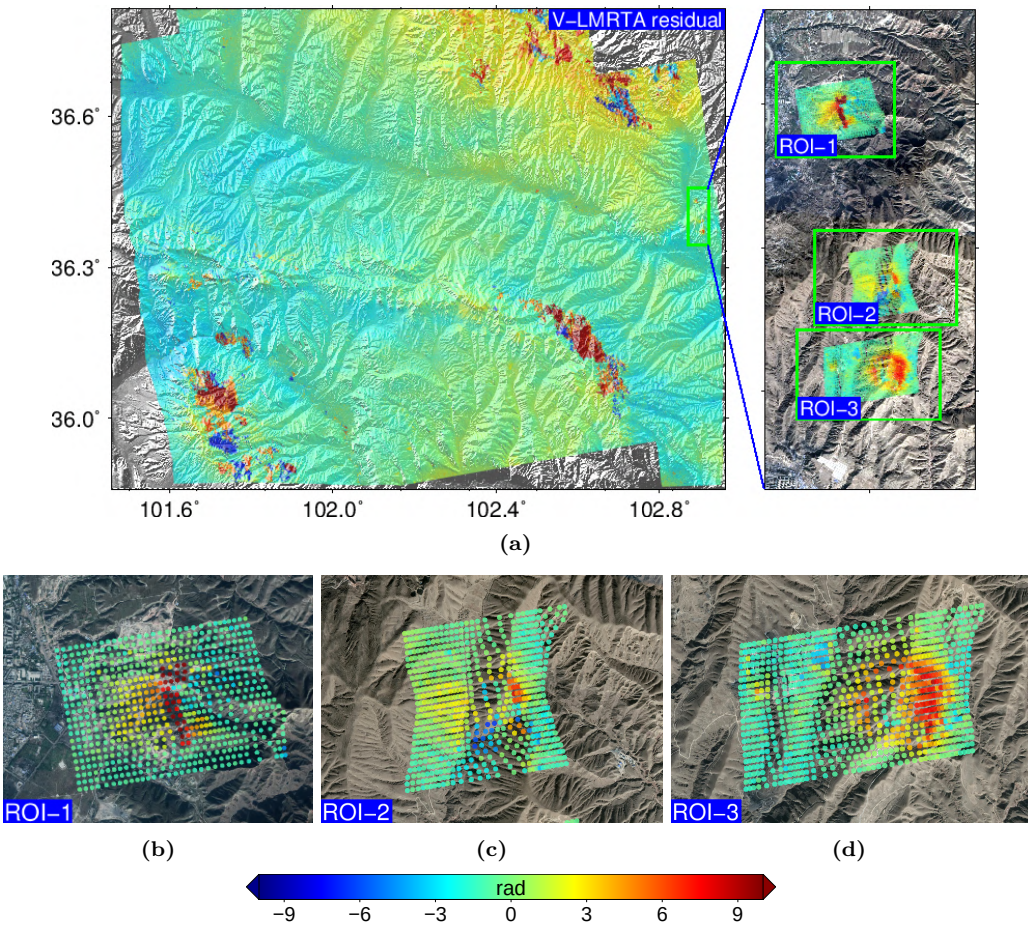

Fig. 6.4. Residual phase for the 20160418-20160512 case study after the V-LMRTA correction in Gansu, China. (a) An overview of the residual phase in the study area. (b) Zoom in for the ROI-1, corresponding to a quarry. (c) Zoom in for the ROI-2, corresponding to a landslide area. (d) Zoom in for the ROI-3, corresponding to a coal mining area.

6.2.3 D-LOS MERRA2 residual

Fig. 6.5(a) shows the residual phase after D-LOS compensation based on the MERRA2 data. It is evident that the MERRA2 data has a limited ability to remove the atmospheric artifacts for this particular case. If we pay attention to the estimated MERRA2 APS once again in Fig. 6.3(c), it can be seen that the APS is extremely underestimated. As a consequence, subsidence phenomena in Fig. 6.5(b), Fig. 6.5(c) and Fig. 6.5(d) are still concealed under the atmospheric artifacts in the residual, or at least the subsidence area is not clear. In statistics, the MERRA2 correction can only slightly reduce SD from 2.70 *rad* to 2.65 *rad*, which further proves the poor performance of MERRA2 data in this particular case.

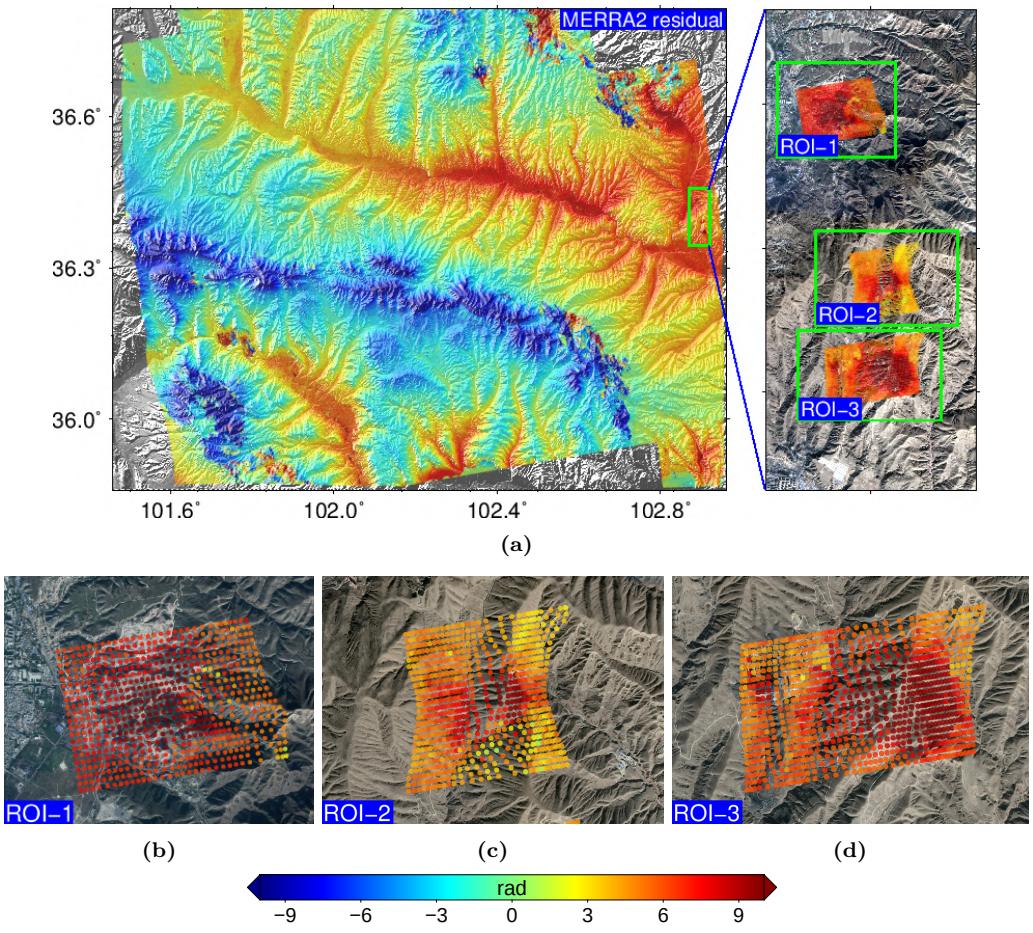

Fig. 6.5. Residual phase for the 20160418-20160512 case study after the MERRA2 correction in Gansu, China. (a) An overview of the residual phase in the study area. (b) Zoom in for the ROI-1, corresponding to a quarry. (c) Zoom in for the ROI-2, corresponding to a landslide area. (d) Zoom in for the ROI-3, corresponding to a coal mining area.

6.2.4 D-LOS ERA5 residual

The ERA5 pressure level data is used to correct the atmospheric artifacts for this case. The residual phase after the ERA5 correction is shown in Fig. 6.6(a). Compared to the original differential interferogram in Fig. 6.2(a), it can be seen that most part of APS has been removed. If we focus on the ROIs, there is a striking contrast regarding to the deformation areas between the original differential interferogram and the residual phase. In Fig. 6.6(b), Fig. 6.6(c) and Fig. 6.6(d), it is clear that the deformation areas appear after the ERA5 correction. In terms of phase SD reduction, the SD value is reduced from 2.70 *rad* to 1.43 *rad*. Compared to the V-LMRTA method, the D-LOS ERA5 correction demonstrates its comparable correcting ability.

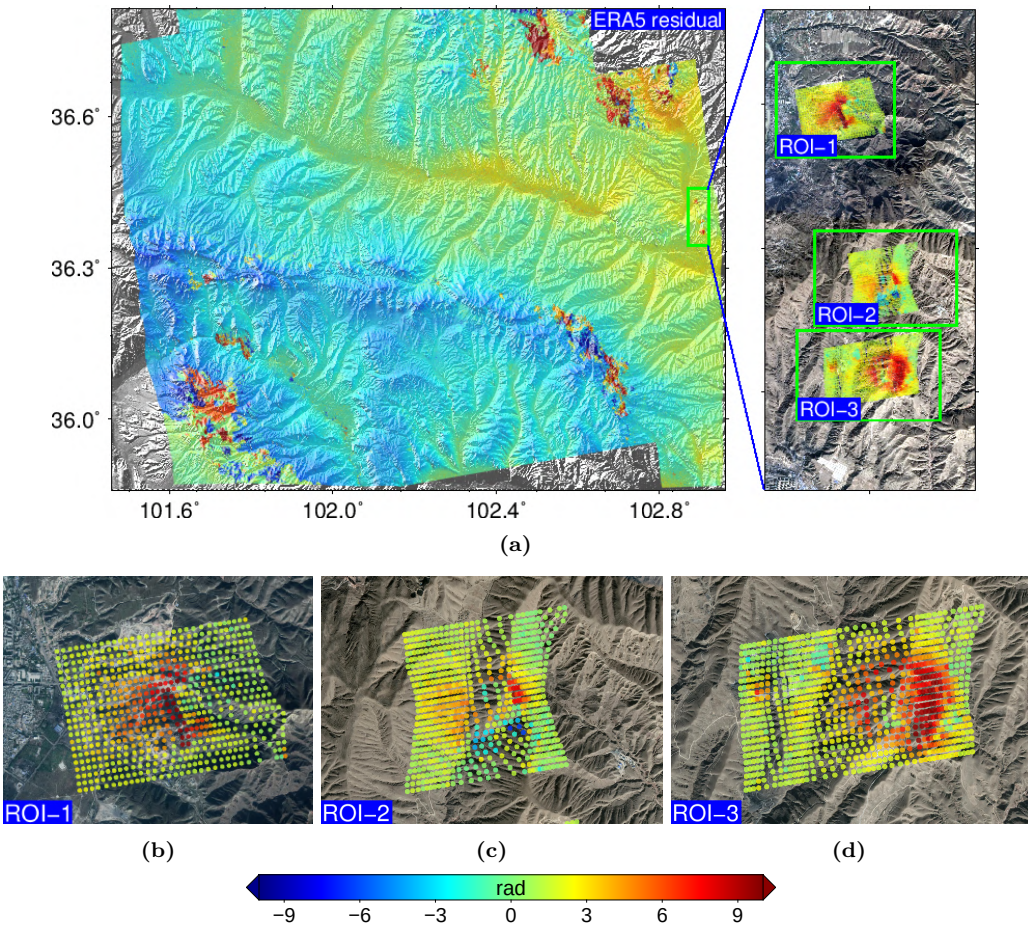

Fig. 6.6. Residual phase for the 20160418-20160512 case study after the ERA5 correction in Gansu, China. (a) An overview of the residual phase in the study area. (b) Zoom in for the ROI-1, corresponding to a quarry. (c) Zoom in for the ROI-2, corresponding to a landslide area. (d) Zoom in for the ROI-3, corresponding to a coal mining area.

6.2.5 D-LOS WRF residual

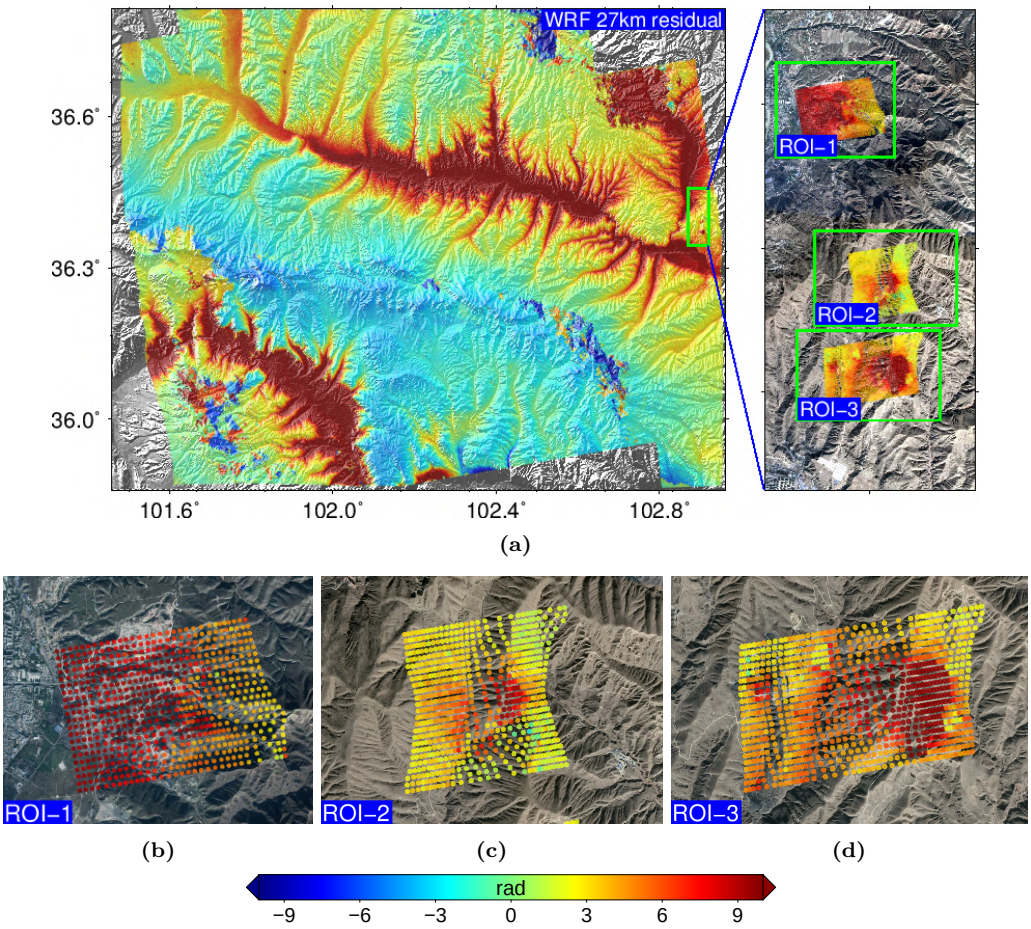

Fig. 6.7. Residual phase for the 20160418-20160512 case study after the WRF correction in Gansu, China. (a) An overview of the residual phase in the study area. (b) Zoom in for the ROI-1, corresponding to a quarry. (c) Zoom in for the ROI-2, corresponding to a landslide area. (d) Zoom in for the ROI-3, corresponding to a coal mining area.

As discussed in Chapter 5, a higher spatial resolution of meteorological parameters from the WRF model does not mean a better APS correction. Moreover, in some cases, the 27 km resolution WRF model can achieve better performance than higher resolution 9 km and 3 km WRF ones. Therefore, in Gansu site, the 27 km WRF model is implemented to generate high resolution weather forecast data. Fig. 6.7(a) shows the residual result after the WRF model compensation. Unfortunately, the WRF model can slightly remove APS only for a small part of the interferogram (around the ridge). For the most part, the WRF correction deteriorates the original differential interferogram, rather than mitigating it. Especially in the areas with low altitude, the original differential interferometric phase is contaminated seriously by the erroneously simulated APS. As a consequence, the deformation in the ROIs is still mixed with strong atmospheric artifacts, as shown

in Fig. 6.7(b), Fig. 6.7(c) and Fig. 6.7(d). The terrible correction performance is also reflected on the phase SD, which is increased from 2.70 *rad* to 9.84 *rad* in the residual phase.

6.3 Summary

In this Chapter, the developed APS correction methods have been applied to the Gansu, China test site, where the deformation signal is mixed with atmospheric artifacts. Therefore, it is an ideal case to test the feasibility of APS correction methods to separate the two phase components.

Based on the aforementioned discussion, it can be concluded that among the four different corrections, on the one hand, the V-LMRTA and D-LOS method based on ERA5 reanalysis data can provide a reliable APS mitigation for this particular case. As a result, the residual phases are reasonable after the two compensations. First of all, the two methods are able to present a comparable correction in terms of both the trend of the atmospheric artifacts and its amplitude. Besides, the subsidence phenomena caused by human activities in the ROIs are clearly visible in the residual phases. On the other hand, the D-LOS method based on MERRA2 has a limited ability to remove the atmospheric artifacts, while the WRF based correction even deteriorates the original differential interferogram. As it is well known that the purpose of any APS compensations is to mitigate it as much as possible on the premise that the correction methods do not incur any additional contamination. Consequently, the failure of the WRF correction also calls our attention to that any APS correction methods should be carefully analysed and verified before applying it for each individual case. If ground truth data for the deformation is not available, phase SD is an alternative index to assess the correction performance. In general, a better APS correction always demonstrates a larger phase SD reduction than a worse one.

7

Chapter 7
Conclusions and future lines

InSAR techniques have proven to be powerful for measuring deformations and mapping topography during the last decades. However, atmospheric artifacts are one of the main error sources that influences the accuracy of InSAR results. In some cases, the APS contamination can lead to unacceptable estimations of geographical parameters. Consequently, a particular attention has to be paid on the APS correction before applying any advanced InSAR technique. This PhD thesis has been devoted to the APS mitigation in interferograms. For this purpose, two correction methods have been developed. The first mitigation method estimates a linear correlated stratified APS from interferograms themselves considering the influence of the turbulent component. The second method takes advantage of auxiliary meteorological data, including both global and local numerical weather prediction models. The main conclusions of the thesis and possible future lines are summarized as follows.

7.1 Conclusions

7.1.1 Correcting APS using a covariance-weighted linear model

Atmospheric artifacts can be estimated by empirical models, such as a linear model or a power law function. The main advantage is their independence of any auxiliary data. These models can be thus adjusted directly to the interferograms with no further data required. However, the reliability of the estimated stratified APS can be effected if turbu-

lent component exists. A covariance-weighting method has been developed in Chapter 3 for a more robust model adjustment in presence of turbulent atmosphere. The proposed method consists of two main steps. Firstly, an improved linear model is defined that considers phase differences among selected pixels instead of their absolute values, known as LMRTA. If two pixels present similar values of turbulent atmosphere, this component would not affect the model adjustment. Secondly, when adjusting the model to the observed phases a proper weighting strategy is applied based on the spatial characteristics of the turbulent APS in order to further reduce its impact as much as possible. The most sophisticated weighting strategy uses the spatial covariance matrix obtained from the empirical variogram to determine how two pixels are affected by the turbulent component, known as V-LMRTA. On account of its high computational burden, an alternate and simpler weighting strategy is based on just using the pixel's distance, known as D-LMRTA. Separated pixels have more chances of being affected by different turbulent atmosphere that closer ones. The difference between both strategies has been studied, which shows that the sophisticated weighting strategy slightly outperforms the simpler one. So, in practice, it is not worth to use the variogram weighting strategy.

The proposed approach has been validated with both simulated data and fourteen Sentinel-1 interferograms from Tenerife. Results have been compared to the conventional linear model method and the D-LOS method based on the ERA5 weather forecast data. On the one hand, 135 interferograms have been simulated with a wide range of turbulent component. From the results it has been concluded that the V-LMRTA method performs the best, compared to the conventional linear method and unweighted LMRTA. For pairs with mild turbulent components, the three methods show a similar correction performance. The better performance of V-LMRTA is more noticeable when the magnitude of turbulent APS increases. On the other hand, with real data a statistical comparison of the different correction methods on fourteen interferograms reveals that the LMRTA method can provide more reliable SD reduction than the conventional linear model. Even in some cases, the conventional linear model can increase the phase SD. Moreover, the correction results from the LMRTA method are closer to the ones provided by the ERA5 weather forecast data. Therefore, both the simulated and real cases have demonstrated the outstanding performance of stratified APS compensation by the covariance-weighted linear model.

However, the linear model based method is merely efficient in situations where the atmospheric artifacts follow a linear trend with the topography. The proposed LMRTA method is designed to model the linear correlated APS in a robust way. Consequently, in situations where the atmospheric artifacts do not follow a linear trend with the topography, other correction methods are necessary. As LMRTA cannot reduce the turbulent component, other approaches, like the classical temporal-spatial filtering can be used to refine the results.

7.1.2 Comparison between Z-LOS and D-LOS correction methods

The APS mitigation method based on weather forecast data is not in principle an innovative technique. However, many authors calculate the phase delay by integrating along the zenith direction and then convert it to the LOS direction (Z-LOS), instead of integrating

along the LOS directly (D-LOS). In fact, with the Z-LOS approach, it is assumed that the atmospheric parameters along the LOS direction are spatially invariant around a given location. However, the assumption fails when the atmosphere state is locally anisotropic. In Chapter 4, a realistic LOS integration method (D-LOS) has been presented and a detailed comparison with the Z-LOS approach has been performed. The framework of the D-LOS method is composed of three steps: determination of the sampling locations along the LOS path, interpolation of atmospheric parameters on the sampled locations and integrating these parameters along the LOS direction. The D-LOS approach is more realistic as it follows the same trajectory as the electromagnetic waves, and it can avoid the possible inaccuracies caused by anisotropic atmospheric states. The evaluation of the two strategies with real data has shown that D-LOS outperforms Z-LOS based on ERA5 global reanalysis data. In order to prove that the conclusions are general, three different regions, Tenerife, Spain, Almería, Spain and Crete, Greece, have been chosen as test sites.

All interferograms in the three test sites have short spatial and temporal baselines. It is assumed that in the differential interferograms there is neither significant deformation nor topography error and the APS dominates the phase components. Consequently, the performance of the APS mitigation can be assessed from the residual phase by using the SD of the residue as a metric. From the statistical point of view, for all interferograms the D-LOS approach presented more significant variance reduction than the Z-LOS method. In Tenerife island, D-LOS can achieve 23-77% SD reduction for the twelve interferograms, with an average level of 50%, while Z-LOS achieved only 14-71%, with an average decrease of 37%. In Crete, Greece test site, after applying the D-LOS correction, the SD decreased by 15-74%, with an average reduction of 38%, compared with 5-48% and corresponding average level of 22% from the Z-LOS method for the eight interferograms. Finally, over Almería, the Z-LOS method also achieved a SD reduction of 14% on average, while the D-LOS strategy showed a better performance, reaching up to 29% on average for the twelve interferograms.

In addition, the Z-LOS method failed to correct APS for one out of twelve interferograms in Tenerife and two out of twelve in Almería. To be more specific, in the three cases after the Z-LOS correction the SD of the residual phases even increased. However, the D-LOS approach succeeded in mitigating the atmospheric artifacts in all interferograms. So, it can be concluded that the realistic D-LOS method is more robust than the conventional Z-LOS approach.

7.1.3 APS mitigation using global numerical weather models

The merit of the D-LOS strategy compared to the Z-LOS one has been certified based on the global ERA5 data. The conclusion is general and it can be applied to any reanalysis dataset. A wide variety of global weather forecast reanalysis data are available to the public. The D-LOS method has been also applied to the ERA-Interim and MERRA2 datasets in Chapter 4 to further evaluate their performance. A detailed comparison between these global reanalysis datasets has been carried out. The ERA-Interim and ERA5 reanalysis datasets are from the same ECMWF family, while the MERRA2 is produced by the GEOS-5 assimilation system from NASA. Regarding their time interval, the temporal sampling of ERA5 is 1 hour, compared to the 6 hours for the ERA-Interim and MERRA2. In terms of spatial resolution, the ERA5 is also the best with a 0.28 *deg*

resolution gird in both latitude and longitude, followed by the MERRA2 with resolution of 0.5 *deg* in latitude and 0.625 *deg* in longitude and the ERA-Interim having 0.75 *deg* space interval in both latitude and longitude.

The tests carried on Tenerife have shown that the three datasets presented a very similar APS correction performance. Although the ERA5 data presented a slightly better correction with an average SD reduction of 50.2% on the twelve interferograms, compared to 49% for ERA-Interim and 48.7% for MERRA2, the differences among them were not significant. On the contrary, in Almería the performance was different for each reanalysis data. For the twelve pairs, the average phase variance reduction (29.0%) by the ERA5 data almost doubled the ones from the ERA-Interim (15.7%) and MERRA2 (14.8%). Additionally, the MERRA2 data failed to correct APS for three pairs. Therefore, the conclusion for this test site has been that ERA5 performed the best, while MERRA2 showed the worst mitigation performance. On the contrary, with the third test site, Crete, Greece, the conclusions were just the opposite, MERRA2 presented a significant SD reduction compared with ERA-Interim and slightly better than ERA5.

From the three tests it can be concluded that the performance of APS correction using different global reanalysis datasets varies from one site to another. But the correction using the latest reanalysis ERA5 data is relatively reliable. Therefore, ERA5 seems to be the most reliable option for APS mitigation.

7.1.4 APS mitigation based on the local WRF model

The reliability of using global weather forecast reanalysis data to correct APS has been demonstrated in Chapter 4. Even though the resolution of the global reanalysis data is relatively low compared to the scale of SAR images, the corrected results in the three test sites are promising. As local weather forecast models have the ability to improve the resolution of meteorological parameters, it was expected that their application can improve the performance of APS correction. To explore it, the latest local weather forecast model WRF has been evaluated in Chapter 5. In this framework, firstly, an overview of the local weather forecast models, specifically the WRF model, has been presented, followed by the WRF model setups for generating atmospheric parameters for APS calculation. After that, the D-LOS method has been applied to the refined parameters from the WRF model. For running the WRF model, ERA5 data has been used for setting the initial conditions.

Three domains with resolutions of 27 *km*, 9 *km* and 3 *km* respectively were set when running the WRF model in the different test sites. On the one hand, in Tenerife it was found that the increased spatial resolution had not implied an improvement of the APS mitigation, but just the opposite. For the twelve interferograms, the average phase SD reduction decreased from 44% for the 27 *km* domain to 38% for the 9 *km* domain and only to 32% for the 3 *km* case. On the other hand, the original global reanalysis ERA5 data was able to achieve an average phase variance reduction of 50%, which was better than all the three WRF domains corrections. For the Almería case, the average phase SD reduction for the twelve interferograms did not vary significantly with the improvement of the spatial resolution. Starting with a 24% reduction for the 27 *km* model, and ending with a 25% for both the 9 *km* and 3 *km* domains. However, similarly to the Tenerife

case, the ERA5 data provided the best APS mitigation, reducing the phase variance by a 29%.

In addition to its high computational burden, the latest local weather forecast model WRF have shown a limited ability to correct APS compared with global reanalysis data to mitigate APS. The local models have to be improved to produce better results.

7.2 Future research lines

From the APS correction point of view, the current weather forecast models, either global or local, can mitigate in the best cases atmospheric artifacts significantly. Meanwhile, in most of the cases atmospheric artifacts can only be removed partially, but in the worst ones interferograms are even deteriorated. The performance of the correction varies from one interferogram to another as well as from one site to another. In fact, the APS correction ability mainly depends on the quality of the weather forecast data. Therefore if these weather forecast models were able to produce meteorological data with quality assessment, it would help to evaluate whether the estimated APS would be reliable or not. Nowadays, the state-of-the-art ERA5 reanalysis is released with an uncertainty estimate based on a 10-member and 4D-Var ensemble at a reduced resolution of 62 km [45]. Based on this, one promising research topic would be the uncertainty propagation from the meteorological parameters to the final phase delays, which can be further used to assess the reliability of atmospheric artifacts correction.

From the perspective of the InSAR meteorology, as phase delays simulated from the weather forecast models show a great agreement with atmospheric artifacts in interferograms in some cases, the atmospheric component in interferograms can provide one auxiliary observation source for numerical weather forecast modelling. It is known that in some cases the weather forecast models have a limited ability to correct APS in interferograms. It is believed that the disagreement is mainly caused by the weather forecast models. There are two main reasons. Firstly, the reliability of weather forecast model products is prone to be effected by a variety of factors, such as the spacing of observation stations and their monitoring frequency. Nowadays both in local and global scale, neither the number stations nor the monitoring frequency are enough. Secondly, InSAR has proven to be a mature technique in many theoretical and application studies. The InSAR meteorology has a potential ability to improve weather forecast modelling in two aspects. For large scale weather forecast modelling, today SAR images have a global coverage with relative short repeat cycles. Moreover, Geostationary Synthetic Aperture Radar (GeoSAR) missions, in the future, would be able to obtain continuous images over the Earth's surface. The InSAR technique therefore is promising to help improve any global weather forecast models. For small scale weather forecast modelling, SAR images are acquired in very fine spatial scale compared to weather monitoring stations. As it can be seen from the results presented in the thesis, APS corrections using the local WRF model are not able to cope with local atmospheric artifacts, which are clearly visible in many interferograms. Therefore, it might be a challenge to retrieve local meteorological parameters from interferograms and integrate these observations into local weather forecast models.

List of Figures

2.1 Summary of SAR satellites. 9
2.2 SAR geometrical configuration. 9
2.3 Amplitude of PAZ and Gaofen-3 SAR images over Barcelona. 10
2.4 An example of one interferogram and differential interferogram over Mojave, California. 13
2.5 Coherence map over Mojave, California. 15
2.6 Two examples of atmospheric artifacts. 18
2.7 Overview of CPT blocks. 21

3.1 Two examples of true and estimated turbulent APS in the simulator. . . . 32
3.2 Delaunay triangulation in the simulator. 33
3.3 Experimental variograms. 34
3.4 Minimization Function. 35
3.5 Linear deformation pattern in simulated interferograms. 36
3.6 Scatter plot between $\sigma(0)$ and absolute SD error. 37
3.7 Location of Canary Archipelago. 38
3.8 Wrapped differential interferograms with strong topography-related APS. 39
3.9 Relationship between the number of fringes and spatial baseline. 40
3.10 LMRTA diagram for atmospheric artifacts compensation. 40
3.11 20151031-20151206 case study of APS compensation over Tenerife island. 42
3.12 SD of phase residues at each iteration. 43
3.13 Two case studies, 20150715-20150808 (Ifg2) and 20160709-20160826 (Ifg13). 46

4.1 An example of realistic atmospheric heterogeneities. 51
4.2 Sentinel-1 IW and EW acquisition modes. 52
4.3 Geometry of LOS path in Cartesian coordinate system. 53
4.4 Overview of geographic locations of the test sites. 55

4.5 Spline interpolation for atmospheric parameters. 58
4.6 Relative tropospheric phase delay along vertical direction. 58
4.7 Original interferograms over Tenerife island. 60
4.8 Relationship between the number of fringes and spatial baseline. 60
4.9 20160721-20160814 case study of APS compensation over Tenerife. 61
4.10 Statistical comparison of APS correction in Tenerife. 63
4.11 20171126-20171208 case study of APS compensation over Crete. 65
4.12 Statistical comparison of APS correction in Crete. 66
4.13 20171031-20171124 case study of APS compensation over Almería. 67
4.14 Statistical comparison of APS correction in Almería. 68
4.15 Distribution of meteorological data for the three test sites. 70
4.16 20160721-20160814 case study of APS compensation over Tenerife using ERA-Interim, ERA5 and MERRA2 reanalysis data. 71
4.17 20160721-20160814 case study of phase-elevation scatters for APS compensation over Tenerife using ERA-Interim, ERA5 and MERRA2 reanalysis data. 72
4.18 Differences between the estimated APS for the 20160721-20160814 (Ifg11) case study over Tenerife. 74
4.19 20160510-20160615 case study of APS compensation in Tenerife using ERA-Interim, ERA5 and MERRA2 reanalysis data. 75
4.20 20171031-20171124 case study of APS compensation over Almería using ERA-Interim, ERA5 and MERRA2 reanalysis data. 76
4.21 20171126-20171208 case study of APS compensation over Crete using ERA-Interim, ERA5 and MERRA2 reanalysis data. 79

5.1 Diagram of local NWP model for APS compensation. 85
5.2 Higher resolution of temperature producted by the WRF model. 87
5.3 The flow chart of the WRF model. 88
5.4 The parameters determining the simulated domain in the WRF model. . . 92
5.5 Illustration of temperature for multiple WRF domains in Tenerife. 94
5.6 20160721-20160814 case study of APS compensation using WRF model over Tenerife. 95
5.7 20171031-20171124 case study of APS compensation using WRF model over Almería. 98

6.1 Geography location of the study area, Gansu province, China. 102
6.2 Original differential interferogram for 20160418-20160512 case study in Gansu, China. 103

6.3 Original differential interferogram and APSs estiamted from different methods for the 20160418-20160512 case in Gansu, China. 105
6.4 Residual phase for the 20160418-20160512 case study after the V-LMRTA correction in Gansu, China. 106
6.5 Residual phase for the 20160418-20160512 case study after the MERRA2 correction in Gansu, China. 107
6.6 Residual phase for the 20160418-20160512 case study after the ERA5 correction in Gansu, China. 108
6.7 Residual phase for the 20160418-20160512 case study after the WRF correction in Gansu, China. 109

List of Tables

3.1 Parameters over a synthetic scenario 31
3.2 True and estimated coefficients 35
3.3 Performance of different correction methods 37
3.4 Statistical comparison of different correction methods in the simulator . . 37
3.5 Performance of different correction methods in Tenerife 45

4.1 Statistical comparison of APS correction over Tenerife using ERA5 data. . 59
4.2 Statistical comparison of APS correction over Crete using ERA5 data. . . 63
4.3 Statistical comparison of APS correction over Almería using ERA5 data. . 68
4.4 Comparison of different global atmospheric models. 70
4.5 Statistical comparison of APS correction in Tenerife using different GAM data. 74
4.6 Statistical comparison of APS correction in Almería using different GAM data. 78
4.7 Statistical comparison of APS correction in Crete using different GAM data. 80

5.1 Comparison of different numerical weather prediction models. 86
5.2 Compulsory static geographical data for the WRF model. 90
5.3 Required fields for the ARW programs. 91
5.4 Description of variables in the WPS namelist file. 91
5.5 Description of variables in the ARW namelist file. 92
5.6 Statistical comparison of APS correction in Tenerife using the WRF model. 97
5.7 Statistical comparison of APS correction in Almería using the WRF model. 99

Bibliography

[1] T. J. Wright, Z. Lu, and C. Wicks, "Source model for the M_w 6.7, 23 October 2002, Nenana mountain earthquake (Alaska) from InSAR," *Geophysical Research Letters*, vol. 30, no. 18, 2003.

[2] B. Delouis, J.-M. Nocquet, and M. Vallée, "Slip distribution of the February 27, 2010 M_w= 8.8 Maule earthquake, central Chile, from static and high-rate GPS, InSAR, and broadband teleseismic data," *Geophysical Research Letters*, vol. 37, no. 17, 2010.

[3] M. Polcari, A. Montuori, C. Bignami, M. Moro, S. Stramondo, and C. Tolomei, "Using multi-band InSAR data for detecting local deformation phenomena induced by the 2016–2017 central Italy seismic sequence," *Remote Sensing of Environment*, vol. 201, pp. 234–242, 2017.

[4] O. Cavalié, C. Lasserre, M.-P. Doin, G. Peltzer, J. Sun, X. Xu, and Z.-K. Shen, "Measurement of interseismic strain across the Haiyuan fault (Gansu, China), by InSAR," *Earth and Planetary Science Letters*, vol. 275, no. 3, pp. 246–257, 2008.

[5] J. Biggs, F. Amelung, N. Gourmelen, T. H. Dixon, and S.-W. Kim, "InSAR observations of 2007 Tanzania rifting episode reveal mixed fault and dyke extension in an immature continental rift," *Geophysical Journal International*, vol. 179, no. 1, pp. 549–558, 2009.

[6] Z. Lu and J. T. Freymueller, "Synthetic aperture radar interferometry coherence analysis over Katmai volcano group, Alaska," *Journal of Geophysical Research: Solid Earth*, vol. 103, no. B12, pp. 29 887–29 894, 1998.

[7] E. Chaussard, F. Amelung, and Y. Aoki, "Characterization of open and closed volcanic systems in Indonesia and Mexico using InSAR time series," *Journal of Geophysical Research: Solid Earth*, vol. 118, no. 8, pp. 3957–3969, 2013.

[8] D. Massonnet, P. Briole, and A. Arnaud, "Deflation of Mount Etna monitored by spaceborne radar interferometry," *Nature*, vol. 375, no. 6532, pp. 567–570, 1995.

[9] A. Singleton, Z. Li, T. Hoey, and J.-P. Muller, "Evaluating sub-pixel offset techniques as an alternative to D-InSAR for monitoring episodic landslide movements in vegetated terrain," *Remote Sensing of Environment*, vol. 147, pp. 133–144, 2014.

[10] D. Massonnet and K. L. Feigl, "Radar interferometry and its application to changes in the Earth's surface," *Reviews of Geophysics*, vol. 36, no. 4, pp. 441–500, 1998.

[11] A. Rucci, A. Ferretti, A. M. Guarnieri, and F. Rocca, "Sentinel 1 SAR interferometry applications: The outlook for sub millimeter measurements," *Remote Sensing of Environment*, vol. 120, pp. 156–163, 2012.

[12] A. Ferretti, D. Colombo, A. Fumagalli, F. Novali, and A. Rucci, "InSAR data for monitoring land subsidence: time to think big," *Proceedings of the International Association of Hydrological Sciences*, vol. 372, p. 331, 2015.

[13] K. Spaans and A. Hooper, "InSAR processing for volcano monitoring and other near-real time applications," *Journal of Geophysical Research: Solid Earth*, vol. 121, no. 4, pp. 2947–2960, 2016.

[14] R. Goldstein, "Atmospheric limitations to repeat-track radar interferometry," *Geophysical Research Letters*, vol. 22, no. 18, pp. 2517–2520, 1995.

[15] H. A. Zebker, P. A. Rosen, and S. Hensley, "Atmospheric effects in interferometric synthetic aperture radar surface deformation and topographic maps," *Journal of Geophysical Research: Solid Earth*, vol. 102, no. B4, pp. 7547–7563, 1997.

[16] R. F. Hanssen, *Radar interferometry: data interpretation and error analysis*. Dordrecht, The Netherlands: Kluwer, 2001.

[17] A. Ferretti, C. Prati, and F. Rocca, "Permanent scatterers in SAR interferometry," *IEEE Transactions on Geoscience and Remote Sensing*, vol. 39, no. 1, pp. 8–20, 2001.

[18] P. Berardino, G. Fornaro, R. Lanari, and E. Sansosti, "A new algorithm for surface deformation monitoring based on small baseline differential SAR interferograms," *IEEE Transactions on Geoscience and Remote Sensing*, vol. 40, no. 11, pp. 2375–2383, 2002.

[19] R. Lanari, O. Mora, M. Manunta, J. J. Mallorquí, P. Berardino, and E. Sansosti, "A small-baseline approach for investigating deformations on full-resolution differential SAR interferograms," *IEEE Transactions on Geoscience and Remote Sensing*, vol. 42, no. 7, pp. 1377–1386, 2004.

[20] P. Blanco-Sanchez, J. J. Mallorquí, S. Duque, and D. Monells, "The Coherent Pixels Technique (CPT): An advanced DInSAR technique for nonlinear deformation monitoring," *Pure and Applied Geophysics*, vol. 165, no. 6, pp. 1167–1193, Jun. 2008.

[21] S. Liu, "Satellite radar interferometry: estimation of atmospheric delay," Ph.D. dissertation, Delft University of Technology, Delft, The Netherlands, 2012.

[22] W. Gong, F. J. Meyer, S. Liu, and R. F. Hanssen, "Temporal filtering of InSAR data using statistical parameters from NWP models," *IEEE Transactions on Geoscience and Remote Sensing*, vol. 53, no. 7, pp. 4033–4044, 2015.

[23] S. H. Knospe and S. Jonsson, "Covariance estimation for DInSAR surface deformation measurements in the presence of anisotropic atmospheric noise," *IEEE Transactions on Geoscience and Remote Sensing*, vol. 48, no. 4, pp. 2057–2065, 2010.

[24] F. Beauducel, P. Briole, and J.-L. Froger, "Volcano-wide fringes in ERS synthetic aperture radar interferograms of Etna (1992–1998): Deformation or tropospheric effect?" *Journal of Geophysical Research: Solid Earth*, vol. 105, no. B7, pp. 16 391–16 402, Jul. 2000.

[25] O. Cavalié, M.-P. Doin, C. Lasserre, and P. Briole, "Ground motion measurement in the Lake Mead area, Nevada, by differential synthetic aperture radar interferometry time series analysis: Probing the lithosphere rheological structure," *Journal of Geophysical Research: Solid Earth*, vol. 112, no. B3, Mar. 2007.

[26] J. Elliott, J. Biggs, B. Parsons, and T. Wright, "InSAR slip rate determination on the Altyn Tagh Fault, northern Tibet, in the presence of topographically correlated atmospheric delays," *Geophysical Research Letters*, vol. 35, no. 12, Jun. 2008.

[27] M. P. Doin, C. Lasserre, G. Peltzer, O. Cavalié, and C. Doubre, "Corrections of stratified tropospheric delays in SAR interferometry: Validation with global atmospheric models," *Journal of Applied Geophysics*, vol. 69, no. 1, pp. 35–50, Sep. 2009.

[28] Y. N. Lin, M. Simons, E. A. Hetland, P. Muse, and C. DiCaprio, "A multiscale approach to estimating topographically correlated propagation delays in radar interferograms," *Geochemistry, Geophysics, Geosystems*, vol. 11, no. 9, pp. 1–17, Sep. 2010.

[29] R. Iglesias, X. Fabregas, A. Aguasca, J. J. Mallorquí, C. López-Martínez, J. A. Gili, and J. Corominas, "Atmospheric phase screen compensation in ground-based SAR with a multiple-regression model over mountainous regions," *IEEE Transactions on Geoscience and Remote Sensing*, vol. 52, no. 5, pp. 2436–2449, 2014.

[30] D. Bekaert, A. Hooper, and T. Wright, "A spatially variable power law tropospheric correction technique for InSAR data," *Journal of Geophysical Research: Solid Earth*, vol. 120, no. 2, pp. 1345–1356, Feb. 2015.

[31] F. Chaabane, A. Avallone, F. Tupin, P. Briole, and H. Maître, "A multitemporal method for correction of tropospheric effects in differential SAR interferometry: Application to the Gulf of Corinth earthquake," *IEEE Transactions on Geoscience and Remote Sensing*, vol. 45, no. 6, pp. 1605–1615, 2007.

[32] S. Williams, Y. Bock, and P. Fang, "Integrated satellite interferometry: Tropospheric noise, GPS estimates and implications for interferometric synthetic aperture radar products," *Journal of Geophysical Research: Solid Earth*, vol. 103, no. B11, pp. 27 051–27 067, 1998.

[33] G. Wadge, P. Webley, I. James, R. Bingley, A. Dodson, S. Waugh, T. Veneboer, G. Puglisi, M. Mattia, D. Baker *et al.*, "Atmospheric models, GPS and InSAR measurements of the tropospheric water vapour field over Mount Etna," *Geophysical Research Letters*, vol. 29, no. 19, pp. 11–1–11–4, Oct. 2002.

[34] F. Onn and H. Zebker, "Correction for interferometric synthetic aperture radar atmospheric phase artifacts using time series of zenith wet delay observations from a GPS network," *Journal of Geophysical Research: Solid Earth*, vol. 111, no. B9, Sep. 2006.

[35] J. S. Löfgren, F. Björndahl, A. W. Moore, F. H. Webb, E. J. Fielding, and E. F. Fishbein, "Tropospheric correction for InSAR using interpolated ECMWF data and GPS zenith total delay from the Southern California integrated GPS network," in *Proc. IGARSS*, Honolulu, USA, 2010, pp. 4503–4506.

[36] C. Yu, N. T. Penna, and Z. Li, "Generation of real-time mode high-resolution water vapor fields from GPS observations," *Journal of Geophysical Research: Atmospheres*, vol. 122, no. 3, pp. 2008–2025, 2017.

[37] Z. Li, E. J. Fielding, P. Cross, and J.-P. Muller, "Interferometric synthetic aperture radar atmospheric correction: medium resolution imaging spectrometer and advanced synthetic aperture radar integration," *Geophysical Research Letters*, vol. 33, no. 6, 2006.

[38] Z. Li, J.-P. Muller, P. Cross, P. Albert, J. Fischer, and R. Bennartz, "Assessment of the potential of MERIS near-infrared water vapour products to correct ASAR interferometric measurements," *International Journal of Remote Sensing*, vol. 27, no. 2, pp. 349–365, 2006.

[39] C. Delacourt, P. Briole, and J. Achache, "Tropospheric corrections of SAR interferograms with strong topography. Application to Etna," *Geophysical Research Letters*, vol. 25, no. 15, pp. 2849–2852, 1998.

[40] J. Foster, B. Brooks, T. Cherubini, C. Shacat, S. Businger, and C. Werner, "Mitigating atmospheric noise for InSAR using a high resolution weather model," *Geophysical Research Letters*, vol. 33, no. 16, Aug. 2006.

[41] D. Perissin, E. Pichelli, R. Ferretti, F. Rocca, and N. Pierdicca, "The MM5 numerical model to correct PSInSAR atmospheric phase screen," in *Proc. FRINGE Workshop*, Frascati, Italy, 2009.

[42] D. Perissin, F. Rocca, M. Pierdicca, E. Pichelli, D. Cimini, G. Venuti, and B. Rommen, "Mitigation of atmospheric delay in InSAR: The ESA Metawave project," in *Proc. IGARSS*, Vancouver, Canada, 2011, pp. 2558–2561.

[43] R. Jolivet, P. S. Agram, N. Y. Lin, M. Simons, M.-P. Doin, G. Peltzer, and Z. Li, "Improving InSAR geodesy using global atmospheric models," *Journal of Geophysical Research: Solid Earth*, vol. 119, no. 3, pp. 2324–2341, Mar. 2014.

[44] C. Yu, Z. Li, and N. T. Penna, "Interferometric synthetic aperture radar atmospheric correction using a GPS-based iterative tropospheric decomposition model," *Remote Sensing of Environment*, vol. 204, pp. 109–121, 2018.

[45] H. Hersbach and D. Dee, "ERA5 reanalysis is in production," *ECMWF Newsletter*, vol. 147, no. 7, 2016.

[46] R. Jolivet, R. Grandin, C. Lasserre, M.-P. Doin, and G. Peltzer, "Systematic InSAR tropospheric phase delay corrections from global meteorological reanalysis data," *Geophysical Research Letters*, vol. 38, no. 17, Sep. 2011.

[47] X. Cong, U. Balss, M. Eineder, and T. Fritz, "Imaging geodesy—Centimeter-level ranging accuracy with TerraSAR-X: An update," *IEEE Geoscience and Remote Sensing Letters*, vol. 9, no. 5, pp. 948–952, 2012.

[48] X. Cong, "SAR interferometry for volcano monitoring: 3D-PSI analysis and mitigation of atmospheric refractivity," Ph.D. dissertation, Technische Universität München, 2014.

[49] D. Bekaert, R. Walters, T. Wright, A. Hooper, and D. Parker, "Statistical comparison of InSAR tropospheric correction techniques," *Remote Sensing of Environment*, vol. 170, pp. 40–47, 2015.

[50] C. Yu, Z. Li, N. T. Penna, and P. Crippa, "Generic atmospheric correction model for interferometric synthetic aperture radar observations," *Journal of Geophysical Research: Solid Earth*, vol. 123, no. 10, pp. 9202–9222, 2018.

[51] A. Love, "In memory of Carl A. Wiley," *IEEE Antennas and Propagation Society Newsletter*, vol. 27, no. 3, pp. 17–18, 1985.

[52] J. Amos, "Finnish start-up ICEYE's radical space radar solution," *BBC News*, Jan. 2018.

[53] A. Moreira, P. Prats-Iraola, M. Younis, G. Krieger, I. Hajnsek, and K. P. Papathanassiou, "A tutorial on synthetic aperture radar," *IEEE Geoscience and Remote Sensing Magazine*, vol. 1, no. 1, pp. 6–43, 2013.

[54] F. T. Ulaby, F. Kouyate, B. Brisco, and T. L. Williams, "Textural information in SAR images," *IEEE Transactions on Geoscience and Remote Sensing*, no. 2, pp. 235–245, 1986.

[55] R. Bamler and P. Hartl, "Synthetic aperture radar interferometry," *Inverse Problems*, vol. 14, no. 4, p. R1, 1998.

[56] H. A. Zebker and R. M. Goldstein, "Topographic mapping from interferometric synthetic aperture radar observations," *Journal of Geophysical Research: Solid Earth*, vol. 91, no. B5, pp. 4993–4999, 1986.

[57] G. Riegler, S. D. Hennig, and M. Weber, "WORLDDEM – A novel global foundation layer," *International Archives of the Photogrammetry, Remote Sensing and Spatial Information Sciences*, 2015.

[58] F. Amelung, D. L. Galloway, J. W. Bell, H. A. Zebker, and R. J. Laczniak, "Sensing the ups and downs of Las Vegas: InSAR reveals structural control of land subsidence and aquifer-system deformation," *Geology*, vol. 27, no. 6, pp. 483–486, 1999.

[59] E. Chaussard, S. Wdowinski, E. Cabral-Cano, and F. Amelung, "Land subsidence in central Mexico detected by ALOS InSAR time-series," *Remote Sensing of Environment*, vol. 140, pp. 94–106, 2014.

[60] K. P. Papathanassiou and S. R. Cloude, "Single-baseline polarimetric SAR interferometry," *IEEE Transactions on Geoscience and Remote Sensing*, vol. 39, no. 11, pp. 2352–2363, 2001.

[61] A. Reigber and A. Moreira, "First demonstration of airborne SAR tomography using multibaseline L-band data," *IEEE Transactions on Geoscience and Remote Sensing*, vol. 38, no. 5, pp. 2142–2152, 2000.

[62] S. Cloude, *Polarisation: Applications in remote sensing*. Oxford University Press, 2010.

[63] S. R. Cloude and K. P. Papathanassiou, "Polarimetric SAR interferometry," *IEEE Transactions on geoscience and remote sensing*, vol. 36, no. 5, pp. 1551–1565, 1998.

[64] I. Hajnsek and S. Cloude, "Differential extinction estimation over agricultural vegetation from PolInSAR," in *ESA Special Publication*, vol. 586, 2005, p. 29.

[65] J. Dall, "InSAR elevation bias caused by penetration into uniform volumes," *IEEE Transactions on Geoscience and Remote Sensing*, vol. 45, no. 7, pp. 2319–2324, 2007.

[66] J. M. Lopez-Sanchez, I. Hajnsek, and J. D. Ballester-Berman, "First demonstration of agriculture height retrieval with PolInSAR airborne data," *IEEE Geoscience and Remote Sensing Letters*, vol. 9, no. 2, pp. 242–246, 2012.

[67] J. J. Sharma, I. Hajnsek, and K. P. Papathanassiou, "Long-wavelength Pol-InSAR for glacier ice extinction estimation," in *Proc. EUSAR*. Aachen, Germany: VDE, 2010, pp. 1–4.

[68] J. J. Sharma, I. Hajnsek, K. P. Papathanassiou, and A. Moreira, "Estimation of glacier ice extinction using long-wavelength airborne Pol-InSAR," *IEEE Transactions on Geoscience and Remote Sensing*, vol. 51, no. 6-2, pp. 3715–3732, 2013.

[69] R. Ahmed, P. Siqueira, S. Hensley, B. Chapman, and K. Bergen, "A survey of temporal decorrelation from spaceborne L-band repeat-pass InSAR," *Remote Sensing of Environment*, vol. 115, no. 11, pp. 2887–2896, 2011.

[70] S. Lee, F. Kugler, I. Hajnsek, and K. P. Papathanassiou, "The impact of temporal decorrelation over forest terrain in polarimetric SAR interferometry," in *Proc. Workshop POLinSAR*, ESRIN, Italy, 2009.

[71] N. Yagüe-Martínez, P. Prats-Iraola, F. R. Gonzalez, R. Brcic, R. Shau, D. Geudtner, M. Eineder, and R. Bamler, "Interferometric processing of Sentinel-1 TOPS data," *IEEE Transactions on Geoscience and Remote Sensing*, vol. 54, no. 4, pp. 2220–2234, 2016.

[72] P. Prats-Iraola, R. Scheiber, L. Marotti, S. Wollstadt, and A. Reigber, "TOPS interferometry with TerraSAR-X," *IEEE Transactions on Geoscience and Remote Sensing*, vol. 50, no. 8, pp. 3179–3188, 2012.

[73] C. Werner, U. Wegmuller, A. Wiesmann, and T. Strozzi, "Interferometric point target analysis with JERS-1 L-band SAR data," in *Proc. IGARSS*, vol. 7. Toulouse, France: IEEE, 2003, pp. 4359–4361.

[74] A. Hooper, H. Zebker, P. Segall, and B. Kampes, "A new method for measuring deformation on volcanoes and other natural terrains using InSAR persistent scatterers," *Geophysical Research Letters*, vol. 31, no. 23, 2004.

[75] S. Usai, "A least squares database approach for SAR interferometric data," *IEEE Transactions on Geoscience and Remote Sensing*, vol. 41, no. 4, pp. 753–760, 2003.

[76] O. Mora, J. J. Mallorquí, and A. Broquetas, "Linear and nonlinear terrain deformation maps from a reduced set of interferometric SAR images," *IEEE Transactions on Geoscience and Remote Sensing*, vol. 41, no. 10, pp. 2243–2253, 2003.

[77] H. Vadon and F. Sigmundsson, "Crustal deformation from 1992 to 1995 at the Mid-Atlantic Ridge, southwest Iceland, mapped by satellite radar interferometry," *Science*, vol. 275, no. 5297, pp. 194–197, 1997.

[78] R. Lanari, P. Lundgren, and E. Sansosti, "Dynamic deformation of Etna volcano observed by satellite radar interferometry," *Geophysical Research Letters*, vol. 25, no. 10, pp. 1541–1544, 1998.

[79] M. Tesauro, P. Berardino, R. Lanari, E. Sansosti, G. Fornaro, and G. Franceschetti, "Urban subsidence inside the city of Napoli (Italy) observed by satellite radar interferometry," *Geophysical Research Letters*, vol. 27, no. 13, pp. 1961–1964, 2000.

[80] A. Ferretti, C. Prati, and F. Rocca, "Nonlinear subsidence rate estimation using permanent scatterers in differential SAR interferometry," *IEEE Transactions on Geoscience and Remote Sensing*, vol. 38, no. 5, pp. 2202–2212, 2000.

[81] M. Costantini, F. Malvarosa, F. Minati, and L. Pietranera, "Optimal combination of multiple SAR differential interferometric measurements for monitoring terrain displacements," in *Proc. IEEE/ISPRS Joint Workshop on Remote Sensing and Data Fusion over Urban Areas.* Rome, Italy: IEEE, 2001, pp. 53–57.

[82] O. Mora, J. J. Mallorquí, and J. Duro, "Generation of deformation maps at low resolution using differential interferometric SAR data," in *Proc. IGARSS*, vol. 5. Toronto, Canada: IEEE, 2002, pp. 2696–2698.

[83] A. Ferretti, G. Savio, R. Barzaghi, A. Borghi, S. Musazzi, F. Novali, C. Prati, and F. Rocca, "Submillimeter accuracy of InSAR time series: Experimental validation," *IEEE Transactions on Geoscience and Remote Sensing*, vol. 45, no. 5, pp. 1142–1153, 2007.

[84] T. H. Dixon, F. Amelung, A. Ferretti, F. Novali, F. Rocca, R. Dokka, G. Sella, S.-W. Kim, S. Wdowinski, and D. Whitman, "Space geodesy: Subsidence and flooding in New Orleans," *Nature*, vol. 441, no. 7093, pp. 587–588, 2006.

[85] D. A. Schmidt and R. Bürgmann, "Time-dependent land uplift and subsidence in the Santa Clara valley, California, from a large interferometric synthetic aperture radar data set," *Journal of Geophysical Research: Solid Earth*, vol. 108, no. B9, 2003.

[86] P. Lundgren, S. Usai, E. Sansosti, R. Lanari, M. Tesauro, G. Fornaro, and P. Berardino, "Modeling surface deformation observed with synthetic aperture radar interferometry at Campi Flegrei caldera," *Journal of Geophysical Research: Solid Earth*, vol. 106, no. B9, pp. 19 355–19 366, 2001.

[87] O. Mora, J. J. Mallorquí, J. Duro, and A. Broquetas, "Long-term subsidence monitoring of urban areas using differential interferometric SAR techniques," in *Proc. IGARSS*, vol. 3. Sydney, Australia: IEEE, 2001, pp. 1104–1106.

[88] O. Mora, R. Lanari, J. J. Mallorquí, P. Berardino, and E. Sansosti, "A new algorithm for monitoring localized deformation phenomena based on small baseline differential SAR interferograms," in *Proc. IGARSS*, vol. 2. Toronto, Canada: IEEE, 2002, pp. 1237–1239.

[89] J. J. Mallorquí, O. Mora, P. Blanco, and A. Broquetas, "Linear and non-linear long-term terrain deformation with DInSAR (CPT: Coherent Pixels Technique)," in *Proc. FRINGE Workshop*, Frascati, Italy, 2003, pp. 1–8.

[90] G. Centolanza, "Quality evaluation of DInSAR results from the phase statistical analysis," Ph.D. dissertation, Universitat Politècnica de Catalunya, 2015.

[91] R. Iglesias, "High-resolution space-borne and ground-based SAR persistent scatterer interferometry for landslide monitoring," Ph.D. dissertation, Universitat Politècnica de Catalunya, 2015.

[92] D. Monells Miralles, "Orbital differential SAR interferometry with polarimetric data," Ph.D. dissertation, Universitat Politècnica de Catalunya, 2017.

[93] P. Blanco Sánchez, "SAR differential interferometry for deformation monitoring under a multi-frequency approach," Ph.D. dissertation, Universitat Politècnica de Catalunya, 2009.

[94] R. Iglesias, J. J. Mallorquí, and P. López-Dekker, "DInSAR pixel selection based on sublook spectral correlation along time," *IEEE Transactions on Geoscience and Remote Sensing*, vol. 52, no. 7, pp. 3788–3799, 2014.

[95] N. Cressie, "Statistics for spatial data: Wiley series in probability and statistics," *Wiley-Interscience New York*, vol. 15, p. 16, 1993.

[96] C. Dietrich and G. Newsam, "A fast and exact method for multidimensional Gaussian stochastic simulations," *Water Resources Research*, vol. 29, no. 8, pp. 2861–2869, 1993.

[97] B. M. Welsh, "Fourier-series-based atmospheric phase screen generator for simulating anisoplanatic geometries and temporal evolution," in *Proc. Propagation and Imaging through the Atmosphere*. San Diego, USA: International Society for Optics and Photonics, 1997, pp. 327–338.

[98] J. Gottsmann, L. Wooller, J. Martí, J. Fernández, A. G. Camacho, P. Gonzalez, A. Garcia, and H. Rymer, "New evidence for the reawakening of Teide volcano," *Geophysical Research Letters*, vol. 33, no. 20, 2006.

[99] J. Almendros, J. M. Ibáñez, E. Carmona, and D. Zandomeneghi, "Array analyses of volcanic earthquakes and tremor recorded at Las Cañadas caldera (Tenerife island, Spain) during the 2004 seismic activation of Teide volcano," *Journal of Volcanology and Geothermal Research*, vol. 160, no. 3, pp. 285–299, 2007.

[100] J. Gottsmann, A. G. Camacho, J. Martí, L. Wooller, J. Fernández, A. Garcia, and H. Rymer, "Shallow structure beneath the central volcanic complex of Tenerife from new gravity data: implications for its evolution and recent reactivation," *Physics of the Earth and Planetary Interiors*, vol. 168, no. 3-4, pp. 212–230, 2008.

[101] C. W. Chen and H. A. Zebker, "Two-dimensional phase unwrapping with use of statistical models for cost functions in nonlinear optimization," *Journal of the Optical Society of America A*, vol. 18, no. 2, pp. 338–351, 2001.

[102] E. K. Smith and S. Weintraub, "The constants in the equation for atmospheric refractive index at radio frequencies," *Proc. IRE*, vol. 41, no. 8, pp. 1035–1037, 1953.

[103] N. Adam, "Algorithmic PSI improvement in mountainous areas by atmosphere mitigation," *Terrafirma (ESA) Technical Note*, 2014.

[104] Z. Hu and J. J. Mallorquí, "A direct method to estimate atmospheric phase delay for InSAR with global atmospheric models," in *Proc. IGARSS*, Valencia, Spain, 2018, pp. 2196–2199.

[105] SUHET, *Sentinel-1 user handbook*. European Space Agency, 2013, from ESA website: https://sentinel.esa.int/.

[106] M. Solana, "Evaluación de la peligrosidad volcánica en Tenerife a partir de la reconstrucción de cuatro erupciones históricas," Ph.D. dissertation, Universidad Complutense de Madrid, 1998.

[107] J. Fernández, T.-T. Yu, G. Rodrıguez-Velasco, J. González-Matesanz, R. Romero, G. Rodrıguez, R. Quirós, A. Dalda, A. Aparicio, and M. Blanco, "New geodetic monitoring system in the volcanic island of Tenerife, Canaries, Spain. Combination of InSAR and GPS techniques," *Journal of Volcanology and Geothermal Research*, vol. 124, no. 3-4, pp. 241–253, 2003.

[108] J. Fernández, R. Romero, D. Carrasco, K. F. Tiampo, G. Rodríguez-Velasco, A. Aparicio, V. Araña, and F. González-Matesanz, "Detection of displacements on Tenerife island, Canaries, using radar interferometry," *Geophysical Journal International*, vol. 160, no. 1, pp. 33–45, 2005.

[109] J. Fernández, P. Tizzani, M. Manzo, A. Borgia, P. González, J. Martí, A. Pepe, A. Camacho, F. Casu, P. Berardino *et al.*, "Gravity-driven deformation of Tenerife measured by InSAR time series analysis," *Geophysical Research Letters*, vol. 36, no. 4, 2009.

[110] A. Eff-Darwich, J. C. Pérez, J. Fernández, B. García-Lorenzo, A. González, and P. J. González, "Using a mesoscale meteorological model to reduce the effect of tropospheric water vapour from DInSAR data: A case study for the island of Tenerife, Canary Islands," *Pure and Applied Geophysics*, vol. 169, no. 8, pp. 1425–1441, 2012.

[111] W. C. Skamarock, J. B. Klemp, J. Dudhia, D. O. Gill, D. M. Barker, W. Wang, and J. G. Powers, "A description of the advanced research WRF version 3. NCAR Technical note-475+ STR," *Mesoscale and Microscale Meteorology Division*, 2008.

[112] S. Rieger, "Regional-scale, natural persistent scatterer interferometry, island of Crete (Greece), and comparison to vertical surface deformation on the millennial-, and million-year time-scales," Ph.D. dissertation, Ludwig Maximilian University of Munich, 2015.

[113] A. Pulido-Bosch, J. Delgado, F. Sola, Á. Vallejos, F. Vicente, J. M. López-Sánchez, and J. J. Mallorquí, "Identification of potential subsidence related to pumping in the Almería basin (SE Spain)," *Hydrological Processes*, vol. 26, no. 5, pp. 731–740, 2012.

[114] C. W. Chen and H. A. Zebker, "Phase unwrapping for large SAR interferograms: Statistical segmentation and generalized network models," *IEEE Transactions on Geoscience and Remote Sensing*, vol. 40, no. 8, pp. 1709–1719, 2002.

[115] D. Dee, S. Uppala, A. Simmons, P. Berrisford, P. Poli, S. Kobayashi, U. Andrae, M. Balmaseda, G. Balsamo, P. Bauer *et al.*, "The ERA-Interim reanalysis: Configuration and performance of the data assimilation system," *Quarterly Journal of the Royal Meteorological Society*, vol. 137, no. 656, pp. 553–597, 2011.

[116] M. M. Rienecker, M. J. Suarez, R. Gelaro, R. Todling, J. Bacmeister, E. Liu, M. G. Bosilovich, S. D. Schubert, L. Takacs, G.-K. Kim *et al.*, "MERRA: NASA's modern-era retrospective analysis for research and applications," *Journal of Climate*, vol. 24, no. 14, pp. 3624–3648, 2011.

[117] B. Puysségur, R. Michel, and J.-P. Avouac, "Tropospheric phase delay in interferometric synthetic aperture radar estimated from meteorological model and multispectral imagery," *Journal of Geophysical Research: Solid Earth*, vol. 112, no. B5, 2007.

[118] G. Nico, R. Tome, J. Catalao, and P. M. Miranda, "On the use of the WRF model to mitigate tropospheric phase delay effects in SAR interferograms," *IEEE Transactions on Geoscience and Remote Sensing*, vol. 49, no. 12, pp. 4970–4976, 2011.

[119] J. Jung, D.-j. Kim, and S.-E. Park, "Correction of atmospheric phase screen in time series InSAR using WRF model for monitoring volcanic activities," *IEEE Transactions on Geoscience and Remote Sensing*, vol. 52, no. 5, pp. 2678–2689, 2014.

[120] J. Foster, J. Kealy, T. Cherubini, S. Businger, Z. Lu, and M. Murphy, "The utility of atmospheric analyses for the mitigation of artifacts in InSAR," *Journal of Geophysical Research: Solid Earth*, vol. 118, no. 2, pp. 748–758, Feb. 2013.

[121] L. F. Richardson, *Weather prediction by numerical process.* Cambridge University Press, 2007.

[122] L. M. Harris and D. R. Durran, "An idealized comparison of one-way and two-way grid nesting," *Monthly Weather Review*, vol. 138, no. 6, pp. 2174–2187, 2010.

List of Publications

Journal Articles

J1 **Z. Hu**, J. J. Mallorquí, "An Accurate Method to Correct Atmospheric Phase Delay for InSAR with the ERA5 Global Atmospheric Model," *Remote Sensing*, vol. 11, no. 17, pp. 1969: 1-22, August 2019.

J2 **Z. Hu**, J. J. Mallorquí and H. Fan, "Atmospheric Artifacts Correction with a Covariance-Weighted Linear Model over Mountainous Regions," *IEEE Transactions on Geoscience and Remote Sensing*, vol. 56, no. 12, pp. 6995-7008, December 2018.

Conference Papers

C1 **Z. Hu**, J. J. Mallorquí, "A Direct Method to Estimate Atmospheric Phase Delay for Insar with Global Atmospheric Models," *IGARSS 2018, Valencia, Spain*, pp. 2196-2199. Received the *Symposium Interactive Prize Paper Award of IGARSS 2018*.

C2 **Z. Hu**, J. J. Mallorquí, "Comparison of InSAR Atmospheric Phase Screen Correction with Global Atmospheric Models (GAM)," *EUSAR 2018, Aachen, Germany*, pp. 1-4.

C3 **Z. Hu**, J. J. Mallorquí, G. Centolanza and J. Duro, "InSAR Atmospheric Delays Compensation: Case Study in Tenerife Island," *IGARSS 2017, Fort Worth, TX, USA*, pp. 3167-3170.

C4 J. J. Mallorquí, **Z. Hu**, J. Corominas and J. A. Gili, "Landslide Monitoring with Staring-spotlight Data: Canillo Case Study," *IGARSS 2017, Fort Worth, TX, USA*, pp. 3174-3177.